



TECHNISCHE
UNIVERSITÄT
WIEN

VIENNA
UNIVERSITY OF
TECHNOLOGY

Diese Dissertation haben begutachtet:

.....

DISSERTATION

Thresholds for Laser-Induced Thermal Injury of Ex-vivo Bovine Retina Explant

Ausgeführt zum Zwecke der Erlangung des akademischen Grades eines Doktors der
Technischen Wissenschaften unter der Leitung von

(Betreuung) Ao.Univ.Prof. Dipl.-Ing. Dr.techn. Wolfgang Husinsky
E134 – Institute of Applied Physics
Wiedner Hauptstrasse 8, A-1040, Wien, Austria

Eingereicht an der Technischen Universität Wien
Fakultät für Physik

von

(VerfasserInn) Rahat Ullah
0827843
Kölblgasse 35/1, 1030, Wien

Wien, 11 November 2010

eigenhändige Unterschrift

Kurzfassung

Die besonderen Eigenschaften wie geringe Divergenz und die Fähigkeit extrem hohe Leistungsdichte zu erreichen, machen Laserstrahlung attraktiv für viele Anwendungen, sind aber zugleich der Grund dafür, dass schwere Augen- und Hautschäden auftreten können. Der menschliche Körper, vor allem Organe wie das Auge, ist besonders anfällig für Verletzungen von kommerziell verfügbaren oder experimentellen Lasern. Forschung über das Schädigungspotential des menschlichen Auges und der Haut ist seit der Erfindung des Lasers laufend, um die Gefahren von Laserstrahlung zu verstehen.

Die Mehrheit der Daten werden experimentell von Laser-Induzierte Schädigung der Netzhaut an nicht-menschlichen Primaten (Rhesusaffen) und anderen Tieren gewonnen, jedoch einige an Freiwillige Daten oder Unfälle (meist aus den ersten Jahren des Laser-Operationen) sind ebenfalls erhältlich. Basiert auf diesen Ergebnissen sind Grenzwerte, als Maximum Zulässige Bestrahlung (MZB) bekannt, von der Internationalen Kommission zum Schutz vor nichtionisierender Strahlung (ICNIRP) festgelegt und für Normen von der Internationalen Elektrotechnischen Kommission (IEC 60825-1) sowie als American National Standards Institute (ANSI Z-136,1) übernommen. Diese Schädigungsschwellenwerte ziehen eine Grenze zwischen gefährliche und eher sichere Bestrahlungen.

In dieser Studie sind ex-vivo Rinderaugen als experimentelles Modell für die Bestimmung der laserinduzierten thermischen Schädigungen der Netzhaut unter verschiedenen definierten Prüfbedingungen verwendet. Insgesamt sind 9360 Bestrahlungen auf 388 Augenproben durchgeführt worden. Schädigungsschwellen, durch Fluoreszenz-Mikroskopie bewertet, zeigen gute Übereinstimmung mit Ergebnissen eines von Mathieu Jean in der Seibersdorf Labor GmbH entwickelt erweiterten Computer-Modells. Beide Modelle untermauern gut die bereits publizierten Daten von In-vivo-Rhesusaffen. Die Abhängigkeit der Schwellenwerte auf Pulsdauern in den Millisekunden- und Sekundenbereiche und auf verschiedenen Spotgröße wurde für die Wellenlänge von 1090 nm zum ersten Mal ermittelt.

Der Zweck dieser Studie war: (1) thermische Schädigungsschwellenwerte der Netzhaut in ex-vivo Rinderaugen als Modell zu untersuchen, (2) das Computer-Modell mit dem Arrhenius Kriterium zu validieren, und (3) diese beiden Modelle mit in-vivo Rhesusaffen Daten in Verbindung zu setzen. Letztlich, nach der Validierung dieses Computer-Modells wird es Grundlage für Sicherheitsanalyse komplizierter Szenarien anbieten.

Dedication

I dedicate this research work to my wife for her full support and cooperation throughout my PhD studies and to my mother for her endless efforts throughout my academic career.

Acknowledgment

My first and most earnest acknowledgment must go to my co-supervisor Dr. Karl Schulmeister. I can not forget his very kind response when i was looking for my PhD supervisor. His cooperation and support, both financial and moral, gave me the courage to complete my higher studies at the Technical University Vienna (TU Wien). Having difficulty in appropriate words selection for him I can only say that he has been instrumental in ensuring my academic, professional, personal and moral well being ever since. In every sense, none of this work would have been possible without his relentless and continuous help.

I would also like to thank my academic supervisor Prof. Wolfgang Husinsky at Technical University Vienna for his relentless and continuous help and for providing me the opportunity to register at the Technical University Vienna under his supervision. In Seibersdorf Laboratories GmbH, (Previously known ARC), i started my experimental work in the group of Laser and Optical Radiation Safety. I cannot forget the valuable scientific discussions with my group mates, particularly with Weber Marko and Reinhard Gilber throughout my research work during my PhD studies. They all have my sincere gratitude. I am also deeply grateful to our secretary Kaman Martina who remained very helpful and kind throughout my stay here in Seibersdorf.

I am also very deeply grateful of my brothers and relatives back in my country that remained in continuous touch with my professional as well as my personal activities. In Particular, I would like to thank my brother Mr Rahmat Khan, for his support and endless care of my family in Pakistan during my first year studies. He always remain helpful and spar his precious time for my personal works and activities. I always received an unexpected and generous support from him whenever he was called.

Last, but far from least, I want to express my deep appreciations for my wife who has suffered more for this dissertation than anyone. Particularly, when she was in Pakistan, far away from me, and takes care of my lovely son Raza Ullah Khalil and my chubby daughter Maleeha Khalil. After joining me here in Vienna two years back, she saved my lot of time by providing me well prepared food and help when ever I needed. She took well care of me and my children. Her full support made my life easy in the duration of my PhD research.

Table of Content

ABSTRACT.....	1
1 ANATOMY OF THE EYE	4
1.1 STRUCTURE OF THE EYE	4
1.2 RETINA OF THE EYE	6
1.3 THE RETINAL PIGMENT EPITHELIUM (RPE)	8
1.4 COMPOSITION AND FUNCTION OF MELANIN/MELANOSOMES	10
2 BASICS OF LASER-TISSUE INTERACTION.....	13
2.1 PHYSICAL PRINCIPLES GOVERNING LIGHT TISSUE INTERACTION	13
2.1.1 Absorption of Laser Radiation.....	13
2.1.2 Optical Properties of the Tissue.....	14
2.1.3 Concept of Energy Confinement	16
2.1.4 Light Propagation in the Eye	18
2.2 PHOTOCHEMICAL INTERACTION.....	21
2.2.1 Photo-Oxidative Effects.....	21
2.2.2 Photosensitized Reactions.....	22
2.3 THERMAL INTERACTION	24
2.3.1 Rise in Tissue Temperature	24
2.3.2 The Protein Denaturation.....	26
2.3.3 Thermal Confinement Time.....	27
2.3.4 Damage Criterion to the Eye	28
2.4 PHOTOABLATION	29
2.5 PLASMA-INDUCED ABLATION	31
2.6 PHOTODISRUPTION.....	33
3 EXPOSURE LIMITS	37
3.1 THE CONCEPT OF THRESHOLD AND SAFETY FACTOR	37
3.2 DOSE-RESPONSE CURVE.....	39
3.3 LOG-NORMAL DISTRIBUTION	41
3.4 PROBIT ANALYSIS.....	44
3.5 FIDUCIAL LIMITS	46
3.6 CORNEAL AND RETINAL SPACE	48
3.7 DEPENDENCE ON ANGULAR SUBTENSE.....	49
3.8 COMPUTER MODEL USED FOR RETINAL THERMAL DAMAGE THRESHOLDS.....	51

3.8.1	Overview.....	51
3.8.2	Optical Model	51
3.8.3	Thermal Model	53
3.8.4	Damage Model.....	54
4	DAMAGE THRESHOLD FOR THE WAVELENGTH OF 1090 NM.....	57
4.1	BACKGROUND.....	57
4.2	EXPERIMENTAL SETUP.....	57
4.3	SAMPLE PREPARATION AND EXPOSURE	60
4.3.1	Chondroitinase ABC Assay	60
4.3.2	Live/Dead Assay	61
4.3.3	Exposure	63
4.4	DATA ANALYSIS	64
4.5	UNCERTAINTY AND VARIABILITY FACTORS	66
4.6	RESULTS	68
4.6.1	<i>Ex-vivo</i> Bovine and Computer Model	68
4.6.2	Comparison with Non-Human Primate (NHP) Threshold Data.....	71
4.6.3	Comparison with the 532 nm <i>Ex-vivo</i> Bovine Threshold Data.....	74
4.7	DISCUSSION	76
4.7.1	Spot Size and Time Dependencies.....	76
4.7.2	Comparison with Nonhuman Primate (NHP) Threshold Data.....	78
4.7.3	Comparison with the 532 nm <i>Ex-vivo</i> Bovine Threshold Data	79
5	EFFECT OF THE HANK SOLUTION, TEMPERATURE, AND DYE ON DAMAGE THRESHOLD.....	81
5.1	BACKGROUND.....	81
5.2	EXPERIMENTAL SETUP.....	82
5.3	RESULTS AND DISCUSSION	85
5.3.1	Effect of Hank Solution on Threshold Data	85
5.3.2	Effect of Temperature on Threshold Data	90
5.3.3	Effect of Dye CalceinAM on Threshold Data	92
6	SUMMARY	98
	EXPERIMENTAL RESULTS.....	102
	BIBLIOGRAPHY	108

Abstract

The special properties such as low divergence and ability to reach extremely high power density make laser radiation attractive for many applications, but are at the same time the very reason for laser radiation to be able to cause severe eye and skin injuries. The human body, particularly the organ eye, is most vulnerable to injury by most lasers now available. Research related to the injury threshold of the eye and skin has been ongoing since the invention of laser, in order to understand the biological hazards of laser radiation.

The majority of the threshold data, based on laser induced retinal injury, are obtained from experiments on non-human primate (rhesus monkey) and other animals, however, some experimental data on human volunteers or laser based accidents (mostly from the first years of laser operations) are also available. Based on these threshold results, exposure limits known as *maximum permissible exposure* or shortly MPE's are set by the *International Commission on Non-Ionizing Radiation Protection* (ICNIRP) and adopted by safety standardization committees of the *International Electrotechnical Commission* (IEC 60825-1) as well as *American National Standards Institute* (ANSI Z-136.1). These limits draw a boundary between those known as hazardous for the eye or the skin and those considered safe.

In this study, *ex-vivo* explant bovine eyes are used as experimental model for determining laser induced retinal thermal damage threshold for varying spot sizes and exposure durations. For several combinations, in total 9360 exposures have been executed on 388 bovine retinal samples. Damage thresholds, based on fluorescence microscopy, compare well with the prediction/results of an extended computer model developed by Mathieu Jean at Seibersdorf Labor GmbH. Both models threshold data compare well with the already published data of *in-vivo* rhesus monkey available in this time and wavelength domain. The dependence of thermal damage thresholds on pulse durations for time between 1 ms - 1 s for the wavelength of 1090 nm was determined for the first time for a range of retinal spot sizes.

The purpose of this study was (1) to investigate damage thresholds for retinal thermal injury using *ex-vivo* bovine eye as model, (2) to validate the computer model, stated above, used for retinal thermal threshold calculations based on Arrhenius damage criterion, and (3) to correlate these two model data with *in-vivo* rhesus monkey threshold data available in this time and wavelength domain. Ultimately, after

validation, this computer model will provide the basis for safety analysis of more complicated retinal exposures scenarios and will be used in the future for calculating damage thresholds of more complex laser beam parameters.

I. BACKGROUND

1 Anatomy of the Eye

1.1 Structure of the Eye

As a conscious sense organ, the eye allows vision. Rod and cone cells in the retina allow conscious light perception and vision including colour differentiation and the perception of depth. Seven cranial and facial bones form the orbit cavity. An adult human eye ball is approximately 24-25 mm in diameter, and contained within this orbit. Additionally, nerve tissue, fat, blood vessels, and muscle are also contained in the orbit. Six muscles control all movement of the eye within the bony socket. Figure 1.1 is a schematic overview of the human eye.

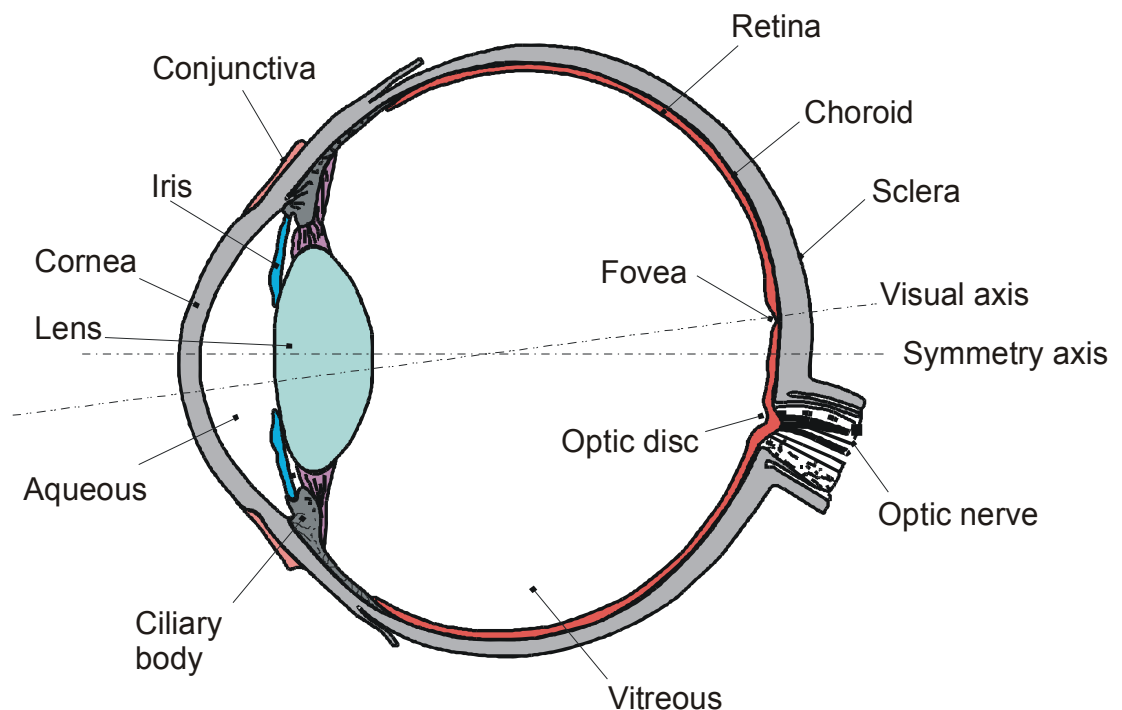


Figure 1.1: Anatomy of the human eye [3]

The cornea is the transparent front part of the eye that covers the iris, pupil, and the anterior chamber. Together with lens, the cornea focus the light on to the retina, and accounting for two third of the optical power of the eye. In human, the optical power of the cornea is approximately 43 dioptres [1]. The cornea which contributes most of the refractive power of the eye is fixed. It is the curvature of the lens that can be adjusted to tune the focus depending upon the object distance. The pupil is an opening located in the center of the iris behind the cornea and aqueous humor of the eye that allows the light to reach the retina. The iris consists of two muscle layers which can expand or contract varying the size of the pupil. In human, the pupil size can be adjusted between

2 to 7 mm. The iris is in contact with the anterior portion of the lens, and is attached to the ciliary muscles that control the focusing power of the lens by changing its shape and curvature. The lens becomes less pliable with age, affecting the optical power of the eye, and focusing becomes difficult or even impossible. The anterior chamber of the eye consists by the space between iris/lens and cornea. Posterior to the iris, the ciliary muscles and lens form the posterior chamber. Both chambers are filled with aqueous humor, which are transparent to visible and near infrared light and, continuously flowed through the chamber. Posterior to the lens and ciliary muscles, the vitreous body, a gel like material, fills and aids in shaping the eyeball. The vitreous body is transparent to visible and near infrared light too and is attached to the retina.

The choroid is the vascular layer containing connective tissue of the eye lying between the retina and the sclera. The human choroid is heavily pigmented with melanosomes. In humans its thickness is varying between $\sim 250 - 450 \mu\text{m}$ [2]. The choroid provides oxygen and nourishment to the outer layers of the retina. The blood vessels in the choroid and even in the choriocapillaris are large in diameter about 10 to 30 μm compared to the normal capillaries size i.e. 8 μm or less [24]. Generally, only a single blood corpuscle can move at a time in the capillary in other part of the body, whereas in the choriocapillaries of the choroid several corpuscles can move through at the same time. The presence of blood in the choroid suggests that the oxygen supply to the tissue may be only a secondary function of the circulation in the choroid. Perhaps, the primary function of the blood circulation in the choroid is to keep the eye warm and at uniform temperature. This extreme vascularity also indicates that heat from laser exposures introduced in this region under study state conditions do very little in rising temperature unless high power levels are used. Between the choroid and the pigment epithelium is Bruch's membrane separating the retina from the cellular components of the blood. It is possible that breaks in Bruch's membrane from exposures to laser and other optical sources results in originally slight trauma into serious retinal injury.

The sclera, also known as the white part of the human eye, forms the outer most portion of the eye. It consists of dense fibrous tissue and is roughly spherical in shape. In the front of the eye it blends into the cornea, and on can considered cornea as a transparent part of the sclera. The sclera is about 1 mm thick near the optic nerve region and is approximately 0.5 mm thick in the middle or at the equator and again become 1 mm thick in front where it blends into the cornea [24]. The shape of the eye ball is maintained by the sclera up to some extent, but mostly maintained by the internal

pressure of the humar. The retina, posterior to the vitreous, consists primarily of photoreceptor (rods and cones) and nerve cells, is discussed in detail in the following section 1.2.

1.2 Retina of the Eye

The retina is a light sensitive tissue lining the inner surface of the eye. The optics of the eye creates an image of the visual world on the retina. Light striking the retina initiates a cascade of chemical and electrical events that ultimately trigger nerve impulses. These impulses are sent to various visual centers of the brain through the fibers of the optic nerve. The retina consists of three types of neurons (nerve cells): ganglion cells, bipolar cells and photoreceptor cells. A schematic overview of these neuron cells is shown in figure 1.2. . The two layers of nerve cells (bipolar and ganglion) lies on top of the photoreceptor cells and are transparent, such that light entering through the pupil actually passes through these two cell layers before reaching the photoreceptor cells. The photoreceptor cells convert the absorbed light energy into nerve impulses. These impulses are received by the nerve cells which transmit them to the brain through the optic nerve that exits in the back of the eye.

A retinal ganglion cell is a type of neuron located near the inner surface of the retina of the eye. There are about 1.3 million ganglion cells in the human visual system that receives visual information from photoreceptors via two intermediate neuron types: bipolar cells and amacrine cells. Retinal ganglion cells collectively transmit visual information from the retina to several regions in the brain. The axons of the ganglion cells combine in the center of optic disc until they emerge in the visual cortex of the brain. Recently discovered photosensitive ganglion cells are excited by light even in the absence of rods and cones. These novel cells contains thier own photopigment, melanopsin, whose functional role is non-image-forming, totally different from that of rods and cones. The photopigment of these photoreceptive ganglion cells, melanopsin, is excited by light mainly in the blue portion of the visible spectrum ~ 480 nm [4]. One of the primary functions is their contribution in synchronizing circadian rhythms i.e. the body's 24-hour biological clock. Moreover, they also play an important role in the regulation of pupil size and other behavioural responses to ambient lighting conditions. [6].

The bipolar cells which exist between photoreceptors (rod cells and cone cells) and ganglion cells act directly or indirectly transmitting signals from photoreceptor cells to

the ganglion cells. Bipolar cells have a central body from which two sets of processes arise. They can synapse with either rods or cones (photoreceptors) but not both and they also accept synapses from horizontal cells. The bipolar cells then transmit the signals from the photoreceptors or the horizontal cells, and pass it on to the ganglion cells through localized graded potentials. Bipolar cells are categorized into two different groups, ON and OFF, on the basis of how they react to photoreceptor cells glutamate (Proteinogenic amino acid). In dark conditions, photoreceptor cells releases glutamate, which excites or activates the OFF bipolar cells inhibiting the ON bipolar cells. However, as light strikes the photoreceptor cells causes it to be inhibited, and thus no glutamate to be given off. In this scenario, the ON bipolar becomes active, while the OFF bipolar cell loses its excitation and becomes silent [7].

The photoreceptor cell is a specialized type of neuron (nerve cell) founds in the eye's retina which is responsible for visual phototransduction. Two types of photoreceptor cells: rods and cones constitute the sensory retina, contributing information to form a representation of the visual world. There are, however, major functional differences between the rods and cones. In the human retina there are probably 120 millions rods averaging 60 μm long and 2 μm in diameter. Rods are mostly concentrated on the outer edge of the retina. Rods are very sensitive to movement, but do not detect color well, being responsible for twilight vision. Additionally, the human retina contained approximately 6 million cones, averaging 50 μm long and 3-5 μm in diameter [24]. They are adapted to colors, and function well in the day light. In human three different types of cones responds to short (blue), medium (green) and long (yellow-red) light respectively. Thus, humans have trichromatic vision with different photopsins, which have different response curves and thus respond to variation in color in different ways. The outer segments of rods and cones are immediately anterior to the retinal pigment epithelium (RPE).

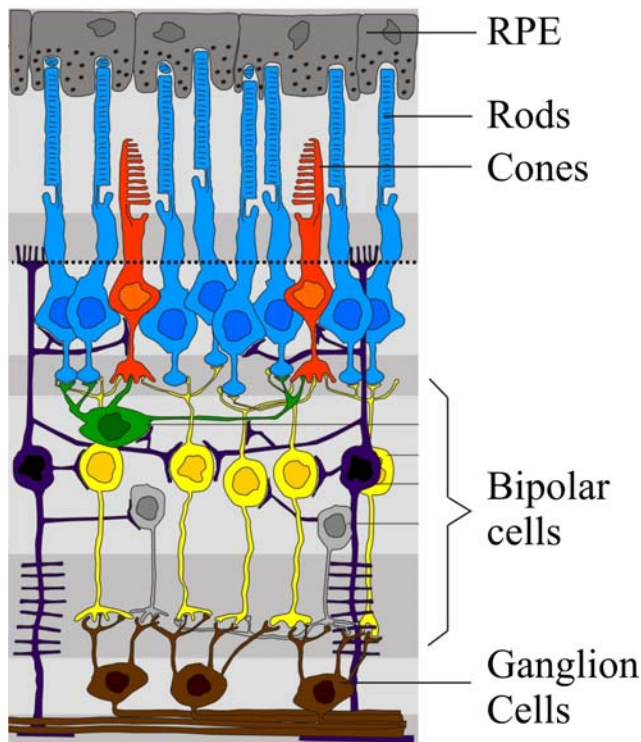


Figure 1.2: Schematic structure of the neurons of the retina and RPE. Light incident from the bottom.

1.3 The Retinal Pigment Epithelium (RPE)

Initially only regarded as the dark cover of the inner wall of the bulbus, today's understanding of the multiple functions of RPE, supporting the normal photoreceptor function, make it essential for visual function. Although, the embryonic origin of the RPE and photoreceptor is different, however, the development and differentiation of both these tissues reflects the view that RPE together with photoreceptors is one functional unit. Studies have shown that disease resulting from defects in genes in normally express photoreceptors leads to degeneration of the RPE, such as ATP-Binding Cassette Transporter (*ABCR* or *ABCA4*), where it believed to transport retinol (vitamin A)/phospholipid derivatives from the photoreceptor outer segment disks into the cytoplasm. Similarly, studies have also confirmed that, defects in genes in the RPE results in the degeneration of photoreceptors, for example, *MerTK* or *RPE65* [5].

The retinal pigment epithelium (RPE) is a monolayer of hexagonal cells about 10-15 μm thick. The human RPE cell is about 14 μm in diameter and 12 μm height in the macula, while reaches upto 60 μm in diameter with varying heights in the peripheral retina (paramacula) [8]. Since the density of photoreceptors decreases in the periphery of the retina, an average of 30-45 photoreceptors overlie each RPE cell. These cells are

tightly packed and, due to this tight junctions in between, forming a part of the blood/retina barrier, blocking the free passage of water and ions. Microvilli, finger like projections, extend from RPE cells into the outer segment of photoreceptor layer. These protrusions (microvilli) help hold the photoreceptors to the RPE. Since, the space between cones and RPE is more than the rods, these microvilli extends further to the cone outer segment.

The RPE plays a very important biological role in the metabolism and biochemistry of the neuroretina. The outermost discs of the rods, made up of lamellar membranes, are continuously shed (phagocytosis of photoreceptors) into RPE, however, cones do not shed in the same manner. Furthermore, the rate of shed for the rods is greatest in the morning while most of the cone activity occurs in the night time. It has been estimated that the same RPE cell must continuously engulf some 3×10^8 discs during a 70-years life time [11]. Photoreceptors are incapable to reisomerize (isomerize is the process in which one molecule is transformed into another molecule having exactly the same atoms, but the atoms are rearranged e.g. A-B-C \rightarrow B-A-C) the *all-trans-retinal*, formed after photon absorption, into *11-cis-retinal*. The RPE play this role, taken up the *all-trans-retinal* from photoreceptors, convert them into *11-cis-retinal*, and is transported back to the photoreceptors, rebuilding the light-sensitive outer segment from the base. The basolateral membrane taking part in the vitamin A cycle, also contribute additionally to this process.

The retinal pigment epithelium also serves as the limiting transport factor that maintains the retinal environment. In one direction, the RPE transport small molecules such as fatty acids (amino acid), retinol and D-glucose from blood to the photoreceptors, on the other hand, is responsible for transporting electrolytes and water from subretinal space to the choroid remaining a tight barrier to choroidal blood borne substances. Furthermore, the secretory function of the RPE helps in maintaining the integrity of the choriocapillaris endothelium and photoreceptors. With these complex functions, normal function of the RPE is essential for the visual system. Damage to this layer can induce failure to any of these functions that can lead to degradation of the retina, loss of visual function, and blindness.

In addition to its important physiological function, the retinal pigment epithelium has a distinctive role in photocoagulation for its light absorbing constituents the melanin, and its critical position between the neural retina and the choroid. About 50-60% of the incident energy in the visible spectrum is absorbed in the RPE which then mostly

dissipated as heat [9]. The portion of transmitted light from the RPE is then absorbed in the less pigmented choroid. Due to the highest concentration of the photon absorbers in the RPE layer, for this part of the spectrum, optically induced damage first occurs in the RPE layer. Following cell death in the RPE, loss of vision is likely to result.

1.4 Composition and Function of Melanin/Melanosomes

Melanins are pigmented chromophores which absorb light in RPE cells. They are packaged in cellular inclusions called melanosomes which by itself is contained inside the RPE cell and has dimension of around 1 μm diameter and 3 μm long. Within the melanosomes, melanins are surrounded by protein-containing coat called “melanoprotein”. The density of the melanin within the melanosomes is so high, as in the bovine RPE cell, that only little structure is apparent. The melanosomes themselves are rather heterogeneous in shape, from spherical to ellipsoid as shown in figure 1.3. The bovine melanosome size ranges from 1 to 5 μm . In normal healthy eye the melanosomes form an absorptive layer of 5 μm in depth at the apical region of the cell, close to the photoreceptors [10].

Retinal premelanosome begin to develop within the RPE cells by budding off of smooth membrane in the Golgi region. The premelanosome contains an abundance of periodically spaced protein filaments. Melanins are deposited on these filaments following the copper-containing enzyme, tyrosinase, (enzyme responsible for the melanogenesis) to the vesicles. Deposition of melanin continues until the melanosome is entirely filled with dense membrane-enclosed particles. No tyrosinase activity can be detected in fully matured melanosome. It appears that mammalian RPE cells exhibit active formation of melanin granule only during the fetal and perinatal period [12].

Perhaps, eye melanin is more important than skin melanin. Because most of the pigmented cells in the eye are non-dividing and practically no melanin renewal is known to occur, showing, that ocular pigmentation is once for life. This is an important biological difference between the skin melanin and the eye melanin. Additionally, the skin melanins are being constantly synthesized by the epidermal melanocytes, transferred to keratinocytes, digested by the lysosomes, and extruded by shedding of dead kertainocytes at the level of the stratum corneum, melanin in RPE, and probably in other pigmented eye tissue, shows very little, if any, turnover [11]. Thus the biological consequences, the structural and functional modification as a result of environmental

insults or simply of aging, in the eye melanin are potentially hazardous than those of skin melanin.

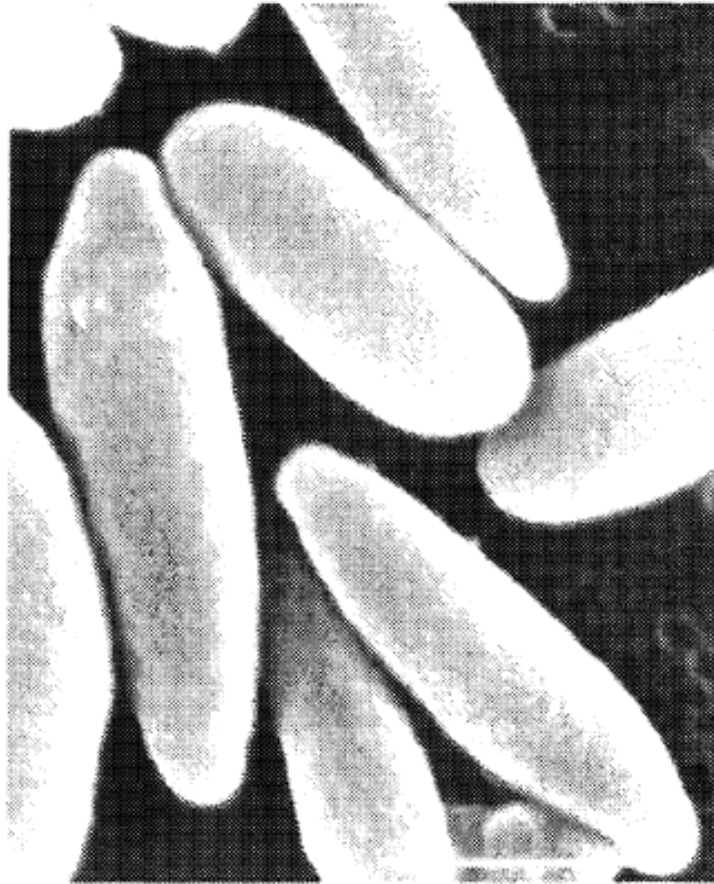


Figure 1.3: Scanning EM picture of the isolated bovine melanosome [13].

Melanins, in the RPE and choroid, efficiently absorbed the incident light, preventing reflection from the fundus, eventually play vital role in improving the visual acuity that may otherwise give rise to spurious signals. Although the primary biological role of melanin except light absorption is still some what controversial, however, theory suggests that melanins are excellent protective organelles due to its photochemical properties. Moreover, very little is known about the exact molecular mechanism of photoprotection by melanin, it is proposed that, this ability of the RPE melanin is related to its anti-oxidant properties. Melanin, due to its excellent scavenging and anti-oxidant properties, play an important role by binding of redox-active metal ions and in the sequestration of harmful photosensitizing agents. Thus, one can say that, a redox-active metal ions or photosensitizing agents presents little threat to the cell as a pro-oxidant, once bound to melanin. Furthermore, studies have shown that, the melanin anti-oxidant capability become less effective or even at some particular stage it becomes

pro-oxidant, when subjected to intense or prolonged oxidative insult. This profound change in the functional properties of RPE melanin may have adverse effect on the integrity and functional performance of the chorioretinal complex and could contribute to the age related macular degeneration (ARMD) [11].

2 Basics of Laser-Tissue Interaction

2.1 Physical Principles Governing Light Tissue Interaction

2.1.1 Absorption of Laser Radiation

When laser radiation is incident on biological tissue, part of the beam energy is reflected, scattered, transmitted, or absorbed. From the laser-tissue interaction mechanisms point of view, it is the fraction of absorbed energy within the tissue which is of interest. The optical absorption properties of the biological tissues are expressed in term of absorption coefficient μ_a . In general, the optical absorption properties of biological tissues are dominated by chromophores such as proteins, melanin, haemoglobin and water. However, their optical activities vary with wavelength as can seen in figure 2.1. Absorption plays a vital role in heating the biological tissue. Hence, the potential of thermal damage relates directly to the absorption coefficient and inversely to the penetration depth.

In the ultra violet (UV) region of the optical spectrum, tissue absorption is dominated by proteins, deoxyribonucleic acid (DNA) and melanin, limiting the penetration depth (the reciprocal of absorption coefficient) to only $\leq 0.5 \mu\text{m}$ for $\lambda \approx 190 \text{ nm}$ to $\sim 200\text{-}400 \mu\text{m}$ for $\lambda \approx 400 \text{ nm}$ [14-16]. At shorter UV wavelengths i.e. $\lambda \approx 190 \text{ nm}$, proteins are the most dominant chromophores. In human tissue, proteins are the second most abundant constituents next to water. At longer UV wavelengths, both DNA (aromatic amino acid residue) and melanin become important chromophores. Melanin absorption is especially important in pigmented tissues such as the skin, iris, and RPE.

In the visible spectral region, absorption in tissue is dominated by haemoglobin and by pigments mainly melanin. Haemoglobin has prominent peak at $\lambda \approx 430 \text{ nm}$, which then drops in the violet and blue region, and again rises in the green spectral part as shown in figure 2.1. Melanin on the other hand, plays a significant role in determining the absorption properties of pigmented tissues such as skin, hair and ocular tissues. The absorption spectrum of melanin drops monotonically in the visible wavelength band such that its absorption at $\lambda = 780 \text{ nm}$ is roughly about 10% of what it has at $\lambda = 400 \text{ nm}$ [17]. A possible explanation to this surprising characteristic of melanin may be their optical scattering contribution to the extinction coefficient, which cannot be easily separated from their absorption properties. Recent studies suggest that the extinction

coefficient in the visible band is mainly due to scattering coefficient which dominates the absorption coefficient by as much as 100 times [18].

In the infrared (IR) regions, water and protein are the main absorbing agents while haemoglobin contributes significantly around $\lambda = 1000$ nm. The absorption co-efficient (μ_a) of water in the Near-infrared (NIR), $\lambda \approx 780$ -1400 nm, is somewhat lower but rises very rapidly with increasing wavelength and reaches its peak value $\mu_a = 12,000$ cm^{-1} at $\lambda = 2.94$ μm [19]. The other chief chromophore in the infrared spectral region is protein. Collagen (a group of naturally occurring proteins) has an absorption peak at $\lambda \approx 6.1$ μm , such that, its absorption peak is greater than water by a factor of 2.

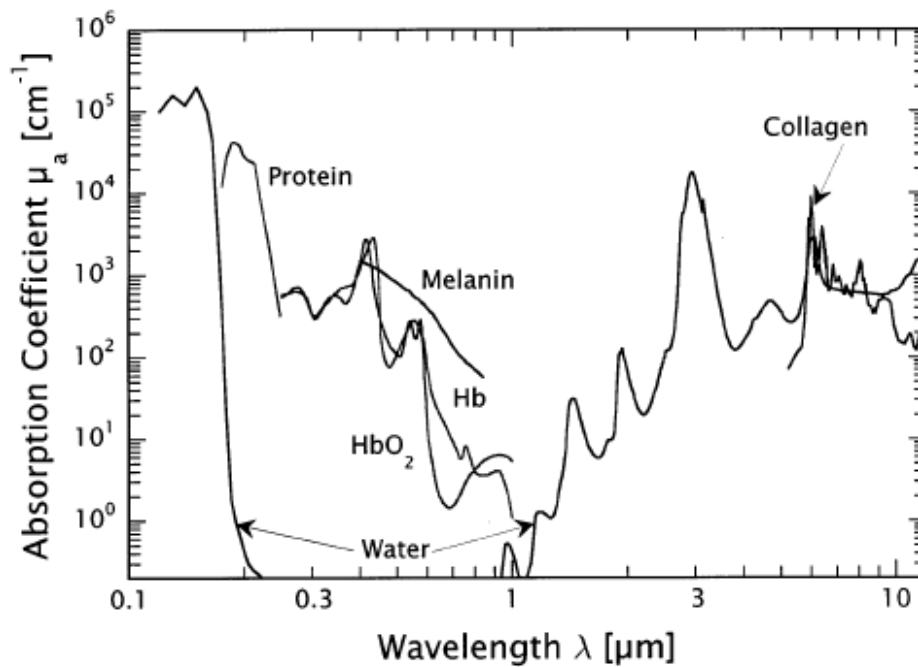


Figure 2.1: Optical absorption coefficient for different chromophores in the wavelength region from 0.1-12 μm [14].

2.1.2 Optical Properties of the Tissue

Light penetration into tissue is an important factor in the evaluation of bioeffects that light produces. Absorption of the incident light in the tissue occurs as a result of resonant coupling i.e. when the photon energy matches with the molecular electronic and vibrational modes. The phenomenon of scattering arises from photon deflection due to change in refractive index or photon interaction with the medium particle. Particularly, the term *Mie scattering* plays an important role in determining the propagation of infrared radiation in tissues, because the cells or organelles sizes are comparable to these wavelengths. The molecules of the target tissue posse an effective

cross sectional area, such that the larger this effective area, the more likely they will absorb photon. The term, tissue optics, indicate the wavelength-dependent properties of absorption and scattering of the tissue that govern light propagation.

Absorption (μ_a) as well as scattering (μ_s) co-efficients, particularly the *effective or reduced scattering co-efficient* $\{\mu_s' = \mu_s(1-g)\}$, are the two most critical tissue optics that determines the volume of tissue affected by light radiation. The term, g , represent the anisotropy which equals to the average cosine value of the photon deflection angle caused by scattering event. The value of anisotropy varies from 0.9 to 0.95 for most biological tissues e.g. the RPE melanin granules have anisotropy of 0.94 [18]. For light propagation through turbid medium e.g. biological tissues, effective scattering co-efficient (μ_s') gives more reliable results than the scattering co-efficient (μ_s) alone. Both absorption co-efficient (μ_a) and effective scattering co-efficient (μ_s') has units of cm^{-1} .

The optical penetration depth, or the distance which light travel into the tissue before its energy density falls to the value of $1/e$, depends on absorption, scattering, and anisotropy. As absorption and scattering depends on wavelength, consequently, the penetration depth also depends on wavelength of the incident light as well as its geometry in the tissue. In another words, optical zone, defines the volume of tissue that absorb the incident light. The optical zone determines, how far light penetrates into the tissue, whether the incident light is a narrowly focused or covers a large area, or whether the incident light is absorbed by a chromophore object in the tissue, in which case the object is the optical zone.

In the back of the eye, the melanin granules rested in the retinal pigment epithelium strongly absorb the visible and near-IR part of the optical radiation band compared to the surrounding tissue absorption [21]. Hence, the absorbed amount of incident light energy determines whether, little or no tissue heating (subthreshold exposure), sufficient heating causing thermal denaturation (threshold exposure), or rapid increase in temperature resulting tissue vaporization (suprathreshold exposure). Moreover, some light exposures may result in tissue damage other than thermal in the optical zone, e.g. triggering photochemical reactions. Thus, the biological tissue response to the incident light depends on the geometry of the optical zone, the wavelength, the amount of delivered energy (or rate of energy in case of continuous exposures) to the tissue, and the exposure duration.

2.1.3 Concept of Energy Confinement

The concept of “energy confinement”, governs the transition between exposures that do not produce tissue damage, those that produce thermal damage, and those that produce photochemical damage. For light energy deposited into the optical zone, whether or not the temperature builds up within the optical zone depends upon the balance between rate of energy deposition and the rate of heat dissipation. If the heat dissipation rate equals to or greater than the energy deposition rate, temperature rise in the optical zone will not occurs, or at least will not exceeds the threshold temperature required for the thermal damage. This illustrates a condition of having no “thermal confinement”. On the other hand, if the energy deposition rate exceeds the energy dissipation rate, temperature will rise in the optical zone until the threshold for thermal damage is reached, and a thermal lesion will results. This state is termed as “thermal confinement”, because heat is retained within the optical zone.

The amplitude and rate of the thermal increase during an exposure determines whether the tissue will undergo for minimal thermal denaturation, coagulation, or vaporization. Similarly, if the rate of energy deposition is extremely higher then the temperature will rises so quickly that thermoelastic shock waves will be induced into the tissue and will leads to a rapid heating-expansion/cooling-contraction cycle. This type of tissue damage is caused by “stress confinement” and is especially associated with bioeffects of short-pulse lasers.

For an exposure duration longer then 10 μ s, damage threshold increases with exposure duration as more energy required and must be deposited into the tissue to counter balance natural cooling due to heat dissipation, thus thermal confinement decreases with increasing exposure duration. For an exposure durations between 10 μ s and 1 ns, all the energy contained in the pulse is deposited into the tissue before thermal diffusion takes place and therefore, the damage threshold remains constant over this time domain. With these short pulses, the temperature raises very quickly reaches to the value of 100°C, consequently tissue water boils and explosive vaporization occurs.

Furthermore, for exposures shorter than 1 ns, the pulse energy is deposited into the tissue in less than the time required for acoustic waves to traverse the optical zone, causing mechanical damage to occur. In this domain of time the threshold damage further drops as can be seen in figure 2.2. Recent work with laser pulses shorter than 100 ps has confirmed the decrease in ocular damage threshold, due to tissue interaction mechanisms associated with extremely high peak power ($>10^9$ W), such as laser-

induced breakdown, beam self-focusing, and multi-photon absorption [22]. The overall laser-tissue damage mechanisms as a function of exposure duration and irradiance is shown in figure 2.3.

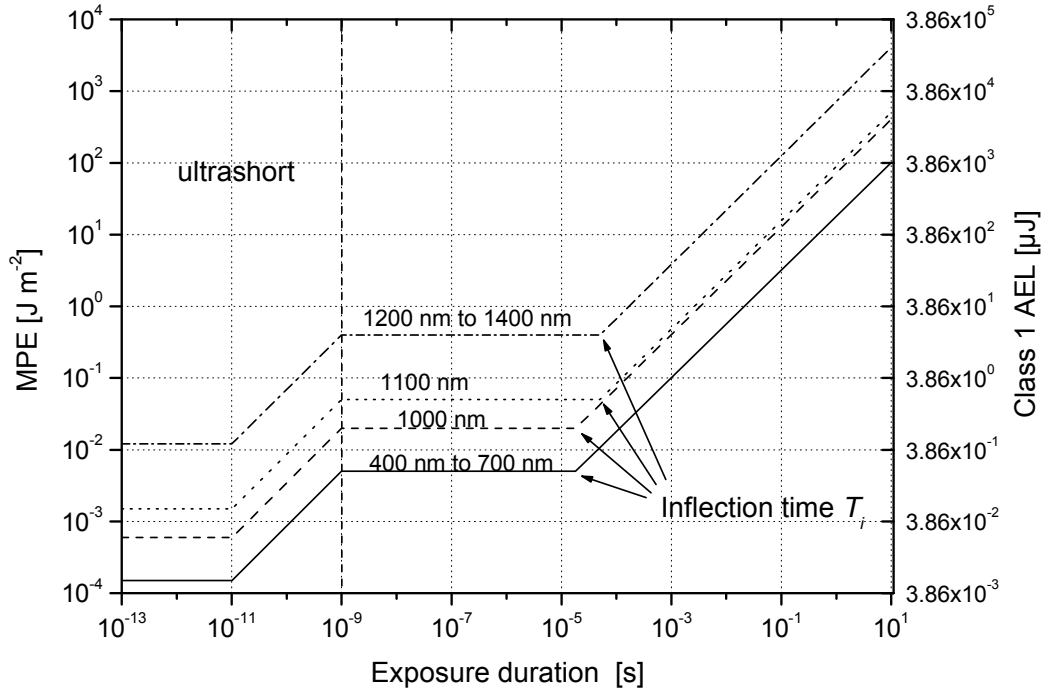


Figure 2.2: Retinal thermal MPE plotted as function of exposure duration for up to 10 s and for a range of wavelengths. The MPE values are given for $C_6 = 1$ and apply to single pulse exposures [3].

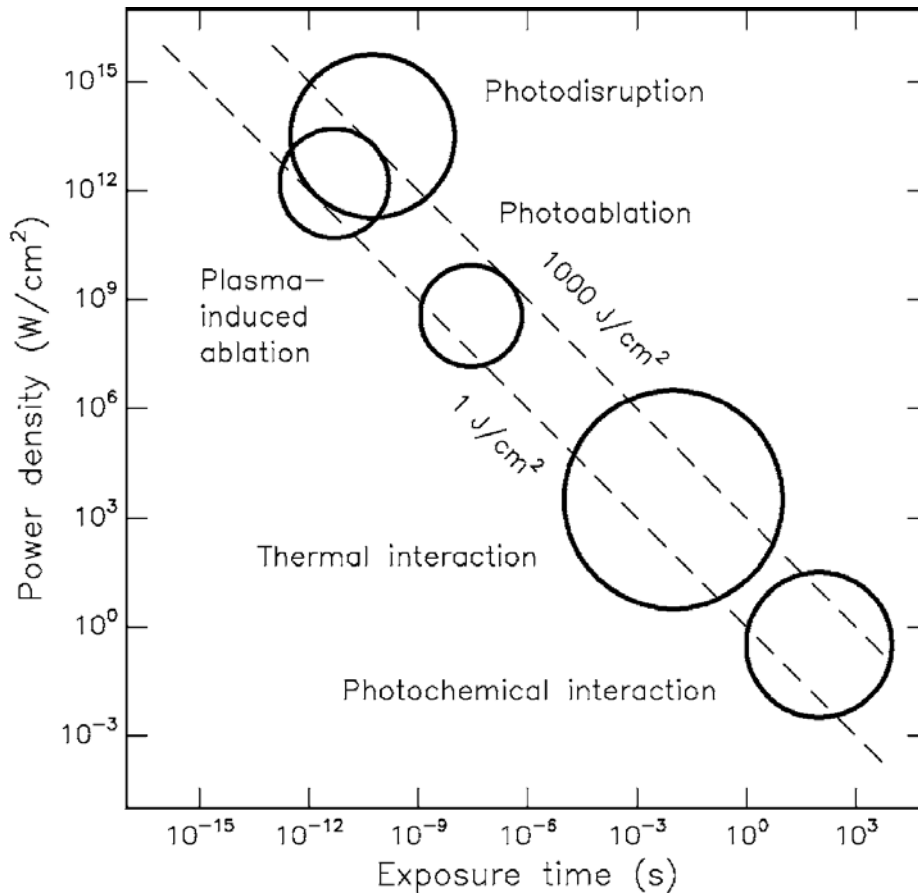


Figure 2.3: Laser-tissue interaction as a function of exposure duration and irradiance [32].

2.1.4 Light Propagation in the Eye

Eye is the most susceptible organ of the body to laser radiation, accidental exposure to which can lead to catastrophic consequences. The eye design is such that the cornea to gather with the lens focuses the incoming light rays and forms images of the object on the neural retina. The central retina known as macula onto which object is imaged is responsible for central acuity and its diameter is only of the order of 350 μm [23]. When a laser beam enters into the eye through cornea, it follows a path such that it passes through the aqueous humor, the lens, and the vitreous humor, and finally reaches to the retina. As already discussed in section 2.1.1, absorption by the surface structures of the eye limits the penetration depth for IR and UV wavelengths, hence no significant amounts of the incident radiation in either of these wavelength regime are expected to reach the retina. Exception is always there for NIR band of the optical spectrum and a weak but potentially hazardous transmission window for the near-UV at $\lambda = 320 \text{ nm}$. It

is because of the imaging function of the eye in the visible part of the spectrum that limits the ocular media absorption in the near-IR as well as in the visible part of the optical spectrum (400-1400 nm), thus making radiation in this part more hazardous for the retina.

Additionally, the focussing property of the eye increases the power density of light on the retina. In the human eye, the effective focal length of the cornea and the lens is approximately 17 mm, and hence focusing the incoming parallel beam entering the eye to an extremely small spot on the retina. For a collimated beam of incident light, and focused to a minimal spot on the retina by the cornea and lens, an increase in the irradiance at the retina may be as high as 10^5 times comparing to the irradiance at the cornea [24]. Thus, an insufficient skin damage radiant exposure when delivered and focus on the retina may indeed cause injury. This is one of the reasons why laser damage threshold for the eye is much lower than for the skin or other tissue. Another consideration for photochemical and photothermal damage is that, light must be absorbed to have a damaging effect. Similarly, the absorption spectrum of each ocular tissue must be taken into account to understand its differential sensitivity with respect to wavelength.

A schematic overview of the propagation of different optical radiation bands through ocular tissue is shown in figure 2.4. The ocular tissues (cornea, aqueous humor, lens, and vitreous humor) are generally transparent only to wavelength in the visible and near-IR bands and their transmission can be seen in figure 2.5. The UV subbands, UV-C ($\lambda \approx 100\text{--}280$ nm) and UV-B ($\lambda \approx 280\text{--}315$ nm), are strongly absorbed by the cornea and lens respectively. Whereas, The Infrared subbands, IR-B ($\lambda \approx 1.4\text{--}3$ μm) and IR-C ($\lambda \approx 3\text{--}1000$ μm) are increasingly absorbed by the water molecules, and hence absorbed in the superficial cornea. Thus, it can be concluded that, cornea is at risk from exposures to UV-C and far-IR wavelengths, lens is susceptible to UV-A and UV-B, while damage to the retina and the choroid results due to excessive visible and NIR exposures.

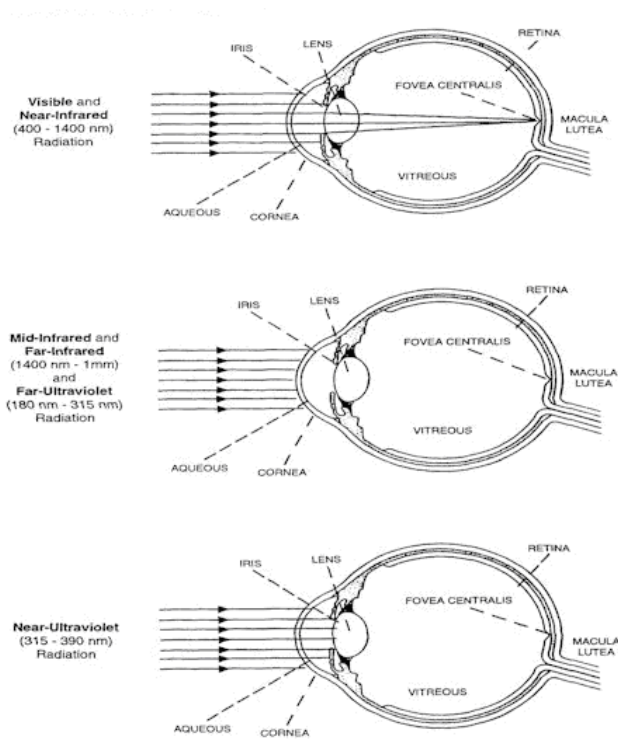


Figure 2.4: Depth of penetration into the eye of different wavelengths of optical radiation. GRM free documentation licence.

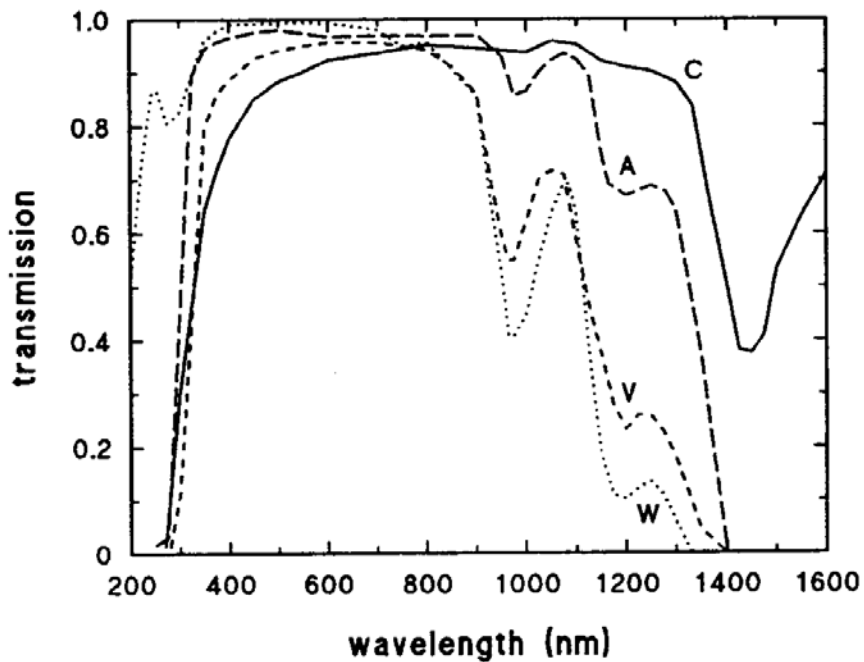


Figure 2.5: Spectral transmission curves of rhesus monkey ocular media. C, Cornea (path length= 0.55mm), A, aqueous (path length = 2.86 mm); V, vitreous (path length = 11.55 mm), and for comparison, the dotted curve, W, of distilled water (path length = 18.5 mm) [25].

2.2 Photochemical Interaction

2.2.1 Photo-Oxidative Effects

This effect arises in results of the incident light with the chromophores in the ocular tissue, causing chemical changes without increasing tissue temperature. This damage mechanism is associated with long exposure duration, short wavelengths ($\lambda \approx 550$ nm or short), and low to moderate tissue irradiance. Because of the inverse relation, short wavelength photons are more energetic, which are necessary to activate chemical reactions, and long exposure duration means to avoid increase in tissue temperature, suppressing thermal damage. The ocular tissue chromophores excitable by short spectral band (UVA and visible) are photoreceptor visual pigments such as heme-proteins, flavo-proteins, and in the RPE, melanin granules and age related lipofuscin. Typically, after photons absorption, these chromophores are excited to triplet state. These triplets are reactive species, and undergo chemical reactions with other molecules.

Sungazing is a classic example of photochemical damage which has been known since antiquity. It has been shown that the temperature increase in the retina during sungazing is at most 4°C, ruling out the thermal damage contribution [59]. Recent studies on solar retinopathy have confirmed that, photochemical process is responsible for solar retinopathy. Retinal damage by prolonged exposure from artificial light sources has also been studied. Rodent models have been extensively used for these studies, in which their retinas were exposed under constant light at relatively low irradiance. The initial damage site reported due to ultraviolet and visible light has varied among investigators. Some were reporting damage in the RPE due to visible exposure [26], whereas others reported damage sites in the retinal photoreceptors [27]. Much important information about photochemical damage have been gathered from these rodent models, yet because of the differences in rodent strains, species differences in the chromophores, it may not be possible to extrapolate entirely to light damage mechanisms in the primate eye.

Lipid peroxidation, particularly damaging in the retina, is also initiated by photochemical interaction, where free radicals, such as singlet oxygen, can attack many molecule types and render them ineffective. Once, one of the $-\text{CH}_2-$ groups in a lipid reacts with free radical, a chain reaction of lipid preoxidation starts that ends eventually in the decomposition of molecule. Protein oxidation is another target of photochemical damage. Many authors have concluded that, chronic blue light exposure initially causes damage in and around the RPE melanosomes results due to the melanin excitation.

Other pigments, such as lipofuscin (age related pigment), probably may also contribute to photo-oxidative stress in the RPE and retina [29-31].

2.2.2 Photosensitized Reactions

In the previous section photochemical damage resulting from the direct interaction of light with endogenous tissue chromophores have been discussed. Same effects might also be produced into tissue by exogenous agents acting as photosensitizer. Photosensitizer is a chromophore compound which is capable of causing light-induced reactions in other non-absorbing molecules. After resonant excitation by laser irradiation, the photosensitizers performs several simultaneous or sequential decays which results in intramolecular transfer reactions. Eventually, these diverse reaction channels results in highly cytotoxic reactants which causes an irreversible oxidation of the essential cell structures. The main idea behind photochemical treatment is to use these chromophores (sensitizers) receptors as a catalyst. These photosensitizers get excited by the absorption of incident photon energy, and their deactivation leads to toxic compounds leaving them into their original state. This type of interaction is also called photosensitized oxidation.

Most photosensitizer chromophores are organic dyes. Their electronic states are characterized by singlet (total electron spin momentum $s=0$) and triplet states ($s=1$). Furthermore, each electronic state contains a band of vibrational states such that within these vibrational states intersystem crossing is allowed. Photosensitizers, after absorbing photons, first transferred to an excited singlet state $^1S^*$, where it decay in three possible ways: nonradiative (heat dissipation), radiative singlet decay to the singlet ground state (fluorescence), and intersystem crossing to an excited triplet state ($^3S^*$) which further decay to the singlet ground state by either nonradiative or radiative triplet decay (phosphorescence). Fluorescence decay life span is of the order of nanoseconds, whereas phosphorescence decay takes up few milliseconds or seconds.

Moreover, there exist two alternative reaction mechanisms for the radiative decay of excited triplet state ($^3S^*$), and based on these two mechanisms retinal photochemical damage is classify either type I or type II. In type I reactions, free neutral or ionized radicals are formed when the photosensitized molecule reacts with molecules of the substrate other than oxygen, which when further interact with triplet oxygen (3O_2) leads to the formation of hydrogen dioxide (HO_2) or superoxide (O_2) anions. In type II reactions, the triplet photosensitizer reacts directly with the triplet oxygen 3O_2 ,

transferred it to singlet oxygen ($^1O_2^*$) which is highly reactive, thus leading to cellular oxidation and necrosis. Usually, these two types of reactions take place simultaneously. Which one is favourable, depends upon the triplet oxygen concentration as well as the appropriate target molecules [32,33].

The type II reaction is exploited in photodynamic therapy (PDT), where a photosensitizer is intentionally introduced into a targeted tissue and then activated by proper light exposure, releasing singlet oxygen that eventually kill or ablate the target tissue. PDT is an emerging clinical treatment modality for cancers and other diseases, and is used in the eye for the ablation of neovascular membranes associated with age related macular degeneration [34]. A schematic overview of PDT is shown in figure 2.6.

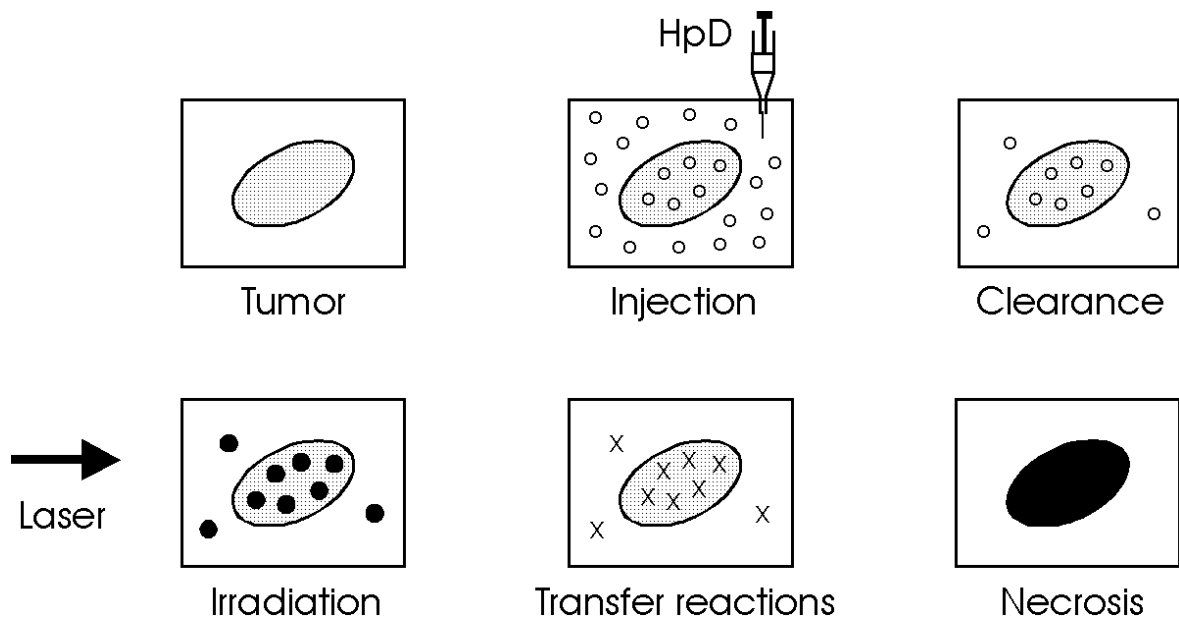


Figure 2.6: scheme of Photodynamic therapy [32].

There are number of invasive and noninvasive measures available for assessing the effects or end points of the phototoxicity of a photosensitizing agent. In the invasive method, histological examination of the affected tissue may reveal the damage site and its extent. The biochemical analysis may also help for damage end points in the excised tissues. On the other hand, there are some suitable noninvasive methods available for investigating ocular toxicity. As discussed photosensitizer reactions consumes oxygen directly or indirectly. Therefore, drug phototoxicity in the eye can be monitored by measuring oxygen consumption. Recent advancement in diode laser sources and electro-optics make noninvasive oximetry method more economical where they uses

NIR light to measure the differential absorption of oxy- and deoxyhemoglobin with good spatial resolution. This approach has great potential in clinical oximetry, but its optical oximetry in avascular or nonperfused tissue, e.g., in the retina away from the retinal vessels needs to provide valid measurements which would eventually make it useful for detecting photosensitizing reactions in the eye [35].

2.3 Thermal Interaction

2.3.1 Rise in Tissue Temperature

For laser radiation in the visible and infrared part of the spectrum, thermal alteration is the dominating damage mechanism in biological tissues. Probably the most thoroughly studied mechanism of injury is that described as thermal. As temperature is a critical parameter in the normal operation of living cells, an increase in temperature can lead to damage consequences. In photothermal interaction, laser light is absorbed by tissue chromophores, convert that absorbed light into heat energy, which rises the local temperature of the target tissue site, and ultimately conducted away that heat to the surrounding tissue i.e. the cooler region. If the temperature or stored kinetic energy of the molecules increases beyond a critical point, they release this extra amount of energy by breaking intermolecular bonds or even intra-molecular bonds. This energy comes from, internal conversion, where excited electronic states decays and releases energy to vibrational or rotational states; or by direct absorption of photon energy into molecular vibration or rotation states followed by nonradiative decay [25].

Interaction between the incident photon and the target molecule A can be considered as a two step process. First, the excitation of target molecule by absorbing photon having energy $h\nu$ and second, inelastic collision of the excited molecule A^* with the surrounding medium partner molecule M, which results in the de-excitation of the molecule A^* and an increase in the kinetic energy of M. Thus, temperature rise microscopically originate from the transfer of photon energy into kinetic energy.

- Absorption: $A + h\nu \rightarrow A^*$
- Deactivation: $A^* + M (E_{kin}) \rightarrow A + M(E_{kin} + \Delta E_{kin})$

The above mentioned two step process need to be considered separately. First, photon absorption by numerous numbers of accessible vibrational-rotational states of most biomolecules, Secondly, the channels available for deactivation or thermal decay are also numerous, because the incident photons energies (Er-YAG laser: 0.35eV, Nd-YAG

laser: 1.2eV, ArF laser: 6.4eV) are well above the kinetic energy of the target molecules at room temperature which is only about 0.25eV [32]. Thus, both of these steps are highly efficient for proper exposure duration.

Absorption plays an important role in tissue temperature rise. The lower the absorption coefficient value of the tissue is, the more will be the penetration depth (reciprocal of absorption). Hence, tissue with low absorptivity will not be heated as much as tissue with high absorptivity, for the same amount of radiations. Consequently, for the same irradiance level as well as exposure duration, the magnitude of thermal damage is directly related to the absorption coefficient and inversely related to the absorption depth. Thus, the potential of thermal damage in tissue, depending on the exposure duration and peak temperature achieved, can be different. The cell nucleic acids seem to be relatively stable with respect to temperature (80°C at time up to an hour) [37]. Hyperthermia starts when body temperature increases to around 45-50°C. If hyperthermia lasts for several minutes it can lead to tissue necrosis. At temperature around 50°C enzyme inactivation occurs and certain cellular repair mechanisms are disabled [36]. Above 60°C photothermal injury becomes irreversible where protein denaturation leads to coagulation. Beyond 100°C tissue water get vaporized which leads to the consequences of carbonization, melting and ejection of tissue fragments into free space, commonly referred as ablation [32] and can be seen in figure 2.7.

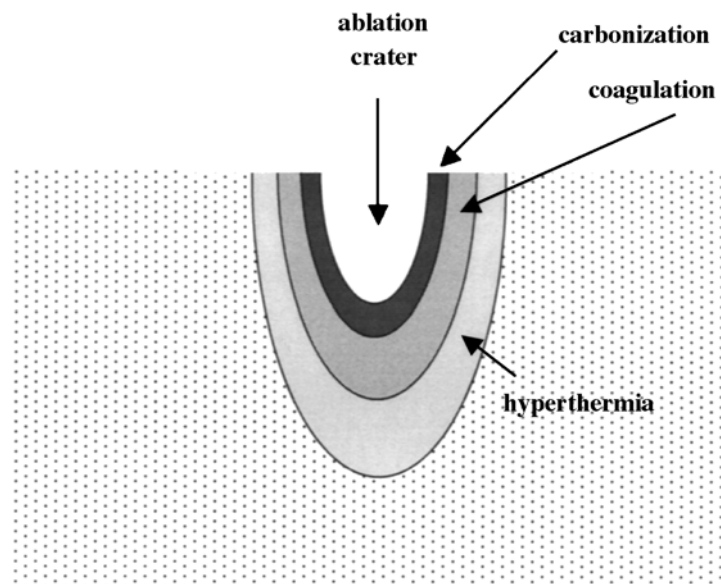


Figure 2.7: Schematic representation of photothermal phenomena inside biological tissue after laser irradiation [32].

2.3.2 The Protein Denaturation

Thermal injury ensues when enough radiant energy is absorbed within the tissue to create or sustain, at least for some seconds, a substantial increase in normal tissue temperature. It is generally assumed that temperatures 10 to 20°C above body temperature produce irreversible thermal denaturation in sensitive macromolecules (mostly proteins) with resultant polymerization and/or coagulation. The extent of thermal injury in tissue is proportional to the magnitude and duration of temperature increase, or its “time-temperature history”. For example, when a volume of tissue is heated to a temperature, T_1 , for exposure time, t_1 , similar results may be obtained if the same tissue is heated to a lower temperature, T_2 , for a longer period of time, t_2 .

Proteins are the major structural molecules of most biological tissues and are held in a highly specific configuration by hydrogen bonds and Van der Waals forces. These bonds are relatively weak and get destroyed by heating. If these bonds are broken due to heating, proteins may uncoil or recoil into new configuration, which could disabled any useful function that the protein had, referred to as denaturation or coagulation. In a highly specialized tissue such as the retina, damage that leads to cell death in any layer is readily spread to other cells whose existence depends on the damage cell [38].

Thermal denaturation is a rate process i.e. the ability to transform a tissue from a native to a denatured form depends not only of the irradiation time but also on the elevated temperature achieved during irradiation. The biological tissue may be characterized as having a particular native macromolecules “ N_0 ”. Due to absorption of laser radiation, tissue is heated, thermal denaturation proceeds, and the number of native macromolecules “ $N(t)$ ” decreases with time. Thermal damage can be described by the term “ Ω ” called “damage integral” which can be written as:

$$\Omega = -\ln\left[\frac{N(t)}{N_0}\right] = \int_0^t k dt' \quad (2.1)$$

Before denaturation “ Ω ” is zero. When 63% of the tissue molecules have been denaturated, “ Ω ” value is unity. When all the tissue molecules get denaturated, “ Ω ” value approaches to infinity. The value of rate constant “ k ” is temperature dependent. Higher temperature requires less time to coagulate a certain amount of molecules (large k), while low temperature requires longer time (small k). In general, the lower the threshold temperature, the more important is the exposure duration, while, the higher

the threshold temperature, exposure duration is less important and peak temperature is more important [20].

2.3.3 Thermal Confinement Time

Thermal confinement occurs when the laser pulse is sufficiently short that its energy is deposited in the optical zone such that heat diffusion from that zone can be neglected, or, the temporal duration during which heat is confined within the heated volume and heat diffusion is negligible. Generally, the relation for thermal confinement time or relaxation time can be written as:

$$\tau_{conf} = \frac{\delta^2}{4k_{therm}} \quad (2.2)$$

Where δ [m] is the penetration depth (reciprocal of the absorption) and k_{therm} [m².s⁻¹] is the thermal diffusivity. The value of k_{therm} is approximately same for liquid water and most of the biological tissues. For water at 37°C, the value of k_{therm} is 1.5 x 10⁻⁷ m² s⁻¹[3]. For a given tissue, under thermal confinement condition, the maximum pulse duration depends strongly on the penetration depth which in turn depends on the wavelength. For deep penetration depth a large volume is heated and heat diffusion to the adjacent structures is slower than for low absorption depth where heat diffuses much faster and the temperature decreases much rapidly. Furthermore, for pulse duration less than the confinement time, the peak temperature achieved in the tissue is independent of pulse duration, but only depends on the amount of energy delivered into the tissue. Therefore, in this time domain, constant radiant exposure limits are defined with no time dependence as can be seen in figure 2.2.

For tissue with certain absorption coefficient, confinement time defines the extent of damage. If the total pulse energy is delivered to the tissue in time much shorter than the thermal relaxation time, damage will be confined to the penetration depth only. The magnitude of pulse energy will determine the tissue damage i.e. coagulation or vaporization. Whereas, if the exposure duration is longer than the thermal confinement time, significant amount of heat will be diffuse to the adjacent tissue structures than the original target volume during irradiation, hence the efficiency of achieving peak temperatures reduces in the target tissue site and comparatively little damage may be found in the target tissue [39]. Generally, for definite effects, it is desirable to achieve peak temperatures in the target tissue sites only, sparing the surrounding tissue. In tissue thermal ablation, pulse duration is adjusted keeping in mind the thermal relaxation time

order to minimize thermal damage to the adjacent structures. For thermal ablation confinement time is very important, as it measures the thermal susceptibility of the tissue.

2.3.4 Damage Criterion to the Eye

Retinal thermal damage can only be possible if the temperature of target tissue site raises, i.e., thermal damage cannot happen unless and until, the energy delivered to the tissue volume is faster than its leaks away (dissipation) which will ultimately raises the tissue temperature leading to thermal damage. The criterion for thermal damage at any point(s) \mathbf{r} , as a function of temperature and the temporal duration, is expressed by a single parameter $\Omega(r)$, and can be calculated from the Arrhenius damage integral.

$$\Omega(r) = \sum_p A_p \int_0^t \exp\left[-\frac{E_p}{RT(r,t)}\right] dt \quad (2.3)$$

Where, the two constants A_p [s^{-1}] and the term $\exp(-E_p/RT)$ gives the rate of the p th damage process. For thermal damage in the laser irradiated eye, the values of A and E assuming a single damage process are $1.3 \times 10^{99} s^{-1}$ and 1.5×10^5 cal. mol $^{-1}$ respectively [40]. Generally, the value of $\Omega(r)$ is set to unity for determining the threshold for irreversible damage i.e. $\Omega = 1$. The criterion of $\Omega = 1$ would imply that 63% of the native molecules have been denaturated.

Thermal induced damage is a function of both the initial events caused by the radiation absorbed in the tissue and its response, which can be described as biological amplification of the damage site, as they extend outside of the irradiated area [41]. In the visible wavelength region melanin, contained in the melanosomes found in the RPE, is the main source of absorption, which absorb approximately one-half of the light reaching the retina. The remaining of the light is absorbed by ~ 170 μm thick choroid [42]. This absorption of the melanin granules in the RPE cells results in heat generation, passing these thermal transients to the pigment epithelial cell, the superficial elements of the choroid and towards the tips of the overlying photoreceptor cell outer segments. This temperature transient denaturises the proteins present in outer segments of photoreceptors. If a critical volume of the photoreceptor outer segments damaged the whole cell may die [43]. Moreover, since the RPE act as barrier between the photoreceptors and the choroid, controlling the free diffusion of unwanted metabolites from the choroid vessels into the neural retina and pumping the required moeties to the

photoreceptor cells. Damage of the pigment epithelium will result in loss of both the barrier and transport processes.

For radiation absorption in NIR region, the origin of heat source leading to thermal damage is not only the melanin in RPE, but contribution from melanin in the choroid has to be considered too. This is because; the absorption coefficient of RPE decreases more drastically for wavelengths from UV to NIR as compared to the absorption coefficient choroid. For example, for negro, in the wavelength range from 400 nm to 1060 nm, absorption coefficient of choroid decreases from 240 cm^{-1} to about 106 cm^{-1} , whereas, that of the RPE decreases from 1838 cm^{-1} to 131 cm^{-1} [44]. Consequently, the damage threshold for near infrared wavelengths increases because of, the lesser amount of energy absorbed in the RPE, and the scattering effect in the choroid, where the incident energy is absorbed into a larger volume. For wavelength in the visible range, scattering effects due to neural retina has consequences on the damage threshold. The scattering phenomenon is particularly important for small beam diameters.

2.4 Photoablation

Photoablation was the term which was used to describe the unusually clean, precise, and nearly damage free ablation, when intense pulses of ultraviolet radiation from ArF excimer laser were applied to biological tissues [45]. For available laser sources in the UV wavelength region, photons have sufficiently high energy (4-6.5 eV/photon) comparing to the dissociation of many organic molecules, to break their chemical bonds. If these UV photons are delivered to the tissue in the time frame of ns or less, tissue may be removed precisely. Typically, the photoablation threshold value for ns pulses in the UV region is in the range of 10^7 - 10^8 W/cm^2 .

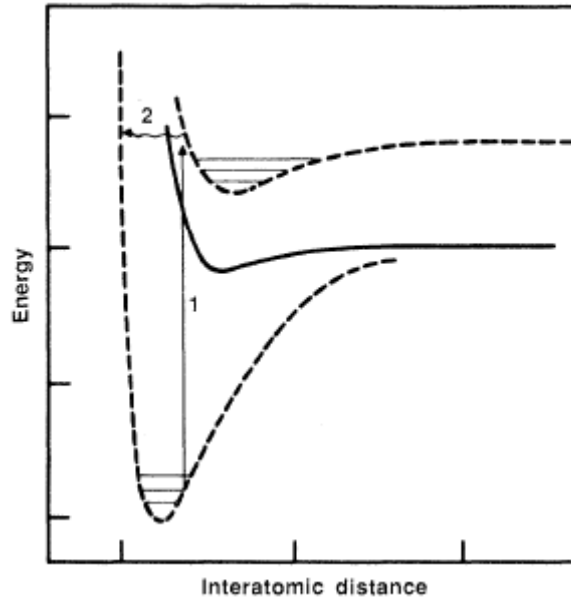


Figure 2.8: Energy level diagram of hypothetical bond A-B. Lower dash line represent ground electronic state, while upper dash and solid lines represents excited electronic states [46].

It is generally accepted that UV photon absorption results in electronic excitation (path1). This excited electronic state may undergo decomposition purely photochemical in that state or, to vibrationally excited ground state as a result of internal conversion (path2), which is the possible basis for photothermal ablation mechanism shown in figure 2.8. In either case the fragments remain same and the electronic energy exceeding the binding energy of molecules contributes to the kinetic energy of the ablated fragments. Regardless of pathway, the ablation that occurs on the time scales that are comparable to the pulse duration (~ 20 ns), thermal diffusion and hence thermal damage to the substrate is minimal, provided that penetration depth is small. Experimental studies on thermal loading have shown that, the deposited energy below the ablation threshold is totally converted into heat, while if the radiant exposure is above the ablation threshold, thermal energy in the substrate increases very slightly, indicating that the excess photon energy is contained in the ablated fragments [47].

In the mid of 1980s, interests had been shown in using pulsed infrared (IR) lasers such as TEA-CO₂ ($\lambda = 10.6$ μm) and Q-switched Er:YAG/YSGG ($\lambda \sim 2.8\text{-}3$ μm) instead of using UV excimer lasers ($\lambda \sim 190$ nm) for tissue ablation. The purpose was, since these lasers were easy to use and maintain, efficient, shorter pulses readily available, and have optical penetration depth in tissue comparable to those of excimer lasers. Several studies

had been performed to compare their tissue effects with the excimer lasers results, which concluded that, UV lasers can cut tissue more cleanly with minimum thermal or mechanical damage than IR lasers, where more thermal injury and tissue tearing in the adjacent tissue was observed. For example, ArF-excimer laser ablation with optical penetration depth of about $\sim 4 \mu\text{m}$ leads to a zone of thermal injury of $0.3 \mu\text{m}$ [60], whereas, Q-sw Er:YAG/YSGG laser having penetration depth of around $\sim 1 \mu\text{m}$ results in a zone of thermal injury 2-4 μm wide [48].

Many investigators have postulated that these differences in the tissue morphology are due to differences in ablation mechanism and/or the dynamics of tissue optical properties. One common argument explaining the ablation achieved by UV and IR is that, tissue removal produced by UV wavelength is mediated by photochemical process enabling direct scission of chemical bonds in the cornea, whereas, IR ablation is governed solely by the thermal processes. Moreover, UV laser ablations do not exclusively involve photochemical dissociation but thermal processes are also present, and that contribution from photochemical decomposition to the ablation decreases with increasing wavelengths. In general, ArF excimer laser ($\lambda = 193 \text{ nm}$) has been found to be suitable than other UV or IR lasers used for ablation purposes in ophthalmology for corneal refractive power correction [56,57].

2.5 Plasma-induced Ablation

Plasma-induced ablation is a nonlinear absorption process that is achieved by short intense laser pulses from Q-switched or mode-locked lasers. This nonlinear absorption process makes it possible to deposit laser energy within the spatially limited regions not only in pigmented tissue but also in the transparent tissues like cornea, lens or in other part of the ocular media. For plasma induced ablation the most important parameter is the electric field strength E which determines when an optical breakdown is achieved. The optical breakdown occurs when E exceeds a certain threshold value. The electric field strength and optical power density I are related to each other as:

$$I(r, z, t) = \frac{1}{2} \epsilon_0 c \vec{E}^2 \quad (2.4)$$

Where ϵ_0 is the dielectric constant and c is the speed of light. Some authors have demonstrated that at light intensities above approximately 10^{10} W/cm^2 [32], formation

of plasma via “inverse bremsstrahlung” and cascade ionization occurs in transparent media like water or ocular media, which form the basis for plasma-induced ablation [49].

Whereas optical breakdown in gases leads to the generation of free electrons and ions, in liquids the electrons are bound to either a particular molecules or “quasi free” where they possess sufficient kinetic energy to move freely without being captured by local molecular energy potential. If some free electrons are available in the medium, they absorb photons by collision with atoms, and may ionize an atom by impact after getting high energy than the ionization potential of that particular atom. An ionization cascade leading to the formation of plasma begins when free electron density reaches between $10^{18} - 10^{21} \text{ cm}^{-3}$ during the laser pulse [58]. Good agreement between experimental and theoretical threshold values for the optical breakdown in pure water was observed for critical electron densities $\rho_{\text{cr}} = 10^{20} \text{ cm}^{-3}$ for ns pulses and 10^{21} cm^{-3} for ps and fs pulses [61]. The seed electrons for the ionization cascade are either generated by thermionic emission by heating the linear absorbing chromophores in the target volume (liquids impurities), or by multiphoton ionization. It was observed that, in Q-switched laser pulses the initial process for the generation of free electrons is supposed to be thermionic, whereas, in mode locked laser pulses multiphoton ionization is responsible. The multiphoton ionization rate is proportional to I^k ; where I is light intensity and k is the number of photons required for ionization.

Once a free electron exists in the medium, it gains kinetic energy by absorbing photons through “inverse bremsstrahlung” process in collision with heavy charge particles to conserve energy and momentum. After a sequence of k inverse bremsstrahlung absorption events, the free electron kinetic energy exceeds the band gap energy, and release another free electron through impact ionization. If the irradiance is high enough to overcome free electron losses, an “avalanche ionization” or “cascade ionization” will result, as can be seen in figure 2.9. Although multiphoton ionization is “instantaneous”, there are time limitations on cascade ionization as several inverse bremsstrahlung events are necessary for a free electron to pick the required kinetic energy for impact ionization. In condensed matter the collisions time τ , of the electrons with the heavy particles, is of the order of 1 fs.

Several authors have demonstrated experimentally that the optical breakdown threshold of water is similar to that of transparent ocular and other biological media such as cornea, vitreous fluid, and saline. Similarly, for pulse duration ≤ 200 ps, multiphoton

absorption is high enough that the optical breakdown process no longer depends on the impurities present in water e.g. the threshold for tap and distilled water are same. For ns pulses, distilled water threshold is lower than the tap water due to absorbing impurities present in tap water, which provides seed electrons for cascade ionization [50].

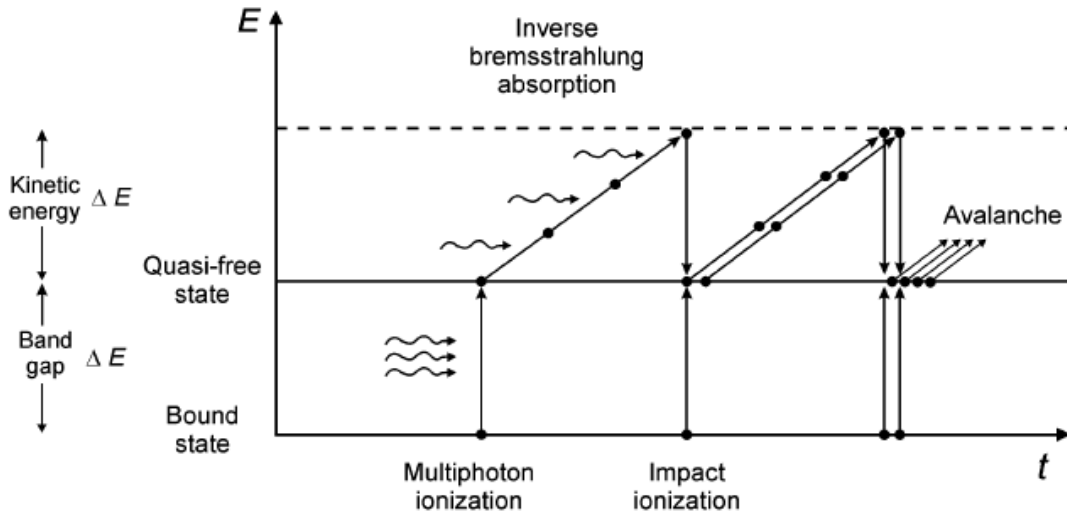


Figure 2.9: Interplay of multiphoton and avalanche ionization in the process of plasma formation [51].

In particular, the important feature of plasma formation is the highly localized energy deposition by short laser pulses, ns or less, independent of the absorption coefficient of the target tissue, and thus ideal for non-invasive microsurgery in transparent media such as eye. The volume of energy deposition can be controlled by focusing the laser radiation, because plasma formation occurs only at locations where the irradiance threshold of laser-induced optical breakdown is exceeded. The high temperature as well as pressure of the plasma drives the rapid expansion of plasma generating a high pressure front. The expansion of plasma slows down as plasma temperature decreases and the high pressure front separates to form shock waves. The expansion of the bubble continues until the pressure reduces to the point where the bubble implodes due to the external pressure of the liquid [52].

2.6 Photodisruption

As already described in previous section, plasma formation due to optical breakdown is coupled with shock waves upon bubble collapse. In soft biological tissues and fluids,

bubble generation, and jet formation additionally takes place. These entire effects take place at different times as can be seen in figure 2.10. In photodisruption, the amount of energy absorbed is two or more orders of magnitude higher than in the plasma-induced ablation. Thus, in photodisruption, the free electron density as well as plasma temperature is higher than in the purely plasma-induced ablation. Photodisruption is a non-linear absorption process leading to plasma formation at the laser focus, especially for ns and ps pulses, where plasma temperature exceeds several thousand °C.

In photodisruption, mechanical forces are responsible for tissue ablation. As plasma-induced ablation is confined to the breakdown region, shock wave and cavitation effects propagate to the nearby adjacent structures, thus limiting the local interaction zone. For nanosecond pulses, optical breakdown is always coupled with shock waves even at the very threshold. The damaging effects of these shock waves to the adjacent tissue sites are undesirable. On the contrary, with ps and fs, optical breakdown is achieved with significantly reduced plasma energy, thus limiting the disruptive effects to the nearby adjacent structures. Initially, in the 1970s decade, all tissue effects produced with ultrashort laser pulses were attributed to photodisruption, but recent studies clarify between ablation due to ionization and ablation due to mechanical forces [54].

Similarly, the rapid adiabatic temperature rise during optical breakdown causes an equally rapid pressure rise 20-60 kbar [53] within the plasma, leading to an explosive expansion of plasma. Initially plasma expands with hypersonic velocity, and a shock wave is generated when plasma expansion is reduced to subsonic values. Subsequently, a cavitation bubble is produced by the still expanding plasma. Within a time scale of ms, the bubble collapses as a result of the outer static pressure of the liquid, and upon bubble collapse pressure and temperature rise again to a value similar to that achieved during optical breakdown resulting in a second transient. Jet formation occurs when the bubble collapses in the vicinity of a solid boundary, and it can cause high pressure impact against the wall, if no water layer exists between the bubble and the solid boundary [55].

Moreover, the lengths and thus volumes of the plasma induced by ps pulses are longer than those induced by ns pulses for the same energy. This difference in plasma volume results in a considerably lower energy density for ps pulses. The reduction of plasma energy density with decreasing pulse duration best explains the strong reduction of mechanical effects associated with ps pulses or less as compared to ns pulses. Furthermore, the plasma volume determines the fraction of incident energy to be converted into shock waves or cavitations. For large plasma volume, as induced by ps

and fs pulses, more energy is required for ionization and evaporation of the tissue. Hence, this amount of energy is no longer available for the generation of shock waves or cavitations. As a result, the plasmas induced by ps pulses are less likely to cause mechanical tissue damage than plasmas from ns pulses [32].

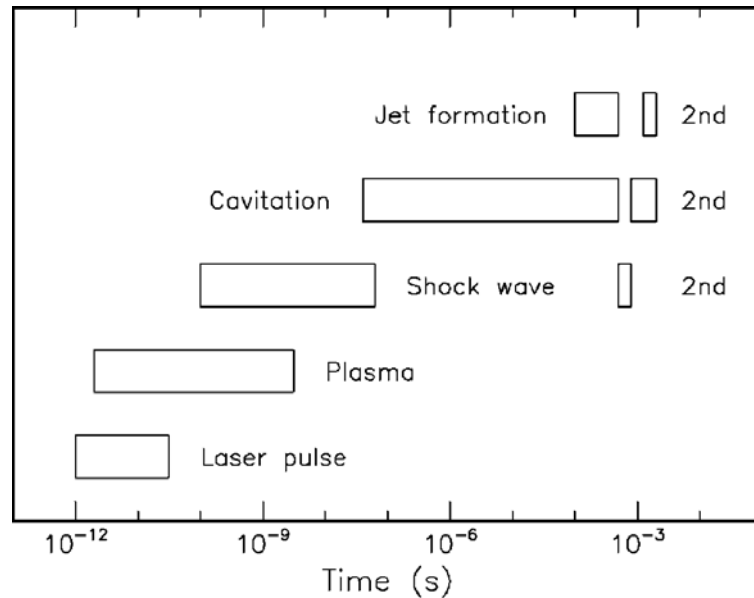


Figure 2.10: Approximate time scale of different processes in photodisruption for 30 ps pulse. Shock wave, cavitation and jet formation are indicated. [32]

Generally, the temperature rise in plasma is determined by volumetric energy density gained during laser pulse. Femtosecond laser pulses are considerably shorter than the cooling or recombination time of the electrons. Therefore, energy diffusion is minimal during laser pulse, and the energy density deposited during exposure in irradiated volume is given by the product of the total number of quasi-free electrons and mean energy gain of each electron. For pulse duration longer than electron-cooling time (several ps) or recombination time (several ten ps), an equilibrium established between energy loss and gain during pulse irradiation. That's why, the required energy density for plasma increases with increasing pulse durations as shown in the below figure 2.11.

The strong nonlinear dependence of plasma free electron density on irradiance enhances the possibility for localized energy deposition within the target volume, and hence large ablation depth can be achieved with little thermal damage to the adjacent tissue. Thermal effects are negligible for single pulse exposures, regardless of the pulse duration. For example, with ns pulses, the thickness of thermal damage layer in corneal

tissue remains $< 1 \mu\text{m}$ [53]. However, when ultrashort pulses are applied with high repetition rate, heat accumulation in the nonablated tissue may increase the thermal damage zone. Thus, when fs pulses are used, the target is heated in regions where ablation threshold is not exceeded. For ns pulses, the sharp decrease in electron density for irradiances below optical breakdown threshold prevents heating of the nonablated tissue.

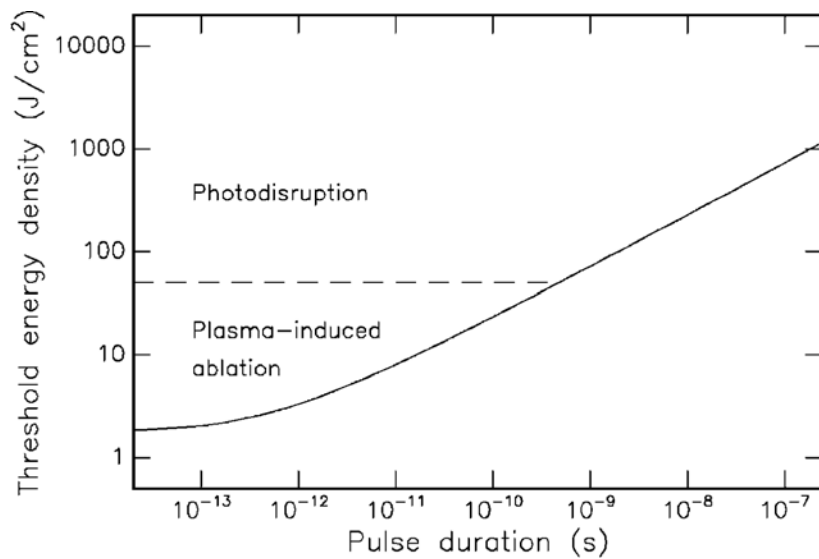


Figure 2.11: Distinction of plasma-induced ablation and photodisruption according to applied energy density [32]

Photodisruption has become a well established tool and has found considerable use in recent years known as laser microsurgery, especially in the procedures of iridotomy improving the drainage of the posterior chamber and posterior capsulotomy of the lens. Laser photodisruption has been used farther back in the eye, but the secondary damage problem to the retina cannot be ignored. Because of the precise nature of lesions formed in photodisruption, this technique might be considered workable for removing epiretinal membranes with proper selection of laser parameters and knowledge of extended damage beyond the target tissue. Beam geometry play an important role, as it has to be focused at the target site to generate plasma, in determining the location of plasma, beam expansion beyond the focal region, and thus irradiance at the retina.

3 Exposure limits

3.1 The Concept of Threshold and Safety Factor

In the field of health and safety, more emphasis on laser radiation is because of its low beam divergence, which together with high energy content can result in an excessive amount of radiation transferred to biological tissue. This emphasis even further increased for visible and NIR radiation due to the transmission of ocular media and eye optical focusing system for this particular band of radiation. To protect individuals from the hazards of laser radiation, exposure limits known as *maximum permissible exposure* or shortly MPE's draw a boundary between those known as hazardous for the eye or the skin and those considered safe. These MPEs (Exposure Limits "EL" in the ICNIRP documents) are set by the International Commission on Non-Ionizing Radiation Protection (ICNIRP) [62], and adopted by safety standardization committees of the International Electrotechnical Commission (IEC 60825-1) [63] as well as American National Standards Institute (ANSI Z-136.1) [64]. The basic purpose of these guidelines is to establish principles of protection against laser radiation. These guidelines are based on an international consensus on the health effects and hazards of laser radiation.

The eye and skin are the organs most susceptible to damage from laser radiation. Adverse health effects due to laser radiation are theoretically possible for the entire optical spectrum ranging from 180 nm to 1 mm, but visible and NIR wavelength region (400 - 1400 nm) is of the primary concern because the consequences of overexposure of the eye are generally more serious than those of the skin. Because most of the MPEs data are derived from animal experiments and data available from human volunteers are very limited in number, hence extrapolation from animal experiments to effects on humans has to be made. Moreover, these limits should provide an adequate level of protection such that repeated exposures would not lead to acute or delayed biological effects.

In describing the adverse biological effects of optical radiation, a linear hypothesis applies with total integration of the lifetime exposure. Optical radiations are generally absorbed in a thin layer of tissue and their effects are mostly thermal in nature except for ultraviolet and visible photochemical processes for wavelengths < 550 nm. All thermal injuries have definite threshold. Photons in the long wavelength region of the optical spectrum do not have enough individual energy to cause biological changes at

molecular levels. Only a sufficient photon flux can overcome the normal repair processes of the molecules or can rise the temperature of the exposed tissue so rapidly that the repair processes seized up. On the other hand, photons in the short wavelength region do have sufficient individual energy that may change or damage individual in a critical biomolecules such as DNA if overwhelm the repair mechanism of DNA [65]. Therefore, high photon flux density is required to overcome these repair processes and have a macroscopic level damage.

In both these acute effects, tissue repair mechanisms results in a definite threshold, below which no adverse change will occur. These thresholds are varying for individual as well as for the environmental conditions. However, safety limits, *Maximum Permissible Exposure*, are set well below the thresholds (ED50) such that these variations are overcome and the exposures at the *MPE* are not hazardous. Safety limits are set for any radiation in which the reciprocal relation exists. At threshold level increase in exposure duration may not be followed by pathological changes in the target tissue. However, there may be some finite, although small, risk of injury or delayed effects exist in a small population.

In Experiments, damage threshold are determined for a verity of laser parameters e.g. fixed wavelength, exposure duration, and spot size, but varying pulse energy delivered to biological tissue (e.g. the retina, the cornea, or the skin). After irradiation, each exposed site is examined for the presence or absence of changes in appearance or possible detectable lesion. The ‘Effective Dose 50%’ or simply ED50 (the dose at which 50% of the population lead to lesion) also referred to as ‘threshold’ is determined from this lesion and no lesion data using does-response curve. The ‘*Maximum Permissible Exposure*’ MPE’s are then derived from the ED50 using the *safety factor*, which specify the level above which the irradiance may lead to an injury or any other effects, and below which exposure remain safe for that specific circumstance [3]. For visible wavelength region, the safety factor, the ratio of ED50 to MPE, is for minimal retinal spot sizes usually set to the value 10 or even more in some cases (depending mainly on wavelength). For extended sources, the safety factor (or “reduction factor”) can be smaller than 10. Also for UV-induced corneal photochemical injury, however, the value of safety factor is less than 10 because of the small uncertainty and variability in the experimental data.

3.2 Dose-Response Curve

In studying laser-induced damage threshold of biological tissue particularly the skin and the eye, dose-response curve or “probit plot” is commonly used for presenting experimental results. The most important point considered on the dose-response curve is the dose which corresponds to 50% probability of injury: the ED50. This value of ED50 is frequently referred to as “threshold”, although there are some damage points below this threshold. In experiments, to determine threshold or energy value which produces *minimum visible lesion* (MVL) for a given wavelength and exposure duration, it is generally accepted that this threshold varies from species to species, and also for exposure sites within the tissue, especially if it is the retina. As a result, the experimental threshold data are analysed on the basis of dose-response concept. In health physics and toxicology, dose-response curve describes the change in effect on biological tissue caused by different levels of exposures or doses. In laser safety the same dose-response concept was adopted, where the response is of yes/no type, or lesion/no-lesion, and is known as quantal response. On the contrary, in graded response, an increase in the dose produces a gradual change of the observed phenomenon.

Theoretically, for a given exposure conditions, an exposed tissue site will have a certain sharp threshold dose: below which no response while above a response is observed as can be seen in figure 3.1. However, practically such a sharp threshold for a given tissue site is not possible, because, any particular site in tissue can only be exposed once which may lead to damage or at least changes the properties of that specific tissue site. Therefore, in laser damage threshold studies, different tissue sites of the same individual or same tissue site of different individuals are exposed for a given exposure conditions. The responses of different tissue sites as well as different individuals are different. For a given exposure conditions, those tissue sites and individuals which have lower threshold damage than the level of exposure or dose will result in a lesion. If the response axis is defined as the relative frequency (percentage), the dose-response curve changes to a uniformly continuous function as shown in figure 3.2.

For laser-induced retinal damage threshold measurements i.e. ED50, laboratory animals, mostly the rhesus monkeys, due to ocular media very close to that of the human, are exposed under controlled conditions. Direct observation of the exposed tissue sites are oftenly made with ophthalmoscope or slit-lamp microscope. Some experimentalists use fluorescein microscopy, in the case of *ex-vivo* explant tissue, for MVL observation (as

used in this study), while some others uses fluorescein angiography or even electron microscopy for examining the exposed tissue site in order to improve lesion visibility. Although, fluorescein angiography and electron microscopy are much sensitive techniques compare with ophthalmic microscopy but are more costly and hence less practical. Studies have shown that, ED50 determined with fluorescein angiography or with electron microscopy is lowered utmost by factor of 2 when compared with ophthalmoscopically determined ED50 [66]. The slope, another important parameter of the dose-response curve, not only reflects the variation in individuals, but also a good indication of the experimental uncertainties as well as quality of the experimental data.

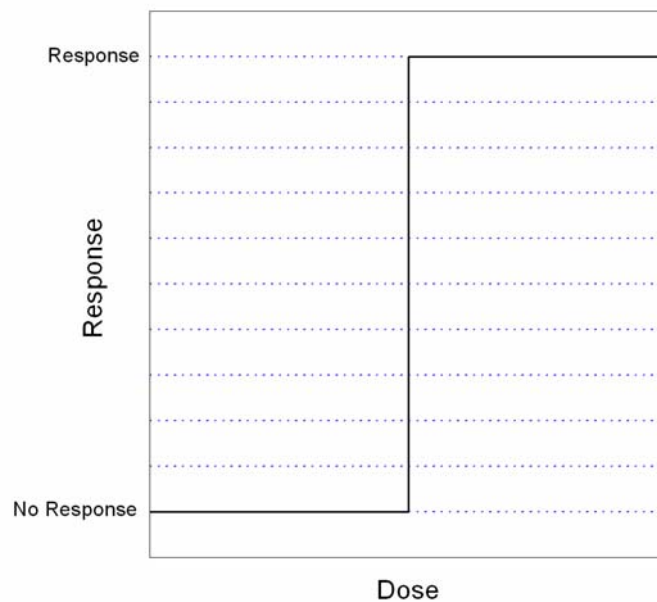


Figure 3.1: Theoretical dose-response curve. Above a certain critical dose, the object under investigation responds, while below show no response.

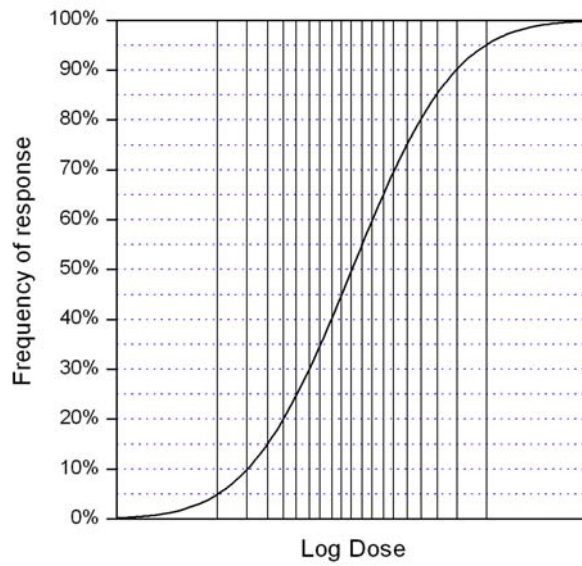


Figure 3.2: Relationship between dose and percentage of population response at a certain dose.

3.3 Log-Normal Distribution

Log-normal distribution is the distribution of a positive random variable “x” whose logarithm “y = ln(x)” is normally distributed. A Gaussian (normal) distribution describes random variation in data from many scientific fields. The normal distribution is arguably the most important probability distribution in probability. It is specified by two parameters: the arithmetic mean “μ”, and the standard deviation “σ”. The probability distribution function for normal distribution can be written as:

$$f(x) = \frac{1}{\sigma\sqrt{2\pi}} \exp\left[-\frac{1}{2}\left(\frac{x-\mu}{\sigma}\right)^2\right] \quad (3.1)$$

Such kinds of data sets are normally expressed as $\mu \pm \sigma$.

Irrespective of the mean “μ” and standard deviation “σ”, many normal distributions have skewness. Skewed distributions are mainly arises for non-negative, low mean values, and large variance. Both normal and log-normal variability acts independently based on a variety of forces. A major difference, however, is the additive and multiplicative effects associated with normal and log-normal distributions respectively [67]. For example, in laser safety, multiplicative dependence of thresholds on the

transmittance of different ocular tissues such as cornea, aqueous humar, lens, vitreous humar, the dimension of the tissue exposed, and the tissue absorption depth.

Log-normal distributions are usually characterized in term of log-transformed variable, with “ μ ” being the mean, and “ σ ” being the standard deviation of the normal distribution, i.e. $\log(x)$. This characterization can be advantageous as, by definition, log-normal distributions are symmetrical again at the log level. The probability density function of a log-normal distribution can be written as:

$$f(x) = \begin{cases} \frac{1}{\sigma x \sqrt{2\pi}} \exp\left[-\frac{1}{2}\left(\frac{\ln x - \mu}{\sigma}\right)^2\right] & \text{for } x > 0, \\ 0 & \text{for } x \leq 0. \end{cases} \quad (3.2)$$

And as a result the cumulative log-normal distribution function becomes:

$$F(x) = \frac{1}{\sigma \sqrt{2\pi}} \int_0^x \frac{1}{t} \exp\left[-\frac{1}{2}\left(\frac{\ln t - \mu}{\sigma}\right)^2\right] dt \quad (3.3)$$

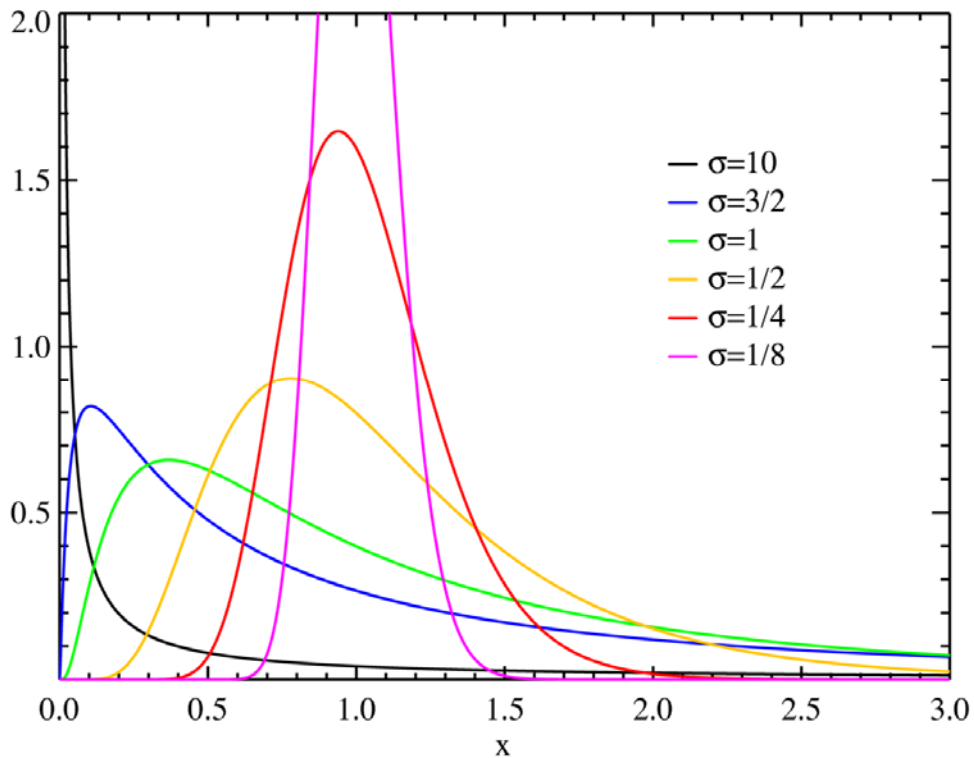


Figure 3.3: Probability density function for $\mu=0$ and varying values of σ . [GNU free documentation license]

Traditionally, for a log-normal distribution, the geometric mean is $\mu^* = e^\mu$ and the geometric standard deviation some time called multiplicative standard deviation is $\sigma^* = e^\sigma$. The multiplicative standard deviation parameter σ^* determines the shape of the distribution as can be seen figure 3.3, while the geometric mean μ^* is called the scale parameter. The geometric mean value changes accordingly with changing the X values but the value of σ^* remains same. Furthermore, as for normal distributed data, the interval $\mu \pm \sigma$ and $\mu \pm 2\sigma$ covers the probability or confidence level of 68.3%, and 95.5% respectively, in the same manner, interval $\mu^* \times / \sigma^*$ and $\mu^* \times / (\sigma^*)^2$ shows 68.3% and 95.5% confidence for a log-normal distributed data set [67].

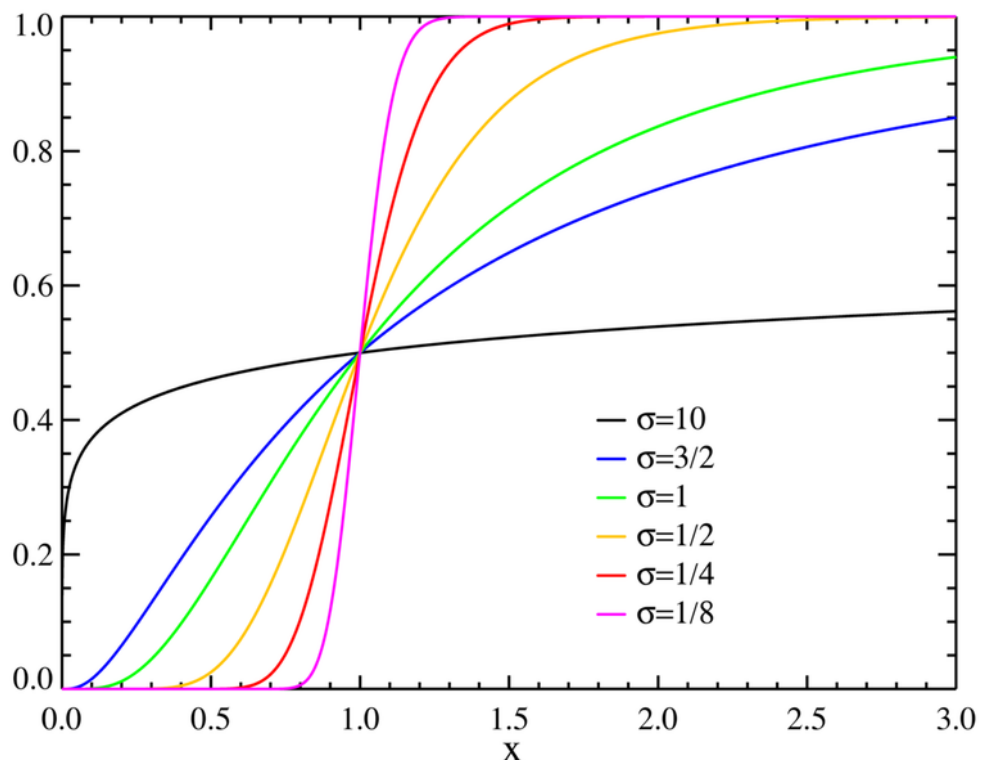


Figure 3.4: Cumulative distribution function for $\mu=0$ and varying values of σ . [GNU free documentation license]

Dose-response relations are essential for the understanding of effective dose 50% or ED50. Typically, such curves are sigmoid in nature and show cumulative action of the dose. This sigmoid curve is symmetrical if the abscissa (dose) of the frequency distribution is plotted on the log scale. For log-normal distribution curve the steepness also known as slope of the sigmoid curve equals to the multiplicative standard deviation σ^* , while the geometric mean μ^* equals to the ED50. Hence, the cumulative log-normal distribution can be re-written as:

$$P(OE) = \frac{1}{\ln(S)\sqrt{2\pi}} \int_0^{OE} \frac{1}{x} \exp\left[-\frac{1}{2}\left(\frac{\ln x - \ln(ED - 50)}{\ln(S)}\right)^2\right] dx = 0.5 + 0.5 \cdot \text{erf}\left(\frac{\ln(OE) - \ln(ED - 50)}{\sqrt{2} \cdot \ln(S)}\right)$$

(3.4)

Where, OE means ocular energy or exposure dose, erf represent error function. ED50 is the median dose, the dose which result 50% probability of injury (a detectable lesion), and which is frequently referred as *threshold* is considered the most important point on the plot. However, not only the ED50 but also the multiplicative standard deviation σ^* shall be taken into consideration for a better understanding of the dose-response curve of a population against a toxic agent. As stated earlier, the value of σ^* determines the steepness (slope) of the curve or in other words, the quality of the data set. Hence a poor quality experimental data set results in large value of σ and high quality data in lower value of σ as can be seen in figure 3.4. Additionally, ED16 as well as ED84 corresponds to the doses at which 16% and 84% of the exposures results in lesions. The slope of a cumulative distribution function can be written as:

$$S = \frac{ED84}{ED50} = \frac{ED50}{ED16} = e^\sigma \quad (3.5)$$

In laser safety community, this value of “S”, to a certain degree can also be seen not only as a measure for actual biological variability, but also for the quality of experimental results. For a step-like threshold or dose-response curve the value of “S” is equal to unity, i.e., $S = 1$, but typical values of S ranges between 1.0 and 2.0, and in some cases upto 2.8 [66].

3.4 Probit Analysis

In many fields of science, the inherent variability of the subject under investigation makes numerical studies more complicated, and conclusions must be based on the derived average values from number of observations. Today, with the advent of modern computers, statistical curve fitting might not be a problem. However, in the pre-computer era, curve fitting was tedious and time-consuming job. In recent years, probit analysis becomes a useful tool to analyse many kind of dose-response or binomial response experiments in a verity of fields, which simplify the fit of a cumulative log-

normal frequency distribution to the data. The ED50 can easily be calculated using probit analysis by transforming the cumulative log-normal frequency distribution into probit scale which yields a straight line graph for a logarithm of the dose values as can be seen in figure 3.5. The logarithm of the abscissa (dose) and the probit on the ordinate (response) are often referred to as “probit plots” [68].

The ratio of the response (lesion) to the total number of irradiated tissue samples gives the probability data at a particular dose. This probability data is subjected to probit transformation which is nothing but 5 more than the normal equivalent deviate. Replacing $z = \ln X$ in equation 3.2, with X being the dose, and integrating yields:

$$P(z) = \frac{1}{\sigma\sqrt{2\pi}} \int_{-\infty}^z \exp\left[-\frac{1}{2}\left(\frac{\ln x - \mu}{\sigma}\right)^2\right] dz \quad (3.6)$$

Where $P(z)$ represent the probability of response (lesion) for the logarithm of dose value.

Replacing the variable of the exponent in the above equation such that

$$u = \left(\frac{\ln x - \mu}{\sigma}\right) \quad (3.7)$$

The probability distribution becomes

$$P(z) = \frac{1}{\sqrt{2\pi}} \int_{-\infty}^{\frac{z-\mu}{\sigma}} \exp\left[-\frac{1}{2}u^2\right] du \quad (3.8)$$

The probit of the proportion P defined as the dose that corresponds to a probability P in normal distribution having mean value 5 and variance 1. In other words the cumulative distribution function becomes

$$P = \frac{1}{\sqrt{2\pi}} \int_{-\infty}^{Y-5} \exp\left[-\frac{1}{2}u^2\right] du \quad (3.9)$$

Comparing equation (3.8) and (3.9) gives

$$Y - 5 = \frac{1}{\sigma}(z - \mu). \quad (3.10)$$

Equation (3.10) shows a linear relation between probit Y corresponding to the set of responses and log-dose value i.e. z . Furthermore, a probit value of 5 corresponds to the

mean log-dose μ . Similarly, a unit increase or decrease in Y value means increasing or decreasing log-dose by σ .

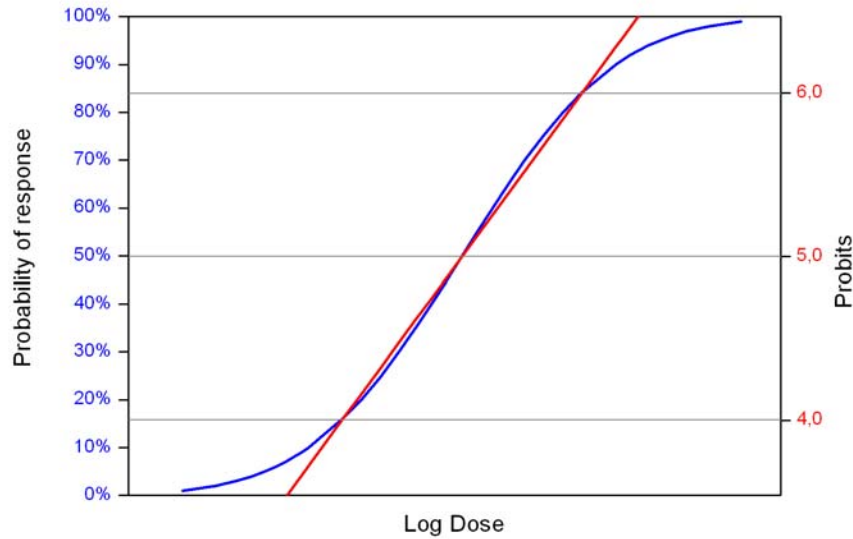


Figure 3.5: Effect of probit transformation: The sigmoid shape of the blue dose-response curve is transformed to a straight line (red).

3.5 Fiducial Limits

Fiducial limits specify the range of values for the ED50 that is supported by the statistical analysis of the data for a specific confidence level. The expected probit value for a given log-dose value x can be calculated by an equation described by the probitfit procedure i.e.

$$Y = \bar{y} + b(x - \bar{x}). \quad (3.11)$$

Such that \bar{y} and \bar{x} are the weighted averages of the probit value while x being the log-dose value and $b = \frac{1}{\sigma}$. Moreover, estimates $\text{Var}(\bar{y})$ and $\text{Var}(b)$ for the variance in the fit parameter \bar{y} and b are also provided by the probit fitting. The variance in the probit value can be determined using below equation:

$$\text{Var}(Y) = \text{Var}(\bar{y}) + (x - \bar{x})^2 \text{Var}(b). \quad (3.12)$$

Generally, the probit values are supposed to be normally distributed about its mean value Y such that its standard deviation is $\sigma = \sqrt{\text{Var}(Y)}$. One can say that, with a 68%

confidence level, the fiducial limits of the mean Y is give by $Y \pm \sqrt{Var(Y)}$. Similarly, the upper and lower fiducial limits for the mean Y can be written as:

$$Y_{UFL} = Y + t\sqrt{Var(Y)} \quad (3.13)$$

$$Y_{LFL} = Y - t\sqrt{Var(Y)} \quad (3.14)$$

Where ‘t’ is the normal deviate for the desired confidence level. The value of t is chosen such that the given equation become.

$$P(t) = \frac{1}{2\pi} \int_{-\infty}^t \exp\left[-\frac{1}{2}u^2\right] du = 0.5 + \frac{Confidence\ level}{2} \quad (3.15)$$

For example for the confidence level of 95% the value of t is $t = 1.96$ [68]. This means that the probability of finding the probit value $Y > Y_{UFL}$ or $Y < Y_{LFL}$ is 2.5% due to symmetry of the probability density function. Hence, 95% probability of the probit value is expected to lie between the upper and lower fiducial limits i.e. $Y_{LFL} < Y < Y_{UFL}$.

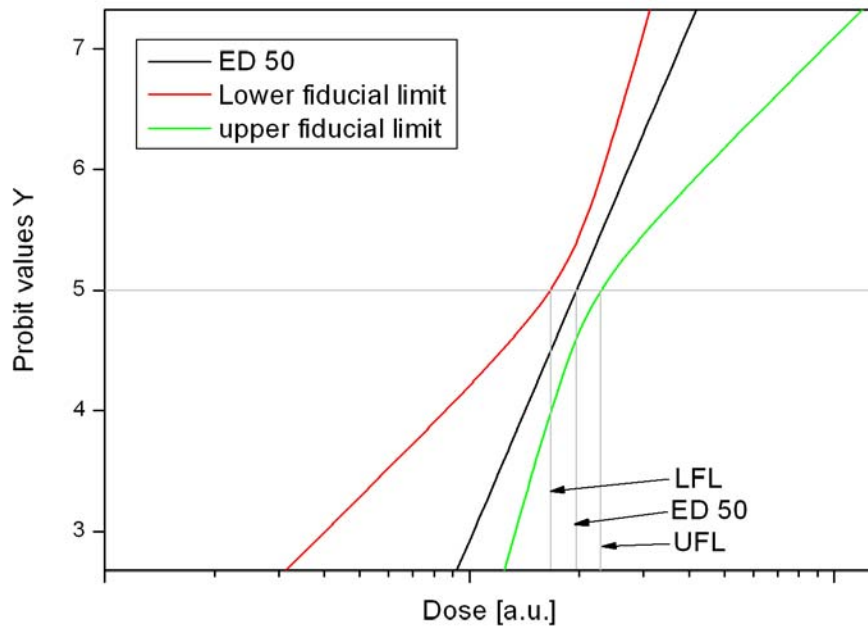


Figure 3.6: Example of probit curve, including the 95% confidence level fiducial curves. The horizontal gray line indicates the 50% probability of response level. The position at which this level intersects the probit curve and the two fiducial curves indicates the ED-50 and the lower and upper fiducial limits of the ED-50.

3.6 Corneal and Retinal Space

In the wavelength region of 400-1400 nm, instead of cornea, it is the retina of the eye which has the lowest injury threshold. For this reason, radiation in this particular wavelength band is known as retinal hazard region. The minimum possible spot size diameter achieved at the retina is approximately 25 μm [3]. Generally, angular subtense (plan angle which the spot or image at the retina makes as seen from the focusing element of the eye) are used instead of retinal spot diameter with the assumption that eye is filled with air. In laser standards this angle, having the symbol α , is measured in milliradian (mrad). The relation between the angular subtense α and the retinal spot size diameter d_r is given by:

$$d_r = \alpha \times f_e \quad (3.16)$$

Such that f_e is the effective focal length of the eye. The values of f_e for human and monkey are 17 mm and 13 mm respectively.

Retinal thermal MPE's are usually defined for worst case scenario i.e. minimal retinal spot produced by a well-collimated beam or point source. These MPE's are spot size dependent and varies relative to the minimal spot size by a correction factor (C_6 or C_E) that has a maximum value of 66.6. In the exposure limits guidelines, this correction factor is referred as C_6 in the IEC 60825-1 document or C_E in the ANSI and ICNIRP documents. For the minimal retinal spot size, retinal thermal MPE's have their lowest values and the correction factor equals to unity. The retinal thermal MPE's increases with the increase of the retinal spot size by a factor of $C_6 = \alpha/\alpha_{\min}$, such that the larger is the retinal spot, the more power is allowed to enter the eye.

Conventionally, in laser safety guidelines, MPE's are defined at the cornea, even for the retinal hazard region, because direct measurement of the irradiance or radiant exposure at the retina is not possible. In safety analysis, the irradiance or radiant exposure that incident on the cornea averaged over 7 mm aperture diameter has to be compared to the MPE. *Total Intraocular Energy* (TIE), the term frequently used in experimental studies, is obtained when the average radiant exposure at the cornea is multiply with the area of 7 mm aperture. Similarly, the MPE (J m^{-2}), when multiply with the area of 7 mm aperture, an energy (J) value is obtained which can be directly compare with TIE.

Furthermore, the transmittance of the ocular media in front of the retina is wavelength dependent. Hence, the radiant exposure (J m^{-2}) at the retina can be obtained by multiplying the TIE with the transmittance of the ocular media for that particular

wavelength and dividing with the retinal area over which this energy is distributed. The direct relation of the retinal spot size with the angular subtense given by Eq(3.16) means that the area of the retinal spot is directly proportional to α^2 , and retinal radiant exposure is proportional to TIE/α^2 . Using this concept, the spot size dependence (as a function of spot diameter or pulse duration) either in “retinal space” in terms of retinal radiant exposure ($J m^{-2}$), or in “corneal space” in terms of *Total Intraocular Energy* (J), can best be explained. Generally, in comparing different model and the human case, spot size is given in terms of diameter (μm) rather than angular subtense ‘ α ’ because the later depends on the effective focal length of the eye as given by eq(3.16) which is different for different species. For example, for the same angular subtense, the retinal spot size diameter on a monkey eye is smaller than on the human eye.

3.7 Dependence on Angular Subtense

The *minimum angular subtense* “ α_{min} ” is the smallest possible plane angle which the image on the retina make with the focusing element of the eye or the minimum possible spot size that produced by the focusing elements of the eye by focusing a very well-collimated beam on the retina. In laser safety standards, a value of 1.5 mrad has been assigned to α_{min} which in a human eye with 17 mm *effective focal length* is equivalent to a retinal spot diameter of 25.5 μm . Similarly, *maximum angular subtense* denoted by α_{max} currently has a numerical value of 100 mrad, i.e. $\alpha_{max} = 100$ mrad. This value is equivalent to a retinal spot diameter of 1.7 mm in the human eye. As discussed in the previous section, retinal thermal MPE varies relative to the angular subtense by a correction factor C_6 given by:

$$C_6 = \frac{\alpha}{\alpha_{min}} = \frac{\alpha}{1.5 mrad} \quad \alpha_{min} \leq \alpha \leq \alpha_{max} \quad (3.17)$$

Where α is the actual angular subtense. For apparent source, if the value of α is less than α_{min} , the value of α_{min} i.e. 1.5 mrad is assigned to α . Similarly, for sources with value of α larger than α_{max} , i.e. 100 mrad, the value of α_{max} will be assigned to α . However, the field of view (angle of acceptance), used for determining the radiant exposure and compared to the MPE value, must also be limited to 100 mrad. For open field of view and $\alpha > \alpha_{max}$, the condition for correction factor is different and has a symbol ‘ C_6^{open} ’ which is given as:

$$C_6^{open} = 66.6 \frac{\alpha^2}{\alpha_{max}^2} = \frac{\alpha_{max}}{\alpha_{min}} \frac{\alpha^2}{\alpha_{max}^2} = \frac{\alpha^2}{\alpha_{max} \alpha_{min}} \quad \alpha \geq \alpha_{max} \quad (3.18)$$

This formula reflects that when an open field of view is used for the determination of an exposure level, a value beyond 66.6 for C_6^{open} can be achieved with α^2 only. When the MPE is determined using the correction factor of C_6^{open} , the exposure assessment is not limited by an angle of acceptance. Hence, the total energy that passes through 7 mm aperture can be compared with the MPE.

Furthermore, as the *minimum angular subtense* α_{min} reflect the limitation of the focusing element of the eye, in retinal thermal space *maximum angular subtense* “ α_{max} ” indicates the knee or breakpoint between the two regions i.e., α^{-1} dependence where the MPE decreases with increase in retinal spot size and no α dependence where MPE remains constant as can be seen in figure 3.7. However, it has to be noted that use of the open field of view is only limited to top hat irradiance profile. For an irregular profile, where the local irradiances are different from each others, the angle of acceptance must be limited to a value equals to α_{max} , and α can be determined as given in IEC 60825-1.

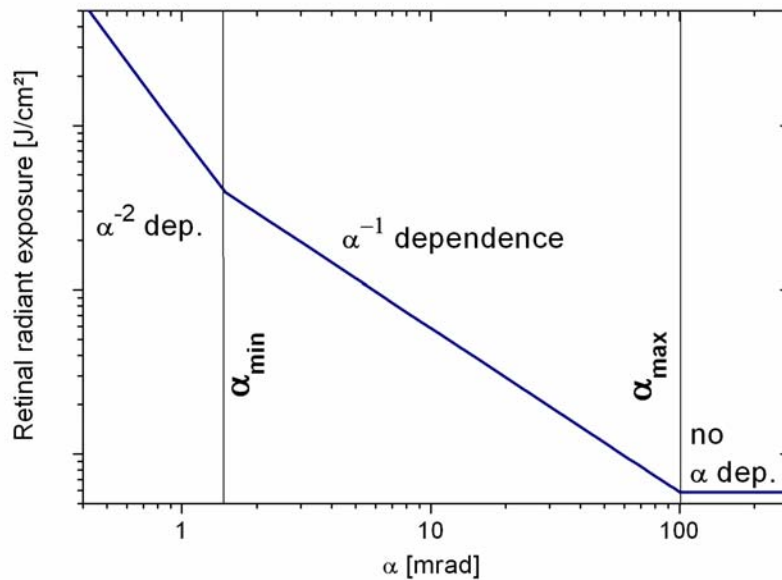


Figure 3.7: General dependence of the current MPE values, given in terms of retinal radiant exposure, as a function of angular subtense α , assuming an ocular transmittance of 1 [69].

3.8 Computer Model Used for Retinal Thermal Damage Thresholds

3.8.1 Overview

Apart from the experimental results which provide realistic retinal thermal thresholds, computational results based on theoretical model are also valuable. The difference between an experiment, with a real eye (*in-vivo* or *ex-vivo*), and a computer model is the amount of included complexity. Although, experiments on animals or animal tissues are carried out in a standardized and controlled environment, but certain factors e.g. laser beam temporal and spatial profile, pulse energy, scattering in the eye, damage and repair mechanisms, lesion detection etc complicate the problem. On the other hand, computational thermal model helps acquiring better understanding of the injury processes and hazard levels as it allows for the estimation of temperature elevation within the retina during and after the laser pulse. The computer model can also be used to characterize the risk for ocular injury independently of exposure limits and safety standards.

Schematic overview of the computer model, developed by Mathieu Jean at Seibersdorf Labor GmbH for thermal injury threshold calculations and used for this study, is shown in figure.3.8. This diagram represents the basic structure of the computer model along with inputs, outputs and physical sub-models. Each of the four sub-models, shown in figure.3.8, has a series of physical and computational parameters which are stated in [83]. This computer model is user friendly and upgradeable. This computer model on the whole consists of, a commercial software: *Comsol* (formerly *Femlab*) for the finite elements method, *Matlab* as a programming environment, and *Microsoft Excel* for the user's input/output processing. Figure 3.9 shows the flow chart diagram of the model indicating its sequential operations. Furthermore, with the help of this computer model several thousand of exposures can be computed automatically once the user input file (*Input.xls*), the only file to manage, is ready.

3.8.2 Optical Model

Pre-retinal ocular media filters out light almost entirely which lies outside the retinal hazard region i.e. 400-1400 nm. UV and IR-B/IR-C radiations are mostly absorbed by the lens or the cornea. In the retinal hazard region, absorption is dominated by pigments, various proteins and water molecules depending on the wavelength. Ocular transmission

measurements carried on Rhesus monkeys, form the most basic ocular model for the study of retinal exposure and which are used in this computer model [84].

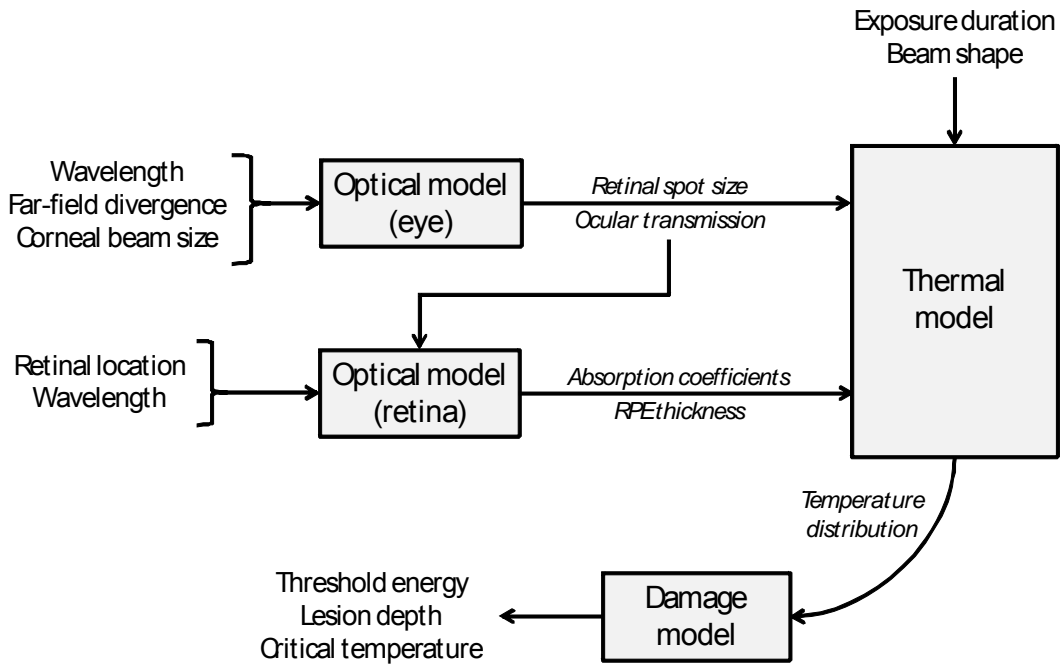


Figure 3.8: Block diagram of the computer model along with input, output and physical sub-models [83].

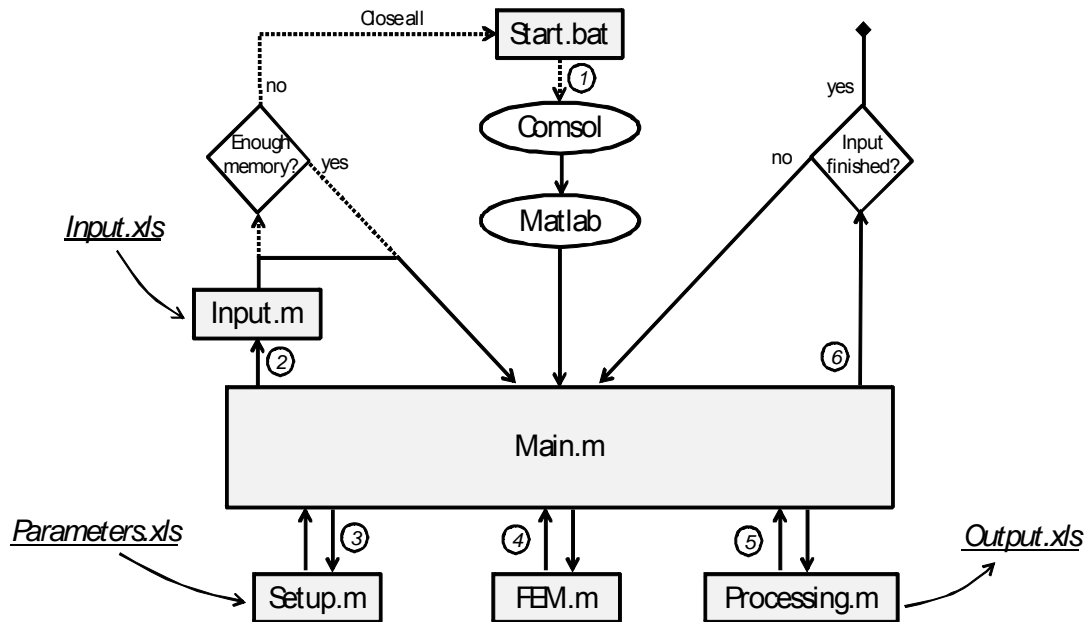


Figure 3.9: Flow chart diagram of the computer model representing different sequences by numbers, executions by straight arrows, and read/write operations by curved arrows [83].

Light for which pre-retinal ocular media is transparent passes through cornea, aqueous, lens, vitreous and finally reaches the retina. The retina is an assembly of complex layers. Regarding the computer model, used for thermal damage threshold calculations, three layers which play a significant role in terms of absorption, scattering and reflection are the retinal pigment epithelium (RPE), the choroid, and the sclera. The RPE and the choroid are highly pigmented and almost opaque in the visible wavelength band due to extremely high absorption co-efficient values. The main aim of the optical model is; (1) to determine the source term which is used in the heat equation, (2) absorption within the RPE and the Choroid axially and radially relatively to the total intra-ocular energy. These values are obtained from the combination of a transmission model, an ideal optical system, and a fundus reflectance model.

3.8.3 Thermal Model

When laser radiation is incident on biological tissue, part of the beam energy is reflected, scattered, transmitted, or absorbed. From the laser-tissue interaction mechanisms point of view, it is the fraction of absorbed energy within the tissue which is of interest. Once light energy is absorbed within the tissue, heat generation and conduction become relevant. The distribution of heat generated within the irradiated tissue due to absorption, considered as a source term over space and time, is described by the heat conduction equation. Heat conduction equation in cylindrical coordinate system can be written as:

$$\frac{\partial T(r, \theta, z, t)}{\partial t} - \alpha \cdot \Delta T(r, \theta, z, t) = q(r, \theta, z, t)$$

Where T is the increase in temperature, α is the thermal diffusivity and q is the time-dependent source term. The equation is linear provided that α does not depend on temperature. This approximation is convenient, since it simplifies tremendously the iterative process of the damage model. Solution of the heat conduction equation with proper initial boundary condition is possible both analytically and numerically. Today's powerful computational methods give support for the use of numerical solutions. Among numerical methods, the finite element method (FEM) is the more tempting. The availability of commercial software, stated above, is another convincing argument.

From the modelling point of view, used for laser-induced thermal retinal lesions, two relevant retinal layers (RPE and choroid) are considered flat, homogeneously absorbing and the surrounding medium is assumed to exhibit similar thermal properties. The heat source exhibit radial symmetry due to the symmetry of the laser beam and is supposed not to vary with depth. With these assumptions, model is reduced to a two-dimensional problem in cylindrical coordinates as shown in figure 3.10. Heat generation is expressed in power density.

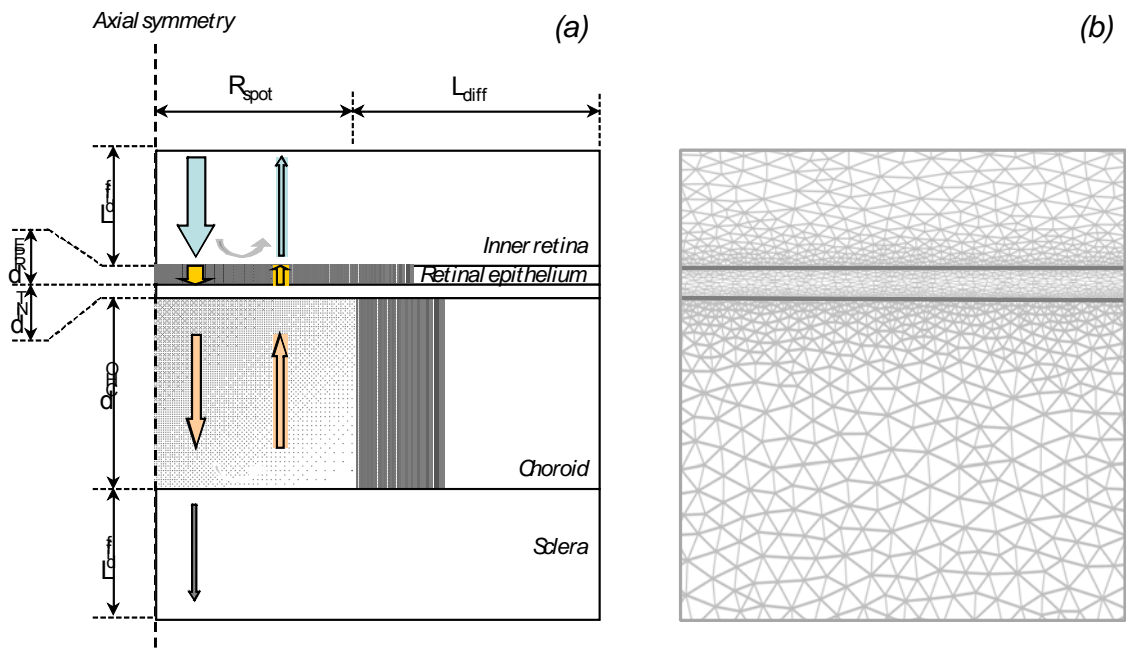


Figure 3.10: Structure of the thermal model showing dimensions, schematic light path, and the 3 layers planar mesh [83].

3.8.4 Damage Model

Retinal thermal damage can only be possible if the temperature of target tissue site raises, i.e., thermal damage cannot happen unless and until, the energy delivered to the tissue volume is faster than its leak away (dissipation) which will ultimately rises the tissue temperature leading to thermal damage. The criterion for thermal damage is expressed by a single parameter Ω , and can be calculated from the Arrhenius damage integral.

$$\Omega = \int_0^t k(T) dt$$

Such that damage is commonly set to $\Omega = 1$. The temperature dependent rate of damage is expressed as:

$$k(t) = A \cdot e^{\frac{-E}{RT(t)}}$$

Where $T(t)$ is the solution of the heat equation plus the initial temperature. A and E are the two constants, which can be related by deriving the Van't Hoff relation and observing a linear relationship between various thermal lesions [84], such that:

$$E = \frac{1}{0.003147} \cdot \left[\ln \left(\frac{A \cdot h}{k_B \cdot T_0} \right) + \frac{327.5}{R} \right]$$

This relation is believed to be the representative of the general form of thermal damage. Several investigators employed this model with success for various tissues, including the retina.

II. EXPERIMENTAL RESULTS AND DISCUSSIONS

4 Damage Threshold for the wavelength of 1090 nm

4.1 Background

It is firmly established that intense optical radiation, emitted from non-coherent as well as coherent sources and absorbed in the retina, can rise the retinal temperature high enough to cause damage. In the past three decades developments in laser technology particularly high power infrared (IR) lasers have evolved to play an important role in biology and medicine. Due to the transmission of the ocular media, near-infrared (NIR) radiation reaching the back of the eye may induce damage in the retina/choroid. The safe and effective use of laser requires the basic understanding of injury mechanisms that occur when laser light is incident upon biological tissue. The derivations of the human exposure limits for laser radiation mainly depend on the experimental ocular injury studies.

Majority of the threshold data on laser-induced retinal injury are obtained from experiments on laboratory animals (*in-vivo*) especially Rhesus monkey or animal tissues (*ex-vivo*), and only limited data from human volunteers or laser based accidents are also available. The purpose of this study is to determine laser-induced retinal thermal thresholds using single pulse duration of the NIR wavelength ($\lambda = 1090\text{nm}$). *Ex-vivo* explant bovine eye is used as experimental model. This report contains experimental threshold results, based on fluorescence microscopy, along with the computer model data, developed by this group, and validated by comparing with *in-vivo* NHP thermal injury threshold data.

4.2 Experimental Setup

Figure 4.1 depicts a schematic diagram of the optical setup used for irradiation of *ex-vivo* explant bovine retinal samples. A CW/Modulated high power Fibre laser by SPI Lasers (SP120C, Southampton, UK), emitting radiation in the NIR wavelength region with central emission wavelength $\lambda = 1090\text{ nm}$, has been used for irradiating the eye samples. The maximum output power of the laser was 120 Watts with high quality Gaussian beam. The reported beam quality factor (M^2) of this laser is 1.08 and beam circularity $\sim 98\%$ respectively. For the desired pulse durations, the laser was operated in the modulation mode by applying a TTL modulation signal to the external modulation trigger via BNC connector using a signal generator. The pulse duration widths were measured using digital storage oscilloscope (TDS6604B, Tektronix, Inc. USA).

According to the manufacturer advice, the laser was operated in the slow mode to suppress the initial spikes as can be seen in figure 4.2(A). The time lapse in each pulse was adjusted so as to get the desired pulse duration on the sample.

As radiation in the NIR wavelength region is less significantly absorbed by neutral density filters, used for attenuating laser power in the visible wavelength (532 nm) case, and because of the thermal lensing of filters follows from NIR-induced heating, which can distort the beam, glass wedges have been used to attenuate the output power of the laser. Two anti-reflecting (AR) coated 10° round wedge prisms (PS814-C, THORLABS, Inc. USA) with surfaces reflection less than 1% were placed at the distal end of the optical fibre to attenuate laser power.

A CCD camera (COHU, Model 7512, USA) was used for beam profile measurements in the sample plane. The camera has a pixel size of $7.6 \times 7.6 \mu\text{m}$ and an array size of 1292×1024 . The $1/e$ criterion of the peak value was applied for beam diameter definition in the beam analyser software (Spiricon, LBA-700PC, USA). For the desired spot size diameter at the sample plane a combination of biconvex lenses were used as can be seen in figure 4.1. To achieve small spot sizes e.g. $26 \mu\text{m}$ beam expander were introduced into the optical setup. A combination of mirrors was used to pass the beam on desired path. Figure 4.3 depicts the spot size diameter recorded with CCD camera.

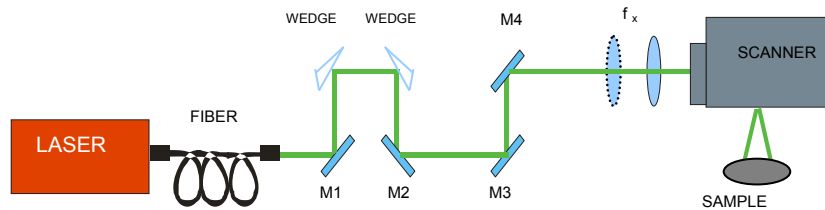


Figure 4.1: Graphical view of the experimental setup used for exposure of bovine retina samples.

The beam, after passing through the beam delivery system, the two power attenuating wedges, and a combination of lenses, was finally directed to a galvanometer-driven scan head (SCANLAB, hurrySCAN™ 14, Germany), placed between the optical system and the sample, in order to achieve the desired exposure pattern on the sample. The scanner was controlled by a PC interface card (SCANLAB, RTC® 4, Germany) with the help of a self developed computer program by Thomas Auzinger, *Scanner Control 1.08*. This automatic program was used for controlling the pulse duration, the scanner mirror position, and the laser output power between marked power level and idle power level.

This computer program makes it possible to expose a sample with a grid of individual laser exposures in short period of time and with high precision.

Before sample irradiation, the energy deposited on each irradiated location was carefully measured beneath the scanner at or near the sample position using pulse duration and power output in Microsoft excel. For this purpose a calibrated laser power meter [Ophir 3A and Ophir L40(150)A, North Logan, Utah] was used to record the power incident on the sample for each exposure duration. These measurements were used for interpolation whose analytical expression was used to calculate the deposited energy for each laser power level.

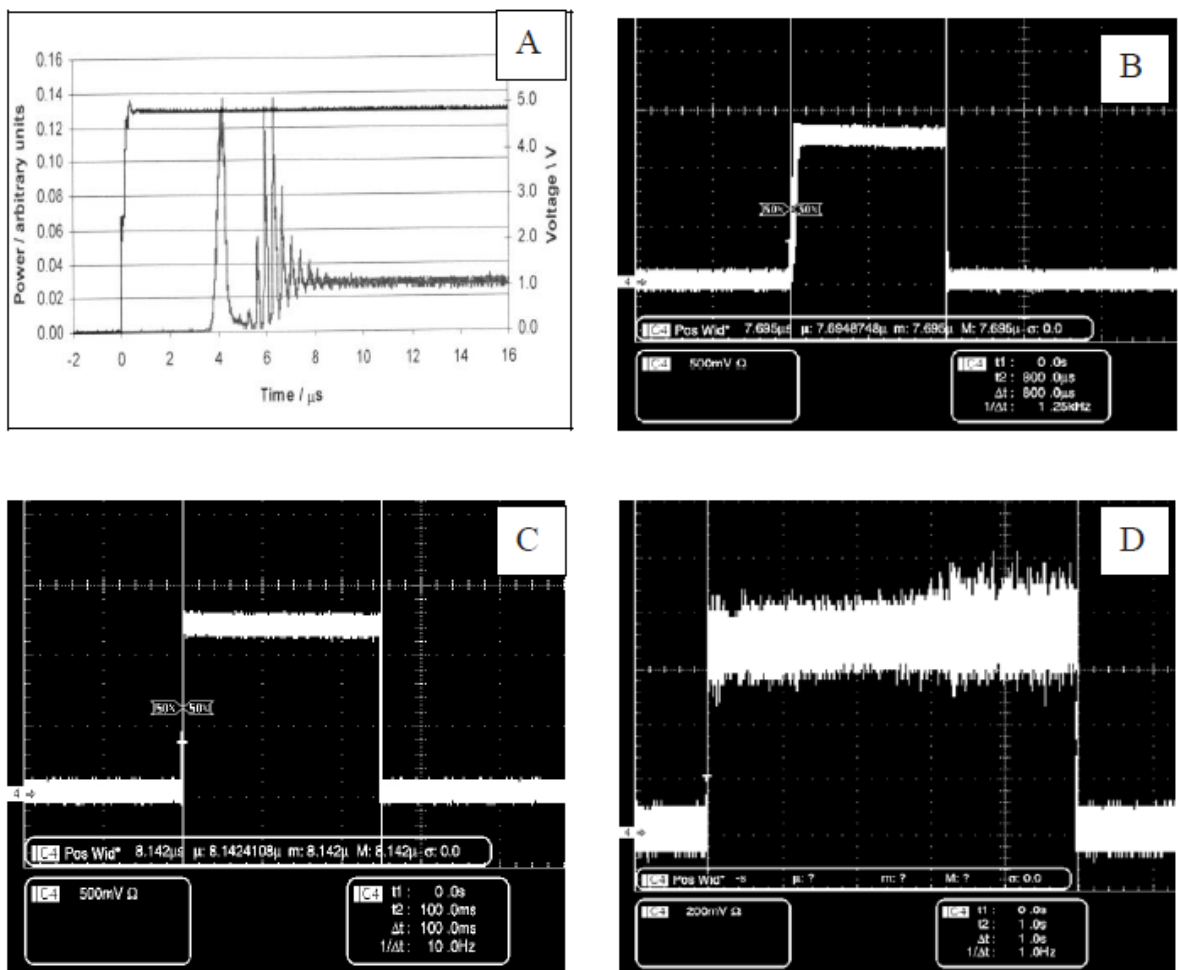


Figure 4.2: Modulated high power fiber laser pulse widths when used in both fast (A) and slow mode.

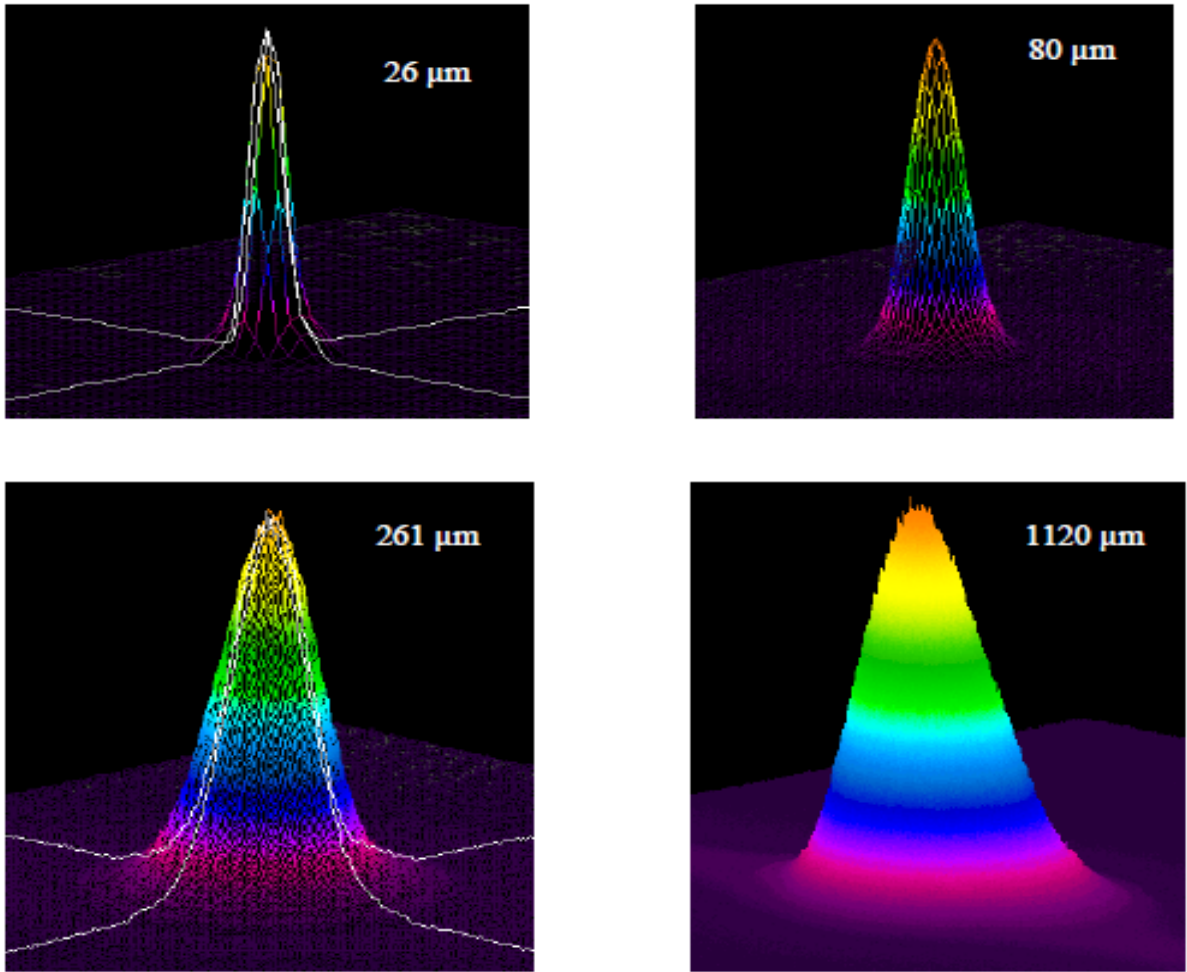


Figure 4.3: 3-dimensional representation of 4 different beam profiles achieved with different combination of lenses for the 1090 nm.

4.3 Sample Preparation and Exposure

4.3.1 Chondroitinase ABC Assay

Fresh *in-vitro* cow eyes were collected under informed consent from slaughterhouses in Zemendorf, Pischelsdorf and Berndorf (Austria). These eyes were extracted immediately after slaughter, kept in a cool environment, in order to prohibit cell death, and were quickly transported to the toxicology laboratory in Seibersdorf. In general, the eyes used for experiments were taken from cows, age between 12 and 36 months. After dissection of the surrounding connective tissues, the eye was opened near the lens position and the vitreous body was removed manually. The black-pigmented part of the fundus of the eye was cut into rectangular pieces of about $2 \times 2 \text{ cm}^2$ in size and placed in phosphate buffered saline (PBS) which helps in maintaining a constant P_H of the cell

biology and nourishes the RPE cells from dissection until examination as shown in figure 4.4. After the completion of dissection process, all samples were placed in the enzyme *Chondroitinase ABC* (Sigma-Aldrich, USA) for 15-30 minutes. *Chondroitinase ABC* (Chondroitin sulphate + H₂O) cleaves the outer segments of the photoreceptors, rods and cones, from the apical surface of the RPE. At the completion of incubation time in the enzyme, the sensory retina was gently removed from each sample, so that the upper most layer was the retinal pigment epithelium (RPE) with supportive connecting tissues of choroid and sclera. The influence of the application of *Chondroitinase ABC* on the damage threshold was already evaluated and concluded without having any adverse effect, except an improvement in the optical appearance of the RPE cells. Per eye, usually three to four samples were taken and were labeled in order to be able to trace back the samples after exposure.



Figure 4.4: Sample preparation for irradiation.

4.3.2 Live/Dead Assay

After the removal of sensory retina, all samples were stained with a cell viability marker CalceinAM. This Aceto-Methoxy derivate of Calcein (CalceinAM) is a non-fluorescent, hydrophobic compound that can easily permeates through the cellular membrane in live cells. The hydrolysis of CalceinAM by intracellular esterases produces Calcein, a

hydrophilic, strongly fluorescent compound that is well-retained in the cell cytoplasm, making it a useful assay for cell viability testing. Figure 4.5 shows the transformation along with chemical composition of CalceinAM into Calcein. Calcein by itself is a fluorescent derivative with peak absorption at 490 nm and maximum fluorescence at 520 nm [70]. The incubation time for the sample was mostly between 15 and 30 minutes. After incubation period in the dye, all the samples were then fixed into the sample holders with circular cuts in the center, exposing the superficial RPE layer. The sample holders were then kept into a Petri dish filled with about 2.5 mm thick layer of phosphate buffered saline (PBS) covering the RPE cells as shown in figure 4.6.

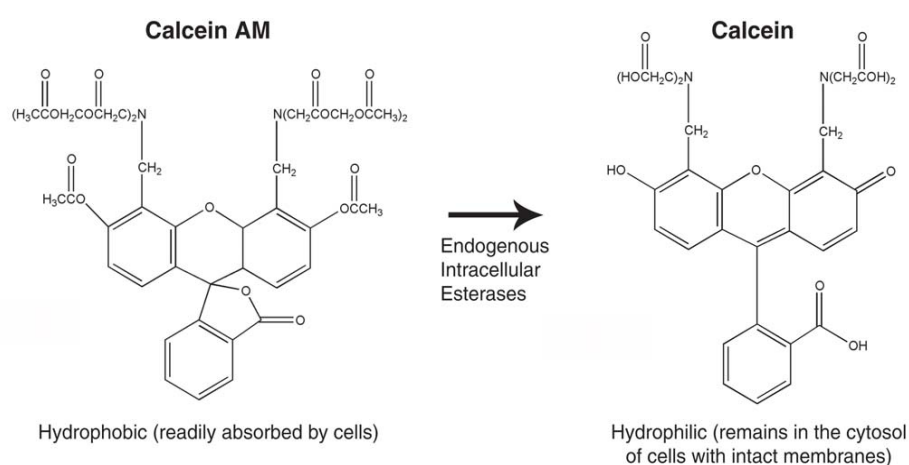


Figure 4.5: Chemical structure of CalceinAM and Calcein [70].

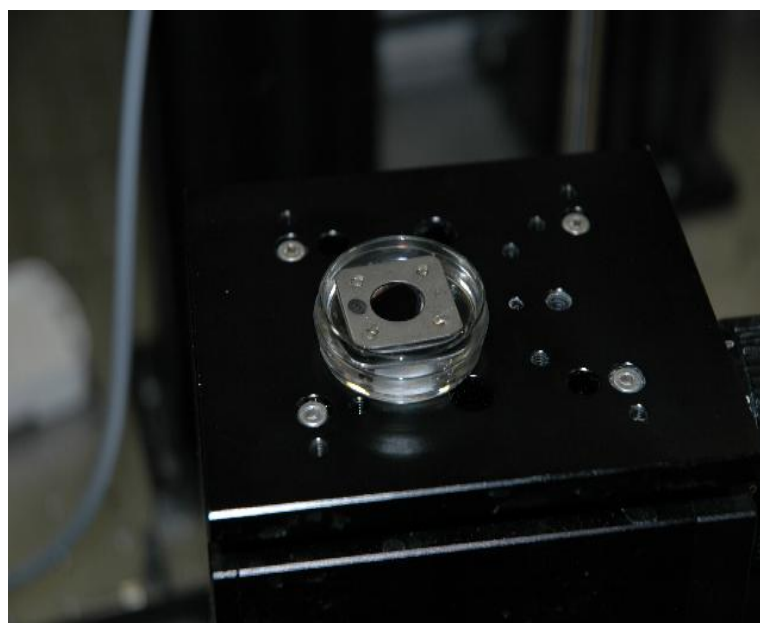


Figure 4.6: A retinal sample mounted in a sample holder and placed in a Petri dish, ready for exposure.

After the completion of sample preparation process but before exposure to laser radiation, cell viability tests were performed by examining all samples in the Zeiss inverted fluorescence microscope. The purpose of this exercise was to select only good quality samples and discard all those samples which were damaged already due to mishandling in the preparation process or environmental conditions. Those good quality samples were then exposed to the laser radiation and were used for data analysis.

4.3.3 Exposure

Thermally induced damage depends exponentially on temperature, as is also shown by the Arrhenius damage criteria, mostly used for thermal damage calculations. Therefore, irradiation of the tissue samples had been performed with sample background temperature at or near to the room temperature i.e. $\sim 20^{\circ}\text{C}$. Similarly, the computer model, described in section 3.8, used for thermal damage threshold calculations (developed by Bernhard Seiser and Mathieu Jean) [82,83], assumed a medium overlying the retinal pigment epithelium with the physical properties of water. Therefore, the level of phosphate buffered saline (PBS) or Hank solution, nourishing the RPE cells from the time of dissection till examination, in the Petri dish was raised about 2.5 mm above the RPE surface. This Hank solution has neither distorting influences on beam propagation nor on the beam diameter in the focus, except shifting the beam focus to a position slightly behind its position in air. A dislocation of the focus of less than 0.355 mm was calculated with computer program WinABCD, developed by Dr Bernd Eppich, using the respective laser beam parameters for 26 μm spot and compensated in positioning the sample.

The scanner control, used for a defined exposure pattern, was calibrated with the horizontal position of the sample. The sample holder dimensions were stored in the scanner control and were calibrated with the sample. The scanner control mirrors were adjusted such that the laser beam draws a rectangular outline. This rectangular outline was scaled down until the area on the sample was enclosed. Infrared sensor card was used for locating the beam within the optical system and at the sample position for calibration purposes.

Each series of exposure was first planned in *Microsoft Excel* and was finally executed with control scanner. For each exposure series, the upper and lower limits of the output power values, the total number of exposures, pulse duration, number of series, number of exposures on each site etc were set in the Excel sheet. These data were than

transferred to the scanner control, where the scanner control automatically calculate the coordinates of the exposure grid based on the dimensions of the rectangular outline above the sample, the spacing between the two exposure points, the scanner control mirror movements, and power command values.

For each sample, an exposure pattern was chosen such that the energy per pulse was increasing from site to site in a regular manner. Because of the inherent complexity and variability of the biological tissues, a large energy range was selected for each sample to cover the no-damage and damage regions which is essential for threshold measurements. Because of this large energy range, the energy step or gap between two consecutive exposure sites was also large, which somehow increases the uncertainty. To get rid of such large energy steps and minimize the uncertainty, exposures were executed on a test sample before starting the regular experiment, in order to locate the approximate threshold level for each exposure pattern.

4.4 Data Analysis

With the completion of exposure to laser radiation, all *ex-vivo* explant bovine retinal samples were examined with the Carl Zeiss Axiovert inverted microscope. As stated earlier, each sample was labeled in order to trace back essential information e.g. temperature of the sample, time of exposure, time of examination etc. For each sample, the delay, time between exposure and time of examination, was mostly around 30 minutes. Upon examination it was noted that living cells were still emitting bright green fluorescence as it was before exposures, except the damaged cells which appeared dark due to leakage of the dye from cell membrane as can be seen in figure 4.7. Additionally, a marking grid was introduced on each sample consisting of an intersecting horizontal and vertical line such that each point on the grid was exposed with suprathreshold power.

Under the microscope each exposure site on the sample was graded as “no damage” or “damage” and was labeled “0” or “1” on the excel sheet respectively. No damaged sites were those cells which survived under intense light and were not affected by exposure, while damaged sites composed of those cells for which the exposure was above their threshold level. For almost each sample, a third interesting phenomenon i.e. very bright fluorescence in between the no damaged and damaged sites were also seen. These three patterns can be easily seen on irradiated bovine retina sample shown in figure 4.7.

In most cases, it was noted that the bright fluorescence droplets were formed just before the clearly dark damaged cells i.e. very near to the threshold region. Since, it was difficult to see the damage or no damage condition of the cells beneath the bright fluorescence droplets, and because of the different appearance of those brighter cells compared to their surrounding normal cells, those highly bright spots were also graded as damaged sites, although the exact reason for this was not know. Moreover, the number of those bright fluorescent were more for small spots diameter as well as pulse durations.

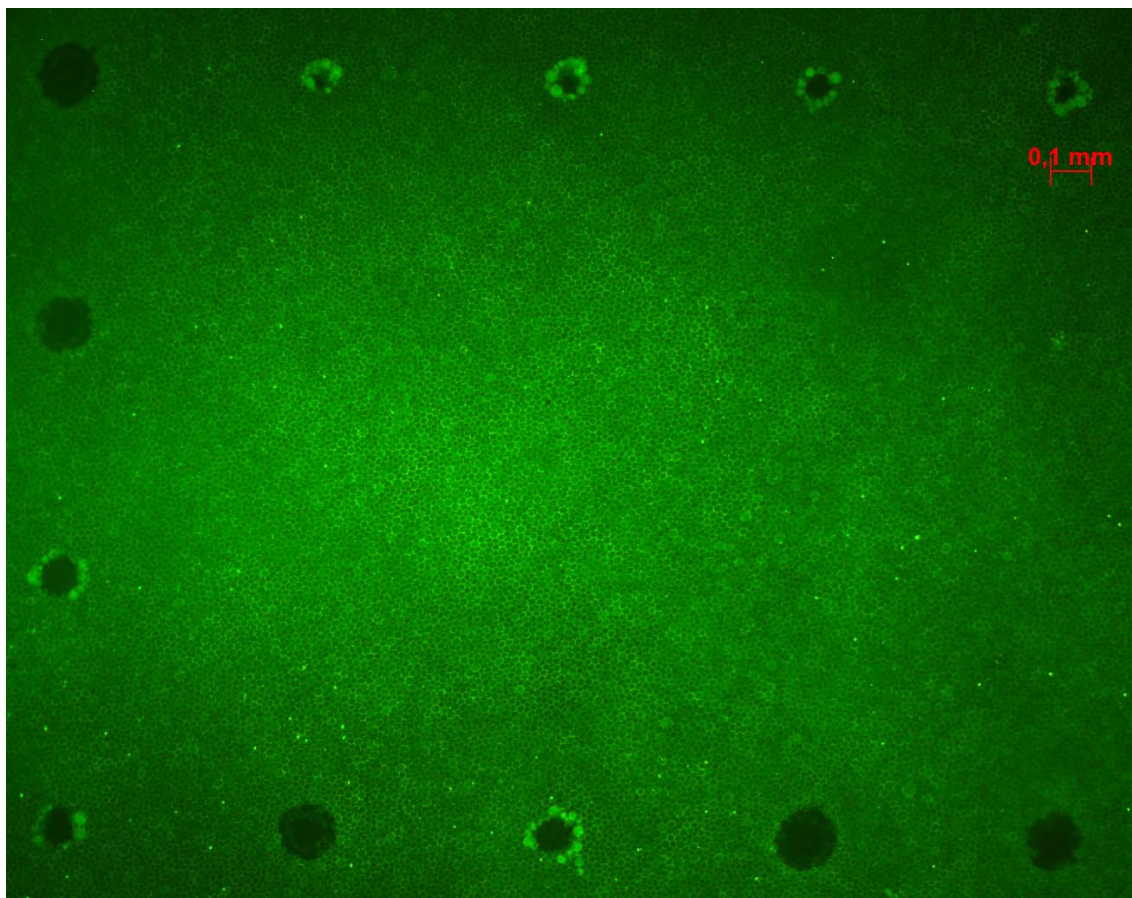


Figure 4.7: An exposed RPE sample. The left most column and the bottom row are the two intersecting lines of the super threshold grid points (“marker lesions”). The middle rows show no damage to laser, while the top row, four exposure sites, shows damage. The brighter site between clearly damaged and no damaged region can also be seen and such brighter sites were also graded as damaged.

Upon analyzing each exposure site of each sample under the microscope and labelling them “0” or “1” for no damage and damage site respectively in the *Microsoft excel*

sheet, this corresponding data was stored against each energy value for each sample in the computer where a data sheet was prepared for each sample. The data from all the samples, for each exposure pattern i.e. spot size diameter, pulse duration etc, were combined and transferred to the Probit analysis software *ProbitFit* (Brian Lund, Northrop Grumman, USA) to obtain ED50 and slope values. Similarly, the corresponding ED50 for each sample was also calculated by transferring their lesion no lesion data to the Probit software. The slope of the line was defined as the ratio of the doses corresponding to ED84 (dose corresponds to 84 % in lesion) and ED50 (dose corresponds to 50 % in lesion).

4.5 Uncertainty and Variability Factors

Generally, the exact value of any measured quantity is always uncertain. Uncertainty is therefore an inherent factor of the measurement process. Uncertainty is a measure of the reliability or quality of the measured data. Uncertainties may be *systematic*, which arises due to faults in the measuring devices or in the techniques used in the experiment or *random* i.e. unpredictable variations in the experimental conditions.

As previously discussed, two power meters, 3A (S/N: 151972) upto a maximum power of 3 Watts and L40 (150)A (S/N: 143157) for high power values, were used to measure power/energy in the sample plane. The test reports provided by the manufacturer claim for the accuracy of the detectors 3A and L40 to $\pm 1.5\%$ and $\pm 1\%$ respectively. Furthermore, because intra- and inter- individual response to exposure is variable, therefore, the inherent biological variability of the tissue under investigation also plays an important role in altering the real value of the measurement process.

Similarly, measurement of the spot size diameter in the sample plan was also critical and hence enhances the uncertainty. The radius $W(z)$ of the propagating laser beam at any position “ z ” can be calculated from the complex wave equation given as:

$$W(z) = W_0 \left[1 + \left(\frac{z - z_0}{z_R} \right)^2 \right]^{\frac{1}{2}} \quad (4.1)$$

With

$$z_R = \frac{\pi W_0^2}{M^2 \lambda} \quad (4.2)$$

In the above equations, $2W_0$ is called beam waist diameter (the minimum beam diameter) which is located at z_0 along the propagation axis, and z_R called the Rayleigh range is the distance from z_0 , where the beam diameter increases by a factor of $\sqrt{2}$. Equation 4.2 shows that the Rayleigh range increases with increasing beam waist diameter, and hence, the bigger the Rayleigh range, the less critical is a slight mispositioning of the sample. Furthermore, due to inverse relationship between the Rayleigh range and the beam divergence, mispositioning of the sample plane was only critical for small beam diameters.

Variations in the surface height of the samples as well as the curvature were also critical factors, especially in small spot size diameter cases because of the small Rayleigh range. To overcome this problem the grid dimension or the irradiated area on the sample was reduced to a maximum of $2 \times 2 \text{ mm}^2$, and the samples were irradiated at least at three different locations by varying the height of the samples to $\pm 0.5 \text{ mm}$. Among these series, the one with the greatest number of lesions being the closest to the beam waist were selected for damage threshold calculations.

Moreover, as described earlier, a CCD camera along with software *LBA-PC* (Spiricon, USA) was used for the spot size diameter calculation in the sample plane. It measures the lengths of two orthogonal lines which pass through the beam centroid and counts for all the pixels whose pixel value was greater than the pixel value corresponding to $1/e$ of the peak value. The reported diameter is the product of the number of pixels having values greater than $1/e$ clip level and pixel pitch. One pixel of the CCD camera had the dimensions of $6.7 \mu\text{m} \times 6.7 \mu\text{m}$. Therefore, increasing the number of pixels in horizontal or in vertical direction by one, an increase of 11.4% for a spot with diameter of $26 \mu\text{m}$, 4% for a $80 \mu\text{m}$ spot, and 1.3% for a $261 \mu\text{m}$ spot could be observed. Although, the resolution $6.7 \mu\text{m} \times 6.7 \mu\text{m}$ of the CCD camera limits the minimum effective diameter calculations to approximately $47 \mu\text{m}$, but the camera-software can calculate beam diameter having value less than $47 \mu\text{m}$. Therefore, very careful attitude towards small spot diameters were required and given, particularly in calculating beam diameter e.g. $26 \mu\text{m}$.

Another important factor of uncertainty affecting the measured data was the horizontal smoothness of the Hank solution surface. Since the Petri dish containing the sample was filled with hank about 2.5 mm above the sample surface. Therefore, the horizontal smoothness of the hank surface was much important, because the curve surface of the

hank solution could acts like a lens, and could alter the beam properties. To avoid any changes in the beam properties, two steps had been taken, first, the horizontal surface was maintained as smooth as possible, and second, the exposed area on the sample was kept as minimum as possible. With a smooth horizontal surface the beam properties remain unaltered, except, a shift in the beam focus on the optical axis to a position slightly behind its original position due to hank solution. Using *Beam Analyser* software *WinABCD* developed by Dr. Bernd Eppich, a dislocation of around 0.4 mm was calculated for 26 μm spot size diameter and accounted for in the positioning procedure of the sample. Again, this correction of the dislocation was much critical for small spot size compare to large spots due to small Rayleigh range value for small spots diameters.

4.6 Results

4.6.1 *Ex-vivo* Bovine and Computer Model

Ex-vivo explant bovine retinal thermal damage threshold (ED50) results calculated by the probit analysis based on lesion/no-lesion data are summarized in table A.1. These results are obtained for a varying pulse durations ranging from 1 ms to 1 s, and for a spot size diameter from 26 μm to 2539 μm . The slope “S” of the probit line (ED84/ED50) for these data points are in a range of 1.09 and 1.28, except for a very large spot size for which a very sharp threshold value, i.e. slope value 1.01, was computed by the probit analysis software which results in fiducial limits equal to the ED50. Variations in the slope values may be assigned to variability in the biological samples e.g. age, gender, location in the eye etc, or, it may also be assigned to uncertainty e.g. experimental fault, environmental conditions etc. Furthermore, in the case of a very large spot i.e. 2539 μm at 1 s, only four exposures could be manage and executed on each sample, because of the limitation of the sample dimension within the sample holder.

Since the reported laser beam profile was TEM₀₀, hence, all exposures were performed with a Gaussian beam profile. For a combination of four pulse durations and five different spot size diameters, a total of 3453 exposures have been executed on 184 samples. These numbers indicates how tedious, if not impossible, it could have been for the *in-vivo* experimentalist/experimentalists to obtain such an enormous threshold data that explain, for the first time in this specific wavelength band, the spot size as well as the pulse duration dependencies.

Ex-vivo explant bovine thermal damage thresholds plotted in terms of radiant exposure as a function of spot size diameter, for different pulse durations, are shown in figure 4.8. Threshold results calculated with the computer model based on the *Arrhenius* damage criterion are also shown in this figure (the calculations were performed by Mathieu Jean at Seibersdorf Labor GmbH). The experimental threshold results are in close accord with the computer simulation data except for small spot and short pulse duration, where experimental threshold data is lower by factor of 1.4. This could be either due to experimental uncertainty described in previous section or could be the limitations of the damage model.

The dependence of damage threshold on the angular subtense “ α ” or spot size diameter, as stated in section 3.7, can be seen in figure 4.8. At least two regions are clearly seen in this figure; region I, where the damage threshold, in terms of radiant exposure, is inversely related to spot size diameter ($1/D$ relation) or spot size dependence, and region II, where damage threshold is independent of the spot size diameter or no spot size dependence. For any value of pulse duration, the two regions i.e. spot size dependence region and no spot size dependence region are roughly separated by an inflexion point or knee. Furthermore, the position of the inflexion point is pulse duration dependent i.e. increases with increasing pulse duration, or another words, the longer the pulse duration, the larger is the corresponding spot size diameter where inflection occurs.

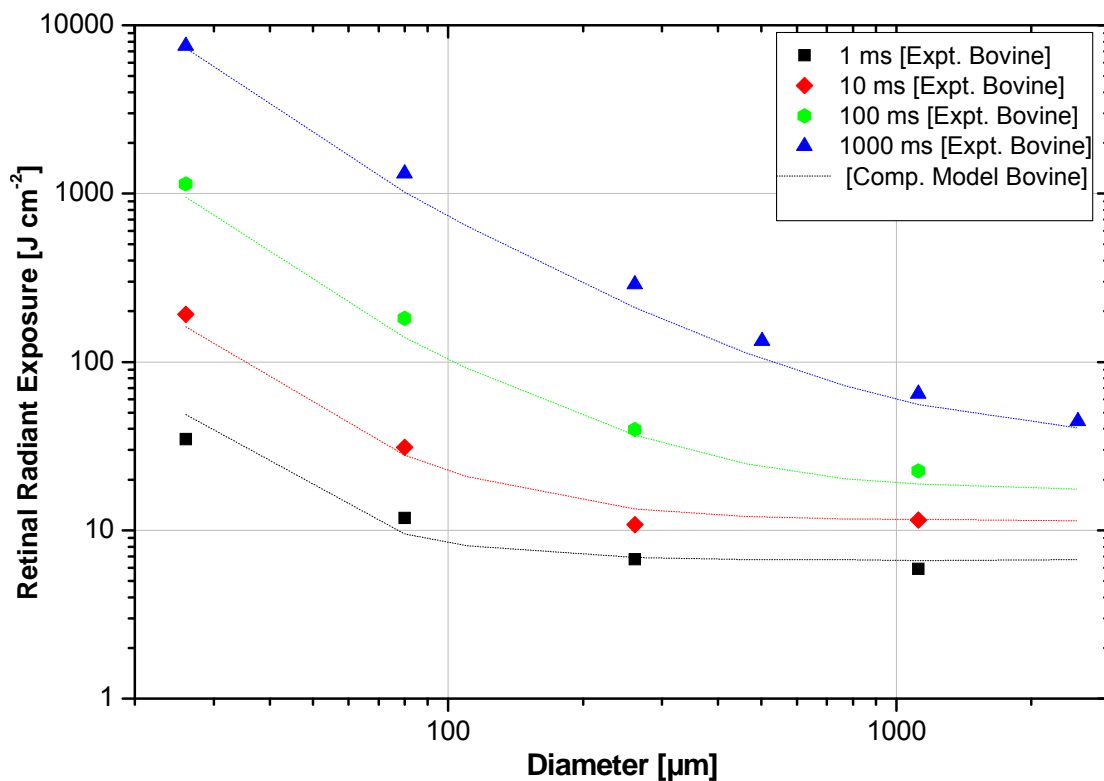


Figure 4.8: Single pulse retinal damage thresholds in terms of retinal radiant exposure as a function of spot size diameter of the *ex-vivo* bovine eyes. Different symbols represent experimental data for Gaussian beam profile, while dotted line is the computer simulation data for the same beam profile.

Similarly, for any value of spot size diameter shown in figure 4.8, the vertical line for each corresponding spot size diameter represents the pulse duration dependence. Variations in damage threshold with pulse duration for different spot sizes can be easily seen in this figure. The gap between damage thresholds for small spot size diameter e.g. 26 μm is more strongly noticeable than for large spot size diameter e.g. 1120 μm . This effect is comparatively better shown in figure 4.9, the pulse duration dependence, where damage thresholds in terms of radiant exposures are plotted as a function of pulse durations.

In figure 4.9, damage thresholds for all spot sizes at large pulse duration e.g. 1 s are well separated and follow a trend, such that they converge at pulse duration less than 1 ms except for 26 μm spot size. Further investigation of the threshold results show that large spots e.g. 261 μm and 1120 μm converges at pulse duration around 10 ms, whereas,

small spots like 80 μm and 26 μm are still separated. Computer model calculations as well as extrapolation of the experimental threshold results predict that, 80 μm spot size will merge/join the two large spots trend at pulse duration $\sim 100 \mu\text{s}$. Additionally, among all separated curves, the small spot size i.e. 26 μm shows the largest pulse duration dependence with a slope $t^{0.80}$, while the large spot size i.e. 1120 μm smallest dependence with a slope $t^{0.35}$.

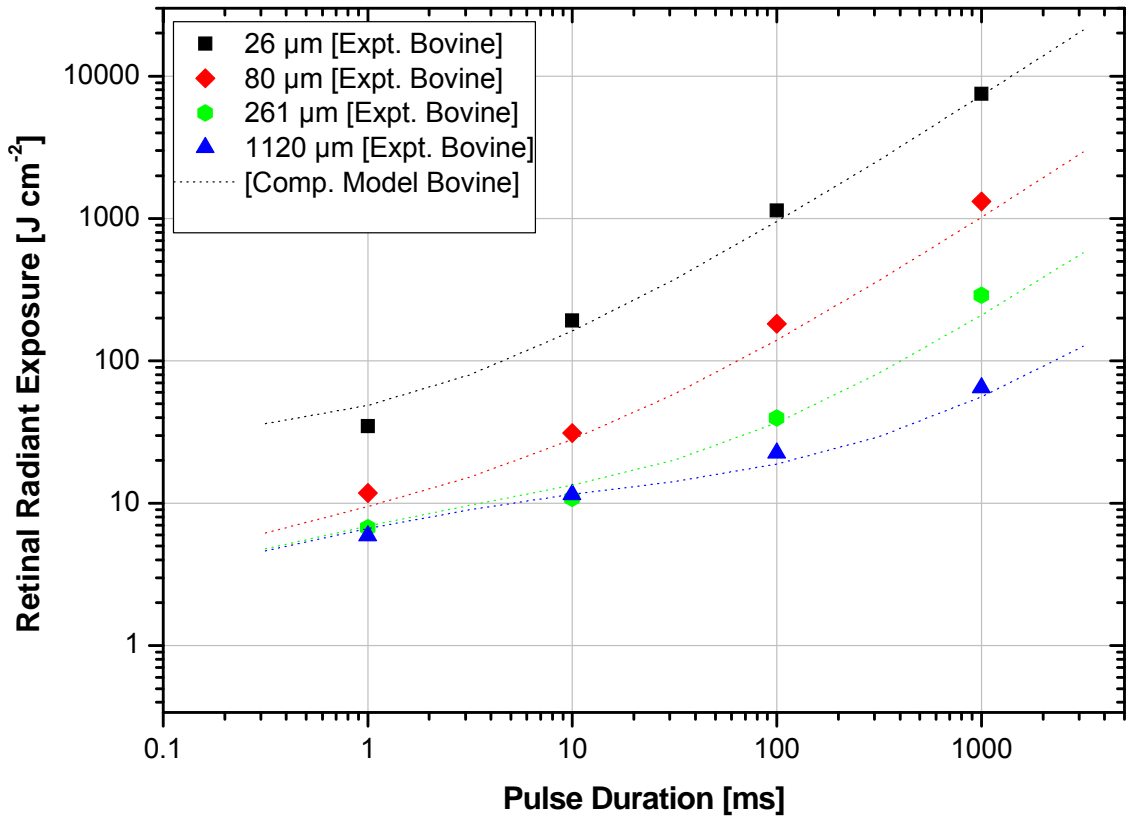


Figure 4.9: Single pulse retinal damage thresholds in terms of radiant exposure as a function of pulse duration of *ex-vivo* explant bovine eyes. Different symbols represent experimental data for Gaussian beam profile, while dotted line is the computer simulation data for the same beam profile.

4.6.2 Comparison with Non-Human Primate (NHP) Threshold Data

Because of the similarities of the ocular media with that of the human, non-human primate (NHP), particularly one special genus Rhesus monkey, has been used extensively in *in-vivo* experiments for obtaining retinal thermal damage thresholds. No single *in-vivo* NHP damage threshold study has been found which uses a set of parameters showing the complete spot size dependence. For comparison with *ex-vivo*

bovine retinal thresholds, *in-vivo* NHP retinal thermal threshold data, for similar laser parameters, available in the literature, is collected and presented in table A.2. The two model thresholds i.e. *in-vivo* NHP and *ex-vivo* bovine (this study) are plotted in terms of *Total Intraocular Energy* (TIE) as a function of spot size diameter and shown in Figure 4.10. One must note however that, *in-vivo* NHP retinal damage threshold results represent dose/energy per pulse delivered at the cornea, whereas, *ex-vivo* explant bovine thresholds are determined from dose/energy directly delivered at the retina (RPE). Therefore, for direct comparison between the two model threshold results at the cornea, *ex-vivo* bovine threshold results are corrected for 62 % transmission of the pre-retinal ocular media [24,44].

It must be noted, however, that the minimum retinal spot diameter for *in-vivo* NHP are theoretical values, considering rhesus monkey eye as perfect optical system. Studies have shown that, actual retinal beam diameter for NIR are wavelength dependent, and increases with increasing wavelength due to intraocular scattering, chromatic aberration, and lower melanin absorption in the RPE [71]. A more recent study in the visible wavelength range has shown that, *in-vivo* NHP threshold value (ED50) does not decrease with irradiated area for retinal diameter less than 70-100 μm [72].

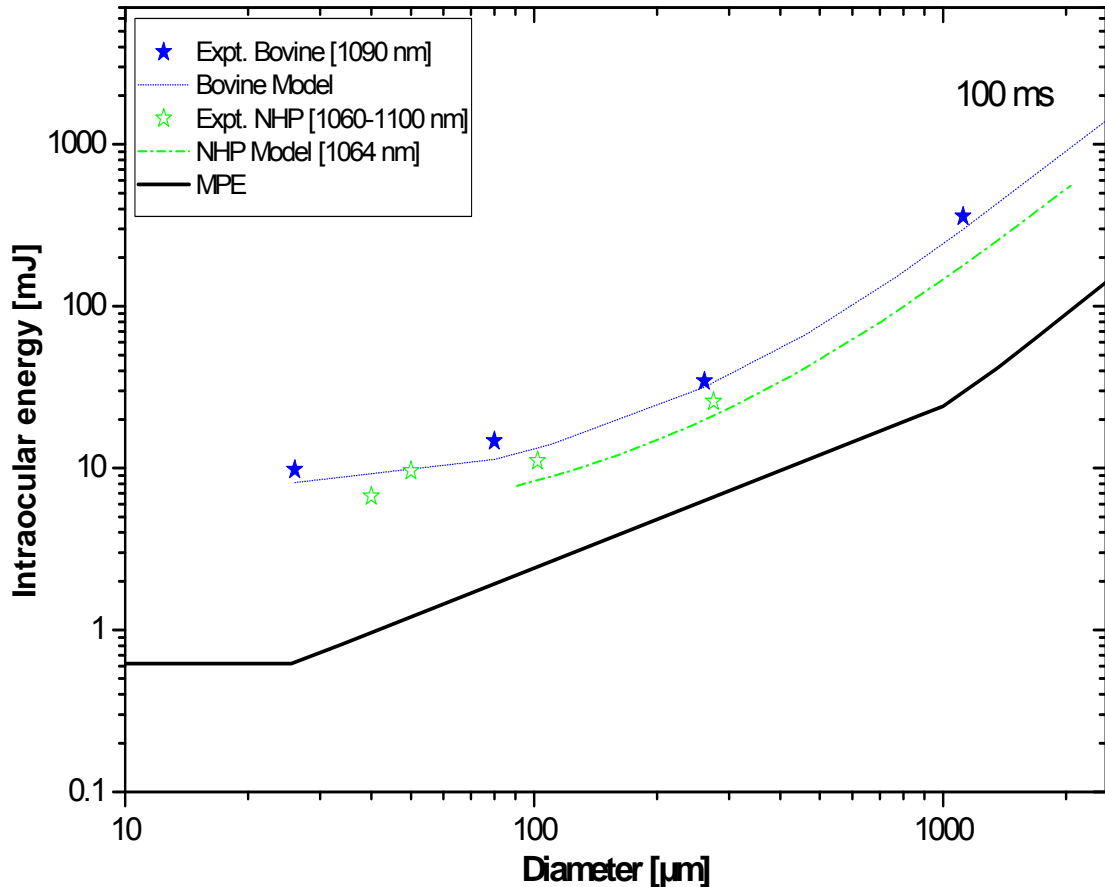


Figure 4.10: 100 ms pulse duration *in-vivo* NHP threshold data (open stars), *ex-vivo* bovine (closed stars; corrected for 62 % transmission at the Cornea), Bovine model data (dotted blue line), NHP model data (dash dot green line) and the current MPE data (full black line). The data are plotted in terms of TIE as a function of retinal spot size diameter.

Considering the minimum image size, modified where required, on the retina specified in [73-76], *in-vivo* NHP threshold results are in good agreement with the computer model calculations based on NHP model threshold results as can be seen in figure 4.10. Similarly, comparing the experimental threshold results of two models, i.e. *in-vivo* NHP and *ex-vivo* bovine, for 100 ms pulse duration, show a difference, on the average, by a factor of 1.54. Although, the end point approach as well as models used for threshold measurements are different. *Ex-vivo* bovine RPE lesion investigation is based on RPE cell viability under the microscope, whereas, *in-vivo* NHP retinal lesion/no-lesion data used for threshold measurements are based on ophthalmoscopic observations.

4.6.3 Comparison with the 532 nm Ex-vivo Bovine Threshold Data

Ex-vivo explant bovine retinal threshold results for the 1090 nm (this study) together with the published threshold results for the 532 nm using the same experimental model are presented in table A.3. For comparison, threshold results, obtained for the two wavelengths, are plotted in terms of radiant exposure as a function of spot size diameter for various pulse durations as shown in figure 4.11. Other exposure parameters such as sample preparation, exposure pattern, sample analysis, end point approach, delay time between time of exposure and time of examination etc. remain same.

Despite the difference in threshold value (ED50), the spot size dependence trend is also different for the two wavelengths. The logarithmic slope value for each pulse duration, in the 1/D dependence region, for the 1090 nm is steeper than for the 532 nm. Furthermore, for short pulse duration more steepness in the 1090 nm thresholds data have been observed as compared to the 532 nm which can be easily seen in figure 4.12, where the thresholds are plotted on the different scales.

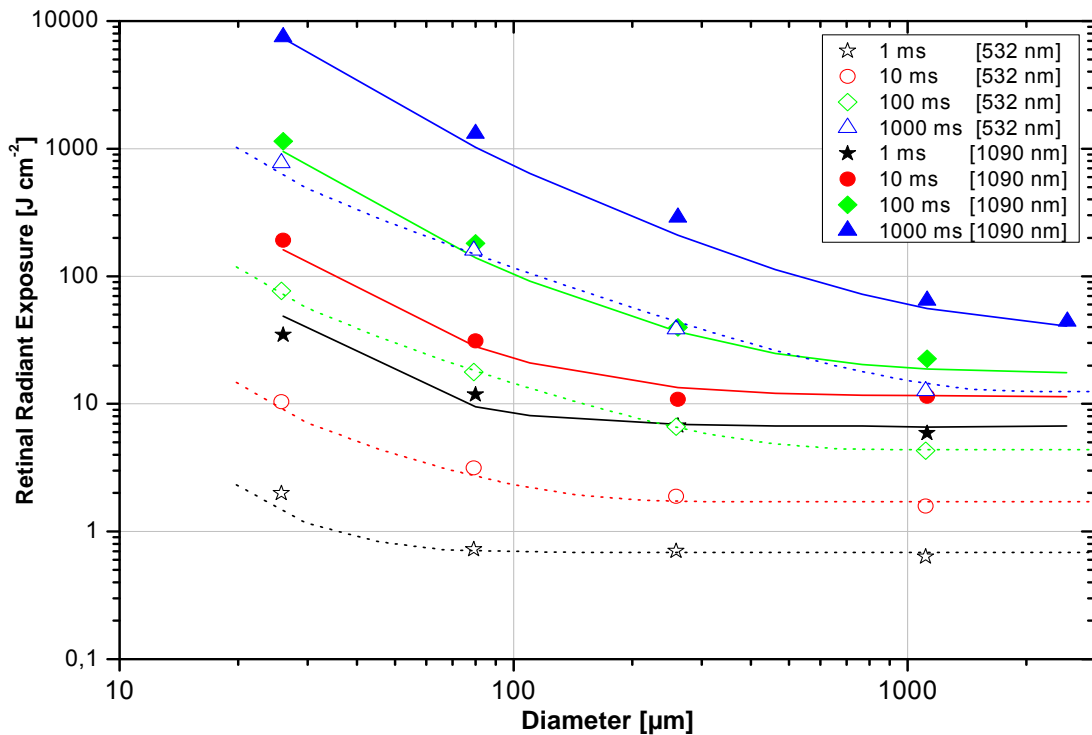


Figure 4.11: *Ex-vivo* bovine RPE damage thresholds for two wavelengths: 1090 nm Gaussian profile (closed symbols) and 532 nm TopHat (open symbols; small spot 26μm had Gaussian profile) along with bovine computer model data (dotted line: 532 nm and full line: 1090 nm).

Another important point to note in the spot size dependence is the variation in the time dependent α_{\max} i.e. breakpoint or the knee position, between $1/D$ dependence region and the no spot size dependence region, for the two wavelengths. For 1 ms threshold data, the breakpoint between the two regions, stated above, for the 532 nm lies at $\sim 70 \mu\text{m}$, whereas, for the 1090 nm at diameter larger than $100 \mu\text{m}$.

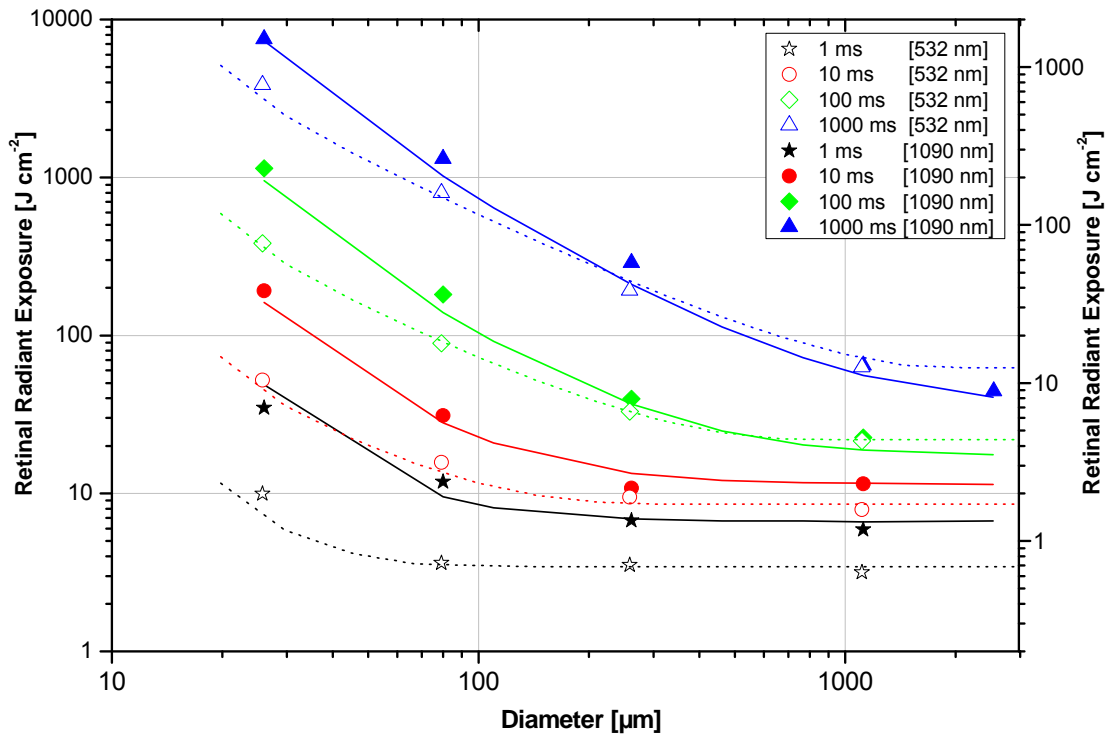


Figure 4.12: Same data as in figure 4.11 but adjusted by eye to comparable levels for long exposure duration. *Ex-vivo* bovine RPE damage thresholds for two wavelengths: 1090 nm left scale Gaussian profile (closed symbols) and 532 nm right scale TopHat (open symbols) along with bovine computer model data (dotted line: 532 nm) and (full line: 1090 nm) using different scale.

Furthermore, for any pulse duration, moving from left to right in the spot size dependence i.e. from small spot diameter to large spot diameter, difference in damage threshold between the two wavelengths decreases. Additionally, for same spot size diameter, the shorter the pulse duration the larger the difference between thresholds for the two wavelengths. For the smallest spot size diameter and the shortest pulse duration, difference in damage thresholds between the two wavelengths as large as 17.5 times have been observed.

4.7 Discussion

4.7.1 Spot Size and Time Dependencies

Ex-vivo bovine retinal thermal damage thresholds for the wavelength of 1090 nm have been established for the first time showing spot size as well as pulse duration dependencies in the time domain from millisecond to second. A computer model, developed by this group, used for bovine thermal retinal damage threshold calculations also confirmed these dependencies and accordingly the two models validate each other as seen in figure 4.8 and figure 4.9. The same computer model has been validated against the *non-human primate* (NHP) retinal threshold data published over the past four decades.

The current MPE in terms of radiant exposure state the inflexion point or the break point ' α_{\max} ', between the spot size dependence region and no spot size dependence region; at fix position i.e. 100 mrad (1.7 mm), independent of pulse duration. *Ex-vivo* bovine retinal damage threshold studies, both the in visible wavelength (532 nm) [77] and this study, have shown that this current value is only applicable for pulse duration longer than 1 s. Both these studies, as can be seen in figure 4.8, confirmed that the inflexion point or α_{\max} value progresses towards smaller diameters as pulse duration become shorter and shorter suggesting a time dependent α_{\max} value.

The physical interpretation of the general spot size dependence or the time dependent α_{\max} value can be explained with the help of the 'thermal diffusion length' l given by $l = 2\sqrt{t\kappa_{Therm}}$ [m], where t is exposure time or pulse duration, and κ_{Therm} is thermal diffusivity given by $\kappa_{Therm} = K/\rho C_p$ [$m^2.s^{-1}$] such that, K is thermal conductivity [$W.m^{-1}.k^{-1}$], ρ is density [$kg.m^{-3}$], and C_p heat capacity [$J.kg^{-1}.k^{-1}$]. For this study, the values of K , ρ , and C_p , used in computer model calculations for the bovine thermal damage threshold measurements, were 0.6305 [$W.m^{-1}.k^{-1}$], 992.22 [$kg.m^{-3}$], and 4178.5 [$J.kg^{-1}.k^{-1}$] respectively.

Previously, it has been observed in [77], that the spot size diameter 'D' characterized by the inflexion point is approximately equal to twice of the diffusion length ' l '. Diffusion length is the distance covered by the heat waves moving outward in the radial direction from the exposure site (hot spot) or the cooling waves moving inward from the surrounding cooler region, for the respective pulse duration. The same trend is also observed in this study, and hence, one can conclude from the above observation that, if

the spot size diameter 'D' is larger than twice of the diffusion length i.e. $2l$ for a given pulse duration, local radiant exposure or irradiance will be independent of the spot size diameter. On the other hand, if $D < 2l$, cooling will play role in diminishing temperature rise, and as a result damage threshold increases compared to the case where there is no cooling. Therefore, the inflexion point is a consequence of the relation between spot size diameter and cooling of the irradiated spot, particularly in the center. Another important point regarding the 1 s data in figure 4.8 is the absence of the breakpoint or knee between the spot size dependence ($1/D$ dependence) and no spot size dependence regions. As stated above, currently α_{\max} has been assigned a constant value of 100 mrad (1.7 mm). However, the experimental threshold results for the 1 s pulse duration, in this study, do not reflect the breakpoint or the knee between a spot size and a no spot size dependence regions, and showed decrease even for a very large spot ~ 2.5 mm. Despite the difficulty to execute an exposure and lack of the data points, an experimental *ex-vivo* bovine threshold value for this large spot i.e. 2.5 mm was necessary to confirm computer model calculations for the large spots.

Similarly, the time dependence, when threshold data is plotted as a function of pulse duration as shown in figure 4.9, of the spot size dependence breakpoint also results in a variation of time dependence for different spot size diameters. For small spot i.e. $26 \mu\text{m}$ the slope in the log-log scaled time dependence is ~ 0.8 , and is very little steeper than the slope value currently reflected in the MPE i.e. 0.75 for pulse duration longer than 1 ms. For short pulse durations, less than 1 ms, the time dependence become shallower. Extrapolation of the experimental threshold results predict that, all curves for different spot size diameters will merge into one for pulse duration less than about $10 \mu\text{s}$. This prediction is also verified by computer model calculations used for bovine except for very small spot i.e. for $26 \mu\text{m}$, where the computer model predicted the no time dependence at much higher threshold value as compared to the experimental threshold results as can be seen in figure 4.9. In time domain $\leq 10 \mu\text{s}$, thermal confinement is reached, where theoretically no heat is dissipated of the absorbed laser energy during the pulse duration. Under thermal confinement conditions of a homogenous medium, damage threshold show no time dependence for all spot sizes.

Similarly, for large spot size diameters, the region of shallower time dependence extends to longer times which are because of the variation of time dependence for different spot size diameters as stated above. Regarding the shallower of time dependence for very large spot size diameter e.g. for $1120 \mu\text{m}$, where the time

dependence slope in log-log scale is 0.35, is more or less reminiscent of the time dependence of the MPEs defined for thermal corneal and skin damage, which is 0.25 [77]. Based on these observations, one can conclude or predict that, for spot size larger than 2 mm, the time dependence is expected to follow similar trend as reflected in the MPEs for thermal corneal and skin damage, which is $t^{0.25}$.

4.7.2 Comparison with Nonhuman Primate (NHP) Threshold Data

As shown in figure 4.10, *in-vivo* NHP threshold results when plotted in terms of TIE as function of spot size diameter are in good agreement with the computer model calculations based on NHP model. Furthermore, *in-vivo* NHP threshold results when compared with *ex-vivo* bovine thresholds are lowered, on the average, by factor of 1.54. A number of factors can be assigned to this difference in the two model thresholds e.g. sample background temperature, pigmentation, absorption co-efficient etc.

Pigment density or melanin concentration in the RPE is similar in most vertebrates, but different in the choroid [78]. For comparable pigmentation and hence absorption co-efficient in the two models, sample background temperature remains the only dominant parameter based on which lower threshold in *in-vivo* NHP compared to *ex-vivo* bovine can be explain. The rhesus monkey body temperature at the time of exposure is always kept at around 38 °C, whereas, the *ex-vivo* explant bovine samples are exposed at room temperature around 23 °C. Computer model calculations, based on NHP model, have shown a reduction in damage threshold by factor of 1.58 for the 1060 nm when sample background temperature was increased from 23°C to 38°C. Hence, one can conclude that, sample background temperature is the main reason for difference in thresholds between the two models. Unfortunately, no exact comparison for the two models has been found in the literature.

Moreover, the most important point to note in the two models is the different endpoint approach. The *ex-vivo* explant bovine thresholds are determined on the average 30 min after the exposure and are based on the RPE cell viability tests under the microscope as discussed in previous sections, whereas, *in-vivo* NHP thresholds are based on ophthalmic observations 1 or 24 h, in some cases 48 h [75], after exposure. Similarities found in the two model thresholds, for a range of spot sizes as shown in figure 4.10, hence confirmed immediate RPE cell death.

Studies have shown that delay, time between exposure and examination, for thermal injury has an impact of lowering threshold by a factor of 1.2 [79]. The delayed

appearance of lesion (change of visual appearance of the sensory retina and not the RPE), 1- or 24-h post exposure, in *in-vivo* NHP model is caused by physiological reactions of the system to the injured RPE cells which take some time to evolve. However, the effect of delay time on damage threshold in *ex-vivo* bovine model is ruled out, because *ex-vivo* bovine samples when re-analyzed under the microscope after 1-h or even longer time, shows no decrease in damage threshold value. Furthermore, it also follows that it is unlikely that the change of appearance at the 1- or 24-h threshold is thermally induced coagulation of the sensory retina. Thermally induced coagulation of the sensory retina should be visible immediately after exposure, which is the case, for instance, in medical photocoagulation treatment of the retina. For thermally induced photocoagulation of the RPE as well as the sensory retina, higher temperatures and hence higher radiant exposures are required than the 1- and 24- h injury thresholds which are, however, the more appropriate endpoints for setting safety limits.

4.7.3 Comparison with the 532 nm *Ex-vivo* Bovine Threshold Data

Laser-induced retinal thermal lesion arises primarily in the pigment epithelium by virtue of concentration of the light-absorbing pigments, contained within the RPE as well as in the choroid. As stated in section 2.3.4, absorption co-efficient of the RPE decreases monotonically with increasing wavelength, and hence, damage threshold increases. Studies have shown more than 50 % absorption of visible (~ 532 nm) radiation and less than 4 % of NIR (~ 1100 nm) within the RPE in rhesus monkey [76,80].

For comparable pigmentation in the RPE in most vertebrates, already discussed in previous section, and assigning the above mentioned absorption co-efficient values to *ex-vivo* bovine model, damage threshold of the RPE cells for the 1090 nm should be higher by a factor of more than 15 compared to the 532 nm. Comparison of damage threshold results for the two wavelengths, for small spot size diameter and short pulse duration, have revealed differences as large as ~ 17 as shown in table A.3.

Similarly, in figure 4.11, moving from small spot diameter to large spot diameter and from short pulse duration to larger pulse duration, the difference in damage thresholds between the two wavelengths decreases. This could be due heat contributed by the choroid pigments in raising the temperature of the RPE cells, hence lowering damage threshold. As shown in section 2.3.4, the absorption co-efficient of the RPE and the choroid is comparable for the 1090 nm. For very long pulse duration, heat generated in the choroid can contribute in raising the temperature of the RPE cells, hence lowering

the damage threshold. Figure 4.11 depict that, the minimum difference between the two wavelengths thresholds are for largest spot size diameter i.e. 1120 μm and longest pulse duration 1 s. The same phenomenon can also be explain in another way, for long pulse durations heat flow reduces the temperature in the RPE cells for the 532 nm case, hence, raising the threshold damage for the 532 nm and making it more similar to the 1090 nm, where the heat is spread out not by conduction but by deep optical penetration.

5 Effect of the Hank Solution, Temperature, and Dye on Damage Threshold

5.1 Background

Ex-vivo explant bovine retinal thermal thresholds have been determined and published for the wavelength of 532 nm for varying number of pulse durations and spot size diameters given in [77]. These thresholds are based on experiments in which no additional hank solution (phosphate buffered saline), which nourishes the RPE cells from dissection until examination, was added on the surface of retinal samples. Although, the computer model, developed by this group, used for thermal damage calculations assume a medium, with the physical properties of water, overlying the RPE cells.

In order to verify the possible influence of hank solution on damage thresholds, several exposure series for different combination of exposure parameters have been performed by adding ~ 2.5 mm thick layer of hank solution above the retinal samples, and compare these results with thresholds measured with no hank solution above the samples. The sample preparation and exposure pattern are exactly the same as previously discussed in section 4.3. Retinal samples after exposure have been analysed under fluorescence microscope for lesion no lesion in the same manner as discussed in section 4.4.

Additionally, instead of body temperature (~ 38°C), which is normally followed in all *in-vivo* non-human primate (NHP) retinal threshold experiments, all retinal samples used for threshold measurements in *ex-vivo* bovine model were exposed to laser radiation at room temperature ~ 23°C. To investigate the effect of temperature on damage thresholds, additional series of exposure on *ex-vivo* bovine retinal samples are made with increased sample background temperature i.e. around body temperature (~38°C) for varying number of pulse durations. These two combinations i.e. different sample background temperatures and different pulse durations were chosen in order to; assess decrease in thermal damage threshold with increasing sample temperature, and to quantify this decrease in damage threshold as a function of time.

Another series of *ex-vivo* bovine retinal exposures was designed to evaluate the effect of dye CalceinAM, used for cell viability testing in fluorescent microscopy, on damage threshold. For this series of experiments, samples have been stained with the dye CalceinAM before and after exposure to laser radiation. Comparison of the measured

thresholds, obtained using CalciinAM before and after exposure to laser, has two advantages; First, one can verify that cell death occurs due to rupture or damage of cell membrane, and Second, using the dye afterwards will reassure that there is no or only a small effect of the dye on damage threshold (ED50), because almost all experimental *ex-vivo* bovine model threshold data were collected using the dye before exposure.

5.2 Experimental Setup

The schematic overview of the experimental setup used for *ex-vivo* explant bovine retinal sample irradiation is shown in figure 5.1. Two frequency-doubled Nd:YAG identical lasers (Omicron FK-LA 8000, Germany) emitting radiation in the wavelength range of 532 nm are coupled which provide, in the continuous wave (CW) mode, maximal output power of 18 W altogether. These lasers have a beam propagation factor M^2 around 8 [81]. After combining the two laser beams by means of a polarization crystal, the beam is coupled into a fiber of length 10 meters having core diameter of 50 μm . Fiber has been used in order to achieve a homogenous spatial beam profile (called top-hat). A lens attached close to the distal end of the fiber can be moved nearer or farther to achieve the desired collimated beam. Depending on the desirable beam diameter on the retinal sample, a varying number of lenses have been used to image the output plane of the fiber onto the tissue sample. A galvanometer-driven scan head (SCANLAB, hurrySCAN™ 14, Germany) was placed between the optical system and the sample to achieve the desired exposure pattern.

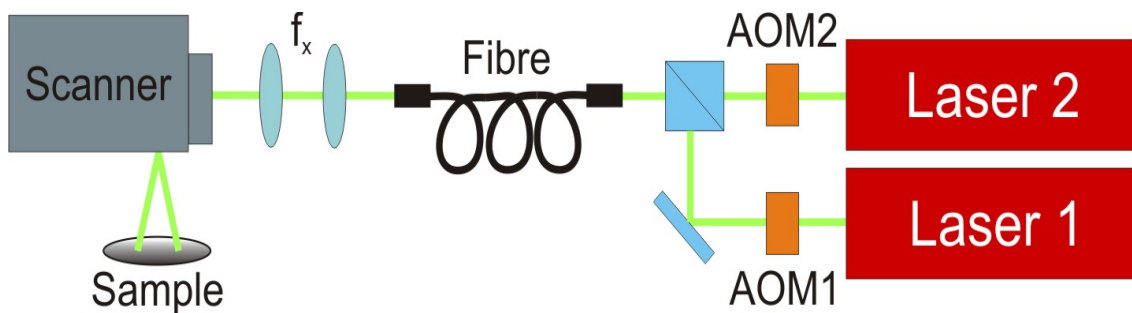


Figure 5.1: System for exposure of bovine retina samples. f_x denote a varying number of lenses imaging the output plane of the fibre on the retina with selectable diameters [81].

The power level and exposure duration of the two lasers are controlled with the help of Acousto Optical Modulators AOM (AA optoelectronics, MTS110-A3-VIS, France)

located next to the output aperture of each laser. The AOM control the laser power as a function of time with a temporal resolution of $10\ \mu\text{s}$ and a throughput resolution of 1024 steps between zero and maximum transmission. The scanner and the AOM performance were controlled by a PC interface card (SCANLAB, RTC[®] 4, Germany) with the help of a computer program developed by Thomas Auzinger, *Scanner Control 1.08*. This automatic system enables us not only to achieve an arbitrary number of exposures with high precision, but also to perform experiment in a comparatively short period of time. Depending upon the desired output power in the sample plane, the diode current of the two lasers were set to a fixed value. Afterwards, a warm-up time of at least 90 minutes was given to the two lasers before each experiment in order to achieve stable laser output power. Similarly, the AOM, as stated above, with multiple functions i.e. temporal rectangular pulse shape with user defined length (minimum $10\ \mu\text{s}$), and modulating the incident laser power into 1024 different power levels, was used for each irradiation. The response behaviour of the AOM follows a sigmoid shape as shown in figure 5.2. In order to keep the error as minimum as possible, only power levels between 300 and 700 have been applied.

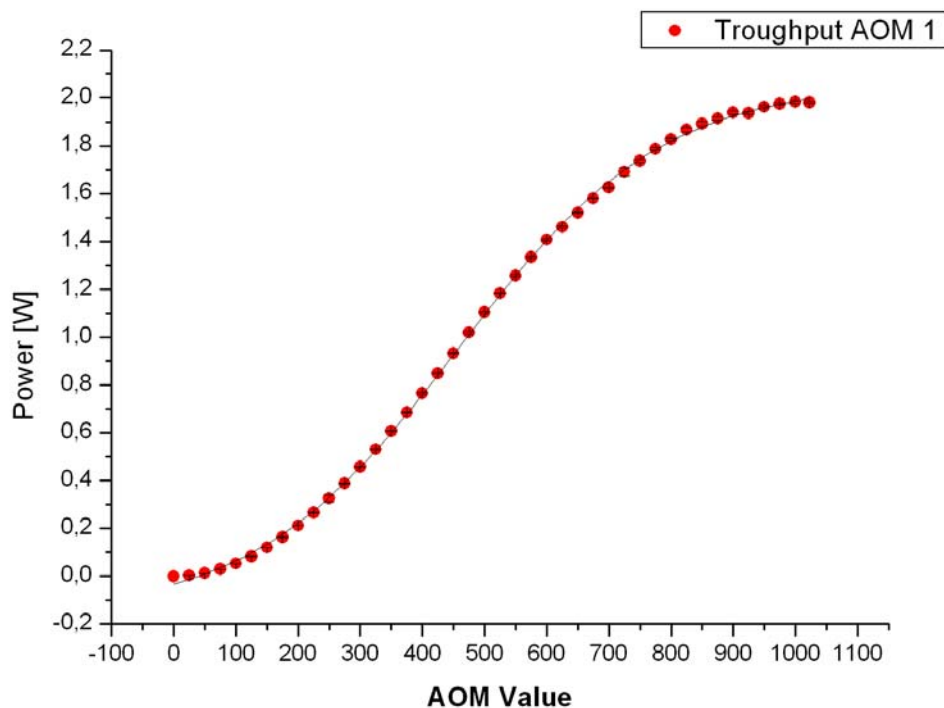


Figure 5.2: The throughput of AOM 1 as a function of bit value. In order to get a linear response, only bit values between 300 and 700 have been used [81].

Prior to exposures, the spatial beam profile was recorded with a CCD-camera (COHU, model 7512, USA). The CCD camera was placed beneath the scanner at a position where the samples were desired to expose to laser radiation. Figure 5.3 shows a three dimensional view of spatial top hat profile recorded with CCD camera. Since the camera was very sensitive, even very lesser laser power may damage it, hence different neutral density filters (Melles Griot, USA) have been used between the optical system and CCD camera for attenuating the laser power. The camera has a pixel size of $6.7 \mu\text{m} \times 6.7 \mu\text{m}$ and an array size of 1292×1024 . The beam diameter was determined using the definition of $1/e$ of the peak intensity, and was calculated with beam analyzer software (Spiricon, LBA-700PC, USA).

To measure the transmitted output power of the optical system, two calibrated power meters (Ophir, 3A and L40(150)A, USA), depending upon the combined output power of the two laser, were put at or below the sample position to record power incident upon the samples for a fully opened AOM. The actual energy deposited on each exposure site was then calculated in Microsoft Excel sheet, using the calculated output power for a fully opened AOM at the sample plane, the pulse duration, and the two AOM throughput characteristics. Using the above stated three parameters an energy or dose range has been selected for each threshold experiment such that, the minimum and maximum exposure dose or energy values contained the expected damage threshold. The linearity of the two power meters has already been discussed in section 4.5.

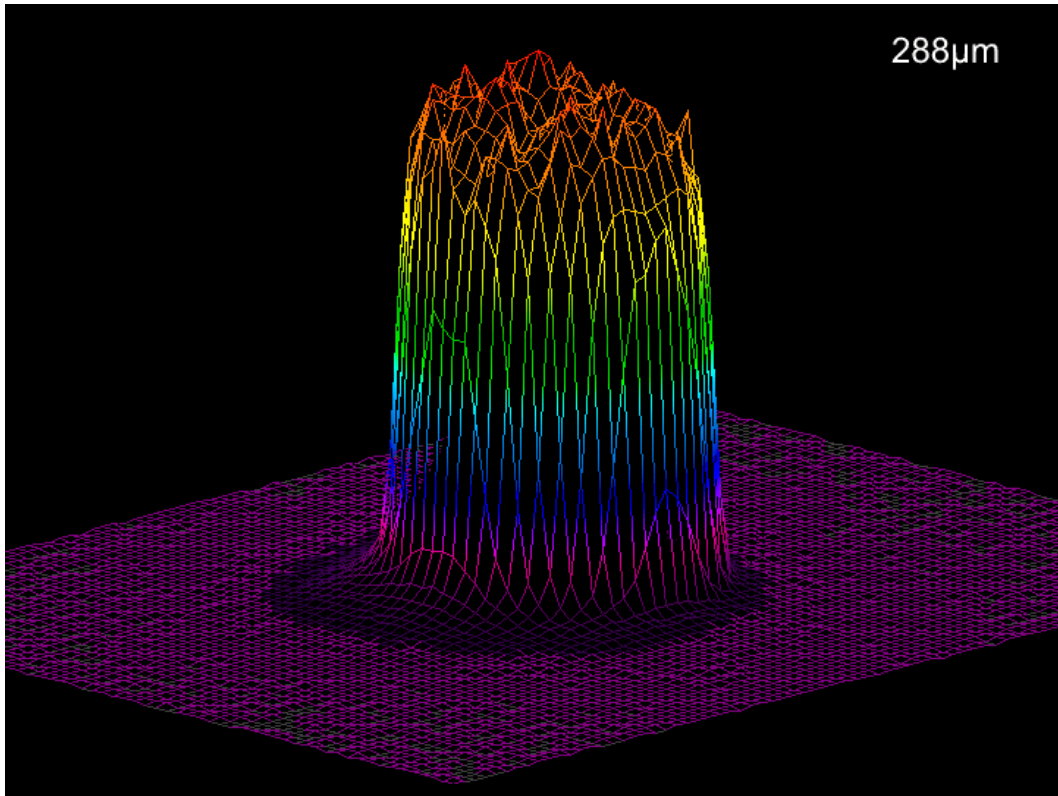


Figure 5.3: Three dimensional view of top hat beam profile recorded with CCD camera.

5.3 Results and Discussion

5.3.1 Effect of Hank Solution on Threshold Data

5.3.1.1 Results

In order to evaluate the possible effect of hank solution on the damage thresholds, two set of thresholds (ED50) data have been obtained. In first case, thresholds were determined for samples exposed to laser without adding hank solution above their surfaces, and are called without hank (WOH) thresholds. In second case, thresholds were determined for samples exposed to laser radiation with a thick layer of hank, approximately 2.5 mm, above their surfaces, and are called with hank (WH) thresholds. These experimental *ex-vivo* bovine thresholds (ED50) measured from the dose-response curve calculated by using probit analysis software, based on lesion/no-lesion data, for WH and WOH are summarized in table A.4. These results have been gathered for two spot size diameters i.e. 80 μm and 288 μm , and for varying number of pulse durations ranging from 0.1 ms to 655 ms.

All samples were exposed with a spatial beam profile called “Top Hat”. The slope S (ED84/ED50) that results from probit analysis of the experimental data remains within the range 1.01 and 1.2. This sharp value of slope confirmed both, little variability within the retinal samples e.g. age, gender, location in the eye etc as well as a small uncertainty [66] e.g. experimental fault, environmental conditions etc. To compare the two damage threshold results i.e. WH and WOH, for evaluation of effect of hank solution on damage threshold, a total of 3231 exposures have been executed on 124 *ex-vivo* bovine retinal samples.

Thermal damage threshold data for WH and WOH in terms of radiant exposure as a function of spot size diameter is plotted in figure 5.4. For the confirmation of spot size dependence of the experimental thresholds, computer model data, as calculated by Mathieu Jean, based on *Arrhenius damage integral* is also shown in the same figure. The spot size dependence shown by computer model in this time domain was followed by both data sets. Comparing the experimental results of WOH and WH, no difference have been found for short pulse durations but, a difference of upto 1.40 have been noted for long pulse duration and large spot diameter.

Additionally, the factor i.e. the ratio between with and without hank thresholds (WH/WOH) is also plotted as a function of pulse duration for the two spot size diameters and shown in figure 5.5. The effect of hank solution on damage threshold for the two spots is clearly distinguished in this figure. For large spot sizes, the factor or the ratio (WH/WOH) remains close to one for pulse duration ≤ 1 ms, indicating that these thresholds are independent of the hank solution. For pulse duration > 1 ms, the two threshold differentiates, indicating that addition of hank solution above the sample surface enhances damage threshold. Furthermore, this difference between WH and WOH increases with increasing pulse duration, showing pulse duration dependence, such that maximum difference of 1.4 for 655 ms pulse duration is seen for 288 μm . For small spot diameter, on the other hand, the factor or ratio (WH/WOH) remains constant independent of the pulse duration as can be seen in figure 5.5. Another important point observed in this is the difference between the factor values of the two spot size diameters. The factor (WH/WOH) for small spot size diameter is always less than the large spot diameter.

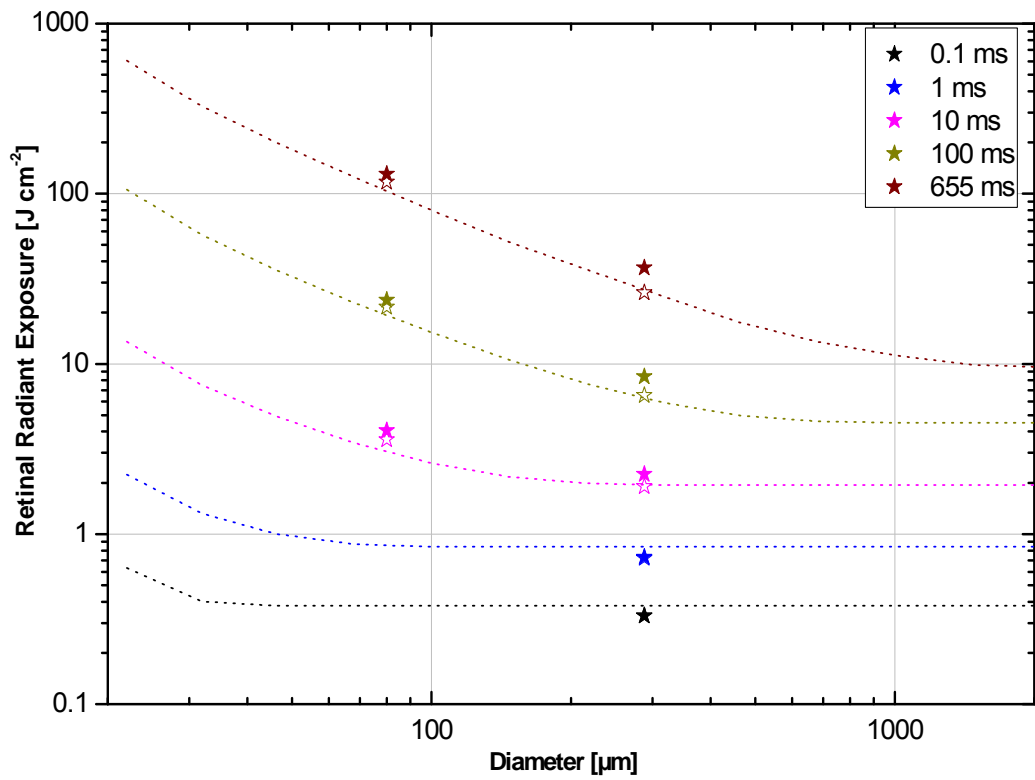


Figure 5.4: Single pulse *ex-vivo* bovine retinal threshold in terms of radiant exposure as a function of spot size diameter for with and without Hank solution. Closed symbols represent with Hank (WH) thresholds, while open symbols show without Hank (WOH) thresholds. Dotted lines represent computer model data.

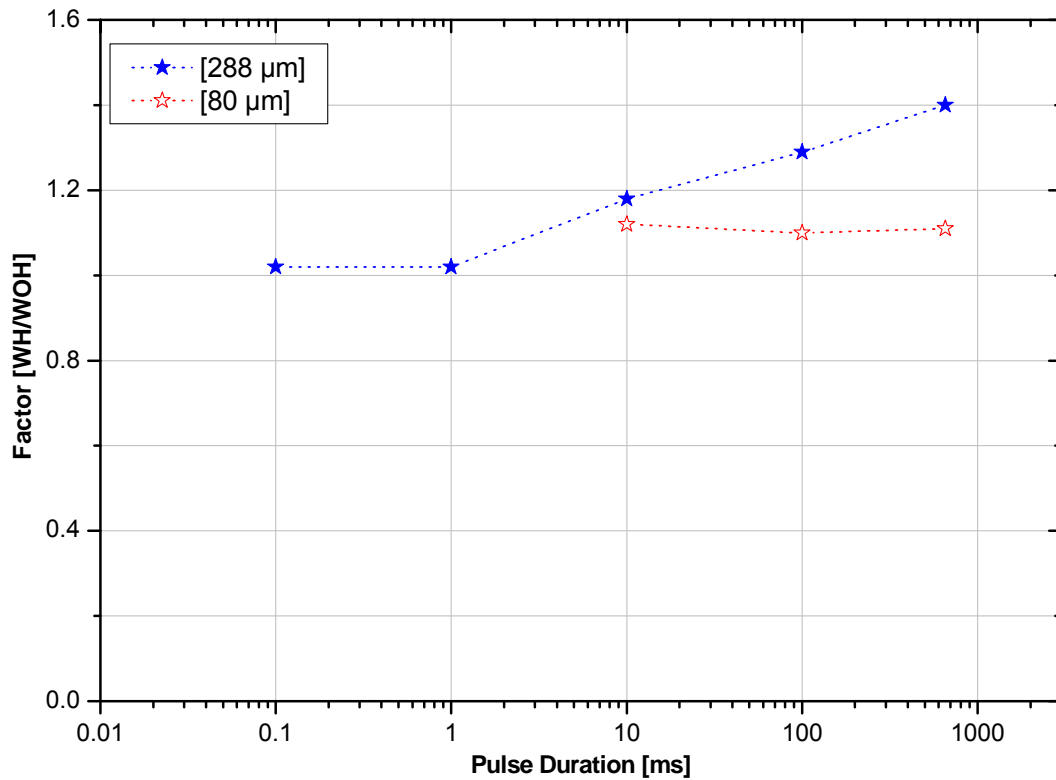


Figure 5.5: Ratio between with and without Hank solution thresholds plotted as a function of pulse duration. Closed stars represent data for 288 μm diameter, while open stars indicate data for 80 μm diameter.

5.3.1.2 Discussion

Figure 5.4 shows *ex-vivo* bovine threshold data, obtained for with and without hank solution above the sample surface. These experimental thresholds show good agreement with the computer model data when plotted in terms of radiant exposure as a function of spot size diameter. For short pulse duration $\leq 1\text{ms}$, the experimental results reveal no difference in the two damage thresholds obtained for with and without hank solution for both spot sizes. For pulse duration $\geq 1\text{ms}$ the gap in the damage thresholds for with and without hank solution starts to build-up and increase with increasing pulse duration specifically for the 288 μm .

This phenomenon can be explained on the basis of heat waves, generated in the irradiated zone of the RPE cells due to absorption of laser radiation, and moving in upward direction during irradiation. As stated earlier, all *ex-vivo* bovine samples, used for experiments, were kept continuously under Phosphate Buffered Saline (PBS) i.e.

hank solution, from the time of dissection until examination. Hence, exposure with no hank solution does not mean sample with dry surface, but a very thin hank layer.

For pulse duration i.e. ≤ 1 ms, the heat wave moving in the upward direction from the heated zone were even unable to pass on this few micron thin layer during irradiation. In other words, the time of exposure is too short for conduction and convection process to react effectively and taken away handsome amount of heat from the irradiated zone in case of with hank solution during irradiation period. That is why, the damage thresholds for both with and without hank solution remains the same i.e. independent of the hank solution for these short exposure durations. On the other hand, for pulse duration ≥ 1 ms, considering the WH case, the irradiation time is much greater than the time required for heat waves to move in the upward direction taking away some amount of heat from the irradiated zone but, less than the time required for the heat waves to cross the 2.5 mm thick layer. Hence the damage threshold for with hank solution keeps on increasing with increasing pulse duration. In the other case i.e. WOH, the irradiation time is much larger than the time required for the heat wave to reach the interface between thin hank layer and air. Heat waves, once reaches at this interface, are encounter by air which acts as an insulating layer, restricting heat removal from the heated zone. As a result, no increase in damage threshold occurred due to excess heat taken in the upward direction. This effect can be seen in figure 5.5.

Considering small spot size thresholds for with and without hank solution, two phenomena have been observed. First; damage threshold increases for with hank solution as compared without hank solution for pulse duration ≥ 10 ms as explain above. Second; the ratio between with and without hank thresholds (WH/WOH) remain constant, independent of pulse duration as can be seen in figure 5.5. This phenomenon, however, is somewhat surprising and did not find a simple reasoning on the basis of which that could be explained.

Another important point to note in figure 5.5 is the difference in factor value (WH/WOH) for the two spot size diameters. The factor value obtained for small spot diameter is always less than what obtained for large spot. One possible reason for this effect could be the difference in surface area of the two irradiated spots. Since for large spot, heat waves are generated from larger surface area as compared to the smaller surface area for small spot. Thus, for any pulse duration ≥ 10 ms, more heat is taken away from large spot by these heat waves as compared to small spot. Hence, the difference in damage thresholds or factor value obtained for with and without hank for

larger spot is larger as compared to the difference for small spot. Unfortunately, this comparison, between hank and no hank, can not be verified from our computer model, because, as stated in section 5.1, our computer model assumes an infinite medium in front of the retina.

5.3.2 Effect of Temperature on Threshold Data

5.3.2.1 Results

Taking into consideration, the effect of sample background temperature on thermal damage threshold, a series of experiments have been performed to determine thermal damage thresholds at two different sample temperatures. These threshold results were obtained with top-hat beam profile i.e. 288 μm spot size diameter for two pulse durations i.e. 100 ms and 655 ms, and are presented in table A.5. These experimental results along with computer model data, for two different temperatures, plotted in terms of radiant exposure as a function of pulse duration, are shown in figure 5.6. As was expected, damage thresholds for both pulse durations decrease when sample background temperature increases from room temperature $\sim 23\text{ }^{\circ}\text{C}$ to body temperature $\sim 37\text{ }^{\circ}\text{C}$ as can be seen in figure 5.6.

Computer model calculations, based on bovine model, also predicted decrease in damage threshold with increasing sample background temperature. However, the reduction factor (ratio between damage thresholds obtained for sample background temperature at room temperature to threshold obtained for body temperature), predicted by the computer model was higher when compared with experimental threshold results. Experimental results illustrate a reduction factor of 1.2 and 1.34 for 100 ms and 655 ms pulse durations respectively, whereas, computer model calculations predicted a factor value of more than 1.5 for the above mentioned spot size diameter and pulse durations.

The difference in the reduction factor between computer model calculations and experimental results may be due to experimental uncertainties and biological variability or due to the fact that sample background temperatures used in experiments were not exactly $37\text{ }^{\circ}\text{C}$ but $\leq 35\text{ }^{\circ}\text{C}$. However, the important point of observation between the computer model calculations and the experimental threshold results is the trend, i.e. increase in reduction factor value with increasing pulse duration, shown by both models used for threshold measurements. For two sample background temperatures i.e. $23\text{ }^{\circ}\text{C}$

and 37 °C, computer model calculations show a reduction factor value of minimum 1.35 and maximum 1.67 for 10 μ s and 1 s pulse durations, respectively.

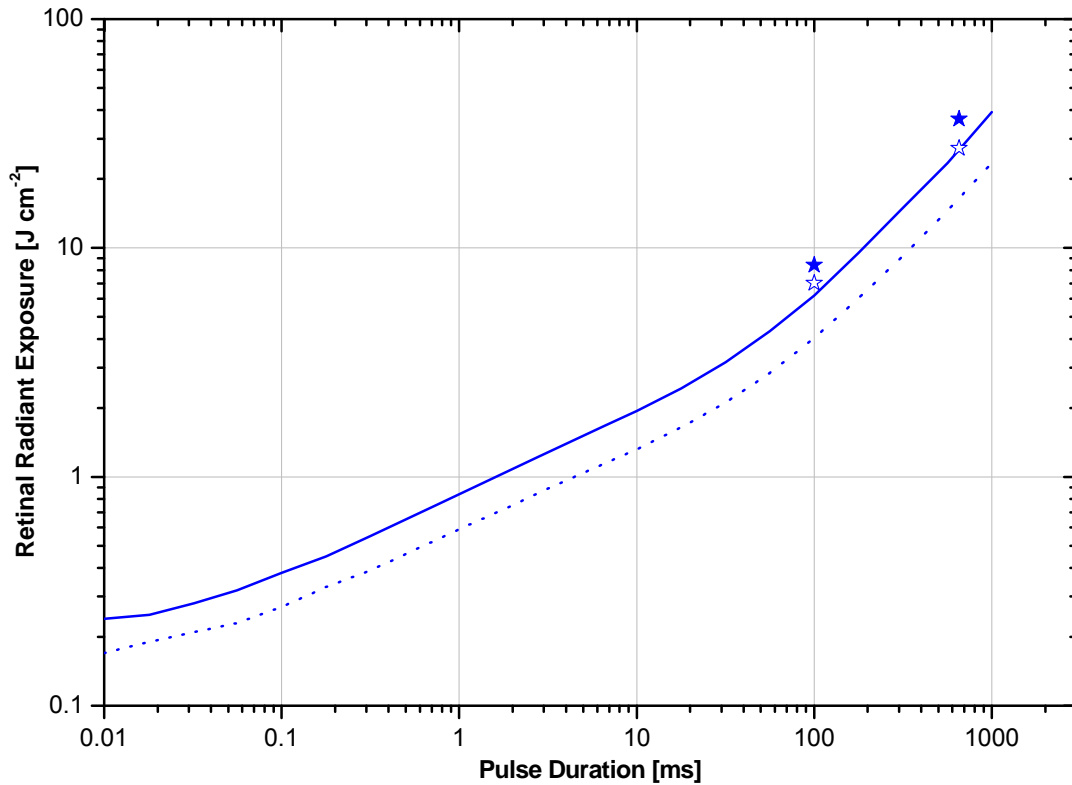


Figure 5.6: *Ex-vivo* bovine thresholds of 288 μ m diameter in terms of radiant exposure plotted as a function of pulse duration. Closed stars represent experimental data for 100 ms and 655 ms at 23 °C, while open stars represent data at 37 °C. Solid and dotted lines represents computer model data for 23 °C and 37 °C respectively.

5.3.2.2 Discussion

Figure 5.6 show threshold results obtained for *ex-vivo* bovine retinal samples, when irradiated with two different background temperatures i.e. room temperature and body temperature, plotted in terms of radiant exposure as a function of pulse duration. Computer model data is also shown for the two temperature values. As was expected, both, experimentally measured *ex-vivo* bovine thresholds as well as thresholds calculated with computer model, decreases when sample background temperature was increased from room temperature to body temperature. The difference in damage threshold for two sample background temperatures is seen because; in biological tissue

thermal injury occurs only if tissue temperature rises to a certain degree and sustain for a particular period. Damage accumulates cumulatively as a function of temperature and time until a critical level of injury is reached. Using this time-temperature history the *Arrhenius* damage integral determines quantitatively how much damage is occurred. This time-temperature relation, a critical parameter, demonstrates that, for same thermal damage to occur, samples irradiated at body temperature require less energy as compared to samples irradiated at room temperature.

The difference in reduction factor value, or ratio between thresholds obtained at two different sample background temperatures, for two pulse durations i.e. 1.2 for 100 ms to 1.34 for 655 ms can be well explain with the help of time-temperature history. As stated above, the extent of thermal injury in tissue is proportional to the magnitude and duration of temperature increase, or its “time-temperature history”. The time-temperature relation manifests that the minimum required temperature, to attain thermal injury, increases with decreasing pulse duration, or injury occurs in biological tissue at lower temperature when heated for longer time and vice versa. Based on this theory, one can deduce a conclusion that, the effect of tissue background temperature on damage threshold is more pronounce in 655 ms pulse duration case when compare to 100 ms pulse. Hence, large difference in damage thresholds or reduction factor has been observed for 655 ms pulse duration when compared to 100 ms pulse duration.

Computer model calculations based on bovine model using *Arrhenius* damage criterion also confirm decrease or reduction in damage threshold by increasing tissue background temperature. As stated in previous section, a reduction factor of more than 1.5 is predicted by model calculations for the two stated pulse durations. However, for pulse duration ranges from 10 μ s to 1s, model calculations predicted a reduction factor value of 1.35 to 1.67 respectively for a number of spot size diameters, showing that this phenomenon is independent of the spot size diameter. Same observations of lowering damage thresholds for increased tissue background temperature are discussed in [77] when comparing *ex-vivo* bovine model results with *in-vivo* NHP model.

5.3.3 Effect of Dye CalceinAM on Threshold Data

5.3.3.1 Results

CalceinAM, a membrane permeant fluorogenic esterase substrate that is hydrolyzed in live cells to yield cytoplasmic green fluorescence, is a dye which is used for cell

viability testing of *ex-vivo* explant bovine RPE cells. In order to investigate, whether the dye CalceinAM affects damage threshold or not, *ex-vivo* explant bovine retinal samples were exposed to laser radiation (532 nm), with specified set of exposure parameters, using the dye before and after exposure. Threshold results calculated with probit analysis software based on lesion/no-lesion data for these series of experiments and for a range of pulse durations are presented in table A.6. These results are plotted in terms of retinal radiant exposure as function pulse duration, and shown in figure 5.7. For comparison, computer model thresholds are also plotted in the same figure. Threshold results for both series of experiments i.e. dye CalceinAM used before and after exposure are in good agreement with each other and followed the trend predicted by computer model calculations.

All *Ex-vivo* explant bovine samples were exposed with a spatial beam profile that represents a constant irradiance level (referred to as “Top Hat”) that was achieved using a combination of lenses as described in section 5.2. The slope S (ED84/ED50) that results from probit analysis of the experimental data remains within the range 1.01 and 1.13. This sharp value of slope confirmed both, little variability within the retinal samples as well as a small uncertainty. To assess the effect of dye on damage thresholds, a total of 1584 exposures have been executed on 44 bovine retinal samples. Threshold results obtained for all pulse durations, when the dye CalceinAM was applied afterward, are always somewhat smaller than the results obtained where dye was used before exposure. Furthermore, comparison of threshold results for the two series show a reduction in threshold, on the average, by factor of 1.13.

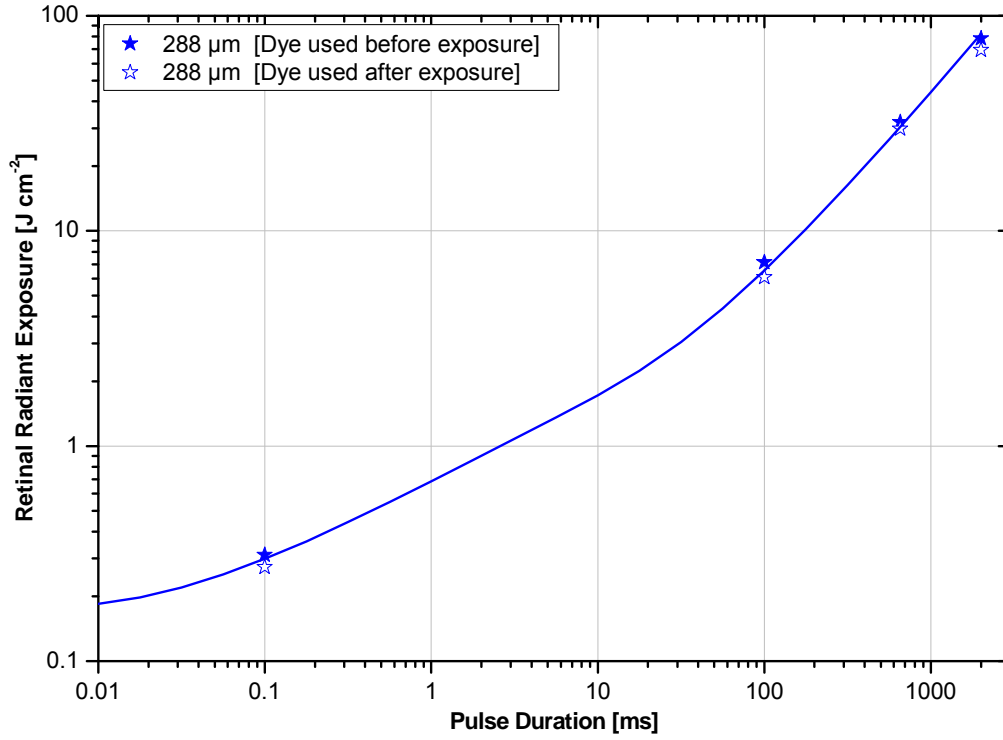


Figure 5.7: *Ex-vivo* bovine thresholds of 288 μm diameter in terms of radiant exposure plotted as a function of pulse duration. Closed and open stars represent experimental data for dye used before exposure and after exposure, respectively. Solid line represents computer model data.

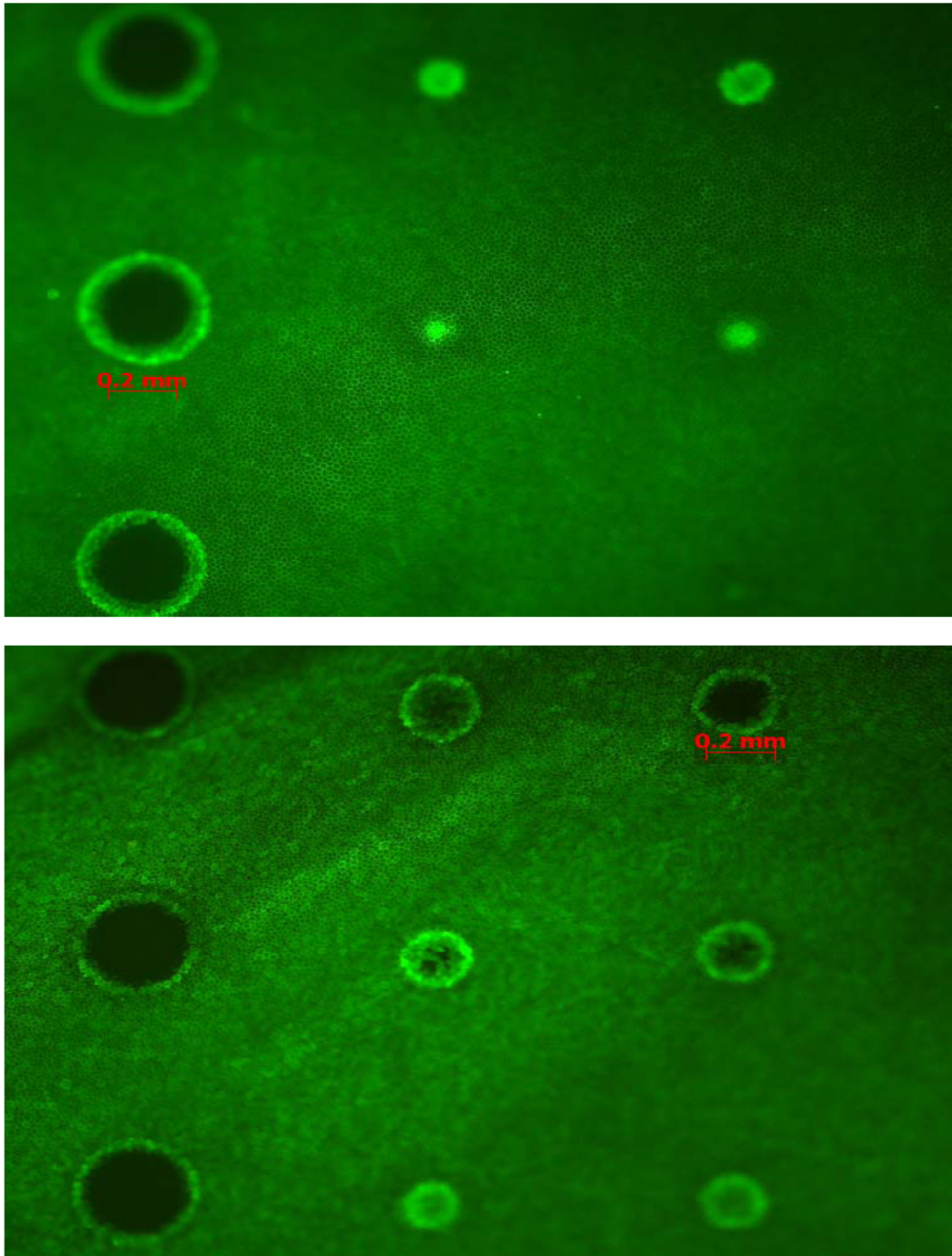


Figure 5.8: An exposed RPE sample. Top image represents sample when stained after exposure, while below is an image of sample when stained before exposure. The left most columns in both images represent super threshold grid points. The middle and right columns show dose near damage threshold. The brighter site between clearly damaged and no damaged region can also be seen and was graded as damaged.

It must be noted, however, that in experiments where the dye CalceinAM was applied before, all samples were examined under the microscope before exposure to insure the

quality of the samples, and to see any prior damage to samples due to mishandling in the preparation process or environmental conditions. Samples which were declared well in quality were then exposed to laser and used for threshold measurements. This cross check was not possible in experimental series where the dye CalceinAM was applied after exposure to laser radiation.

To get rid of false positive lesion or chance of scoring the presence of lesion which is not triggered by the laser radiation but present otherwise, exposure sites were examined with great care, especially in case where the dye was applied afterward. One must also note the delay (time between laser exposure and examination) which was different for the two series. As stated in section 4.4, the delay time noted for experiments, where the dye was applied to samples first, was in the range from 20-30 minutes. In the other series, the delay prolonged to approximately one and half hour, because all samples were stained after exposure and then analyzed under the microscope for lesion or no-lesion data.

5.3.3.2 Discussion

Figure 5.7 show *ex-vivo* bovine retinal thermal threshold results when plotted in terms of radiant exposure as a function of pulse duration. For comparison, computer model data for same exposure parameters are also shown in that figure. As can be seen in this figure, damage threshold data for both sample categories followed the trend predicted by computer model calculations, based on bovine model, for thermal damage. However, comparison between thresholds obtained for the two sample categories, on the average, have shown difference by a factor of 1.13.

In biological tissue damage experiments, where changes undergo a time course following injury, delay between laser exposure and time of examination is regarded the most critical element. For thermal injury, *in-vivo* NHP thresholds get lowered by a factor of 2 or less for different delay time which ranges from 5 minutes to 24 h [80]. As explained, in *in-vivo* NHP threshold experiments, the viability of RPE cells can not be determined and lesion detection is based a change of visual appearance of the sensory retina, not the RPE [78]. The change of colour or appearance of the sensory retina is caused by the physiological reaction that evolved with time.

Threshold values lowered by a factor of 1.13 for the case when the dye CalceinAM was applied afterward, observed in this study, cannot be explained on the basis of longer

delay time, because; firstly, in *ex-vivo* explant bovine experiments RPE cells are directly observed under the microscope for lesion/no-lesion data, and secondly, samples which were analyzed under the microscope 30 minutes after exposure, in case when the samples were stained first, when re-analyzed after 1 h shows no decrease in damage threshold. Hence, based on these observations, one can conclude that the dye CalceinAM does have an influence on damage threshold but it is regarded as rather small compared to effects from other sources.

Additionally, the optical appearance of damage of the exposed sites, in both sample categories i.e. stained before or after exposure, is exactly the same as seen in figure 5.8. This similarity in the appearance of lesion confirm damage of the cell membrane or protein denaturation which in turn is responsible for cell death as well as highly localized damage effect due to strong absorption in the RPE at this particular wavelength.

6 Summary

In the field of health and safety, an emphasis on laser radiation is due to its low beam divergence, which together with high energy content can result in an excessive amount of radiation transferred to a biological tissue. This emphasis even further increases for the visible and near infrared (NIR) radiation due to the transmission of the ocular media and the optical focusing properties for this particular wavelength band of radiation. In the past four decades lasers have become increasingly important tools in research, medicine, and Engineering. Biological effects are not always beneficial, and if improperly used or controlled, lasers can produce injuries (including burns, blindness, or electrocution) to operators and other persons.

Lasers that emit light with wavelengths in the visible and NIR parts of the spectrum are transmitted well by the ocular media. In addition, the eye optics focuses the beam, giving intense concentration of radiation on the retina. This concentrated energy, when above the threshold, can cause retinal injury because this energy is absorbed by the RPE cells in the retina and the underlying choroid. Much more work has previously been done in modelling the mechanism of retinal injury due to the absorption of laser energy from 400-1400 nm. These models calculate the temperature rise due to optical radiation absorption in the biological tissue and predict the radiant exposure at which cellular injury and death occurs as a result of temperature rise above a threshold level; however, there is time-temperature dependence.

Today, evaluation of the risk due to irradiation of the retina by laser is of great importance. The potential hazard of laser in the wavelength regime from UV to NIR and exposure duration from femtoseconds to seconds has been extensively studied. The majority of the data on laser induced retinal injury are obtained from experiments on laboratory animals (*in-vivo*) or animal tissues (*ex-vivo*) which provides basis in setting safety standards for the human eye. These standards i.e. *Maximum Permissible Exposure* (MPE) are set well below the thresholds (ED50) such that biological variability between inter- and intra- individuals are accounted for, and exposures at the MPE are not hazardous.

The purpose of this study is to determine laser induced retinal thermal thresholds (ED50) using single pulse duration for the wavelength of 1090 nm. *Ex-vivo* explant bovine eye is used as experimental model. This report contains experimental threshold results, based on fluorescence microscopy, along with the computer model data,

developed by Mathieu Jean at Seibersdorf Labor GmbH, and validated by comparing with *in-vivo* NHP thermal injury threshold data. These experimental results are obtained for varying pulse durations from 1 ms to 1 s, and spot size diameter from 26 μm to 2539 μm . For a combination of four pulse durations and five different spot size diameters, a total of 3453 exposures have been executed on 184 samples. Threshold results for this wavelength has been established for the first time, showing spot size as well as pulse duration dependencies in the time domain from millisecond to second. Finally, it is concluded that for the NHP model, the underlying damage mechanism at thresholds detected 1 or 24 h after exposure is most likely to be immediate RPE cell damage, not thermal coagulation of the sensory retina.

The advantage of *ex-vivo* explant bovine retinal model, over the *in-vivo* NHP models is that precise dosimetry of the energy incident on the retinal as well as the desired spot size diameter on the retina is possible, as well as stable sample without the influence of ocular clouding or aberrations of the eye. Furthermore, due to availability and cost, an experimental series that covers two parameters, pulse duration and spot size, is not practical with *in-vivo* NHP models. Moreover, the comparison of threshold data for the *ex-vivo* bovine, obtained in this study, and the *in-vivo* NHP models, for specific laser parameters, even further emphasis on the reliability and applicability of this experimental model.

Since laser, emitting in a wavelength of 1060 nm, are used preferentially for coagulations purpose. Detailed understanding of the retinal damage mechanism at these specific laser parameters is necessary because *in-vivo* NHP threshold data, available in the literature, is obtained only for 'worst case' scenario, considering minimum spot size on the retina. Thresholds obtained in this study will be analyzed by the international committees such as ICE, ANSI, and ICNIRP, and will be used in future to improve the safety for lasers. Further experimental work, in addition to the two wavelengths considered in this thesis, is also necessary for complex laser beam profiles such as rectangular, ring etc as well as other wavelengths such as visible and UV have to be considered.

Similarly, other series of experiments on bovine retina have been performed to investigate, effects of Hank solution (phosphate buffered saline), which nourishes the RPE cells from dissection until examination, tissue background temperature, and the dye CalceinAM used for cell viability testing. For this purpose, three different series of

experiments on *ex-vivo* bovine retinal samples with the wavelength of 532 nm have been performed for varying spot size diameters and pulse durations.

In the first series of experiments, in order to verify the possible influence of Hank solution on damage thresholds, several experiments have been performed for with Hank (WH) and without Hank (WOH) solution above the retinal samples. These results have been gathered for two retinal spots, i.e. 80 μm and 288 μm , and for varying number of pulse durations ranging from 0.1 ms to 655 ms. In these experiments, a total of 3231 exposures have been executed on 124 *ex-vivo* bovine retinal samples. Based on the results, it is concluded that, differentiation in damage threshold between WH and WOH starts at pulse duration $> 1\text{ms}$ for both spot sizes, and a maximum difference of a factor of 1.4, between WH and WOH thresholds for pulse duration 655 ms and spot size diameter 288 μm , is seen. This factor of 1.4 has to be considered by the committee using *ex-vivo* bovine damage threshold data for defining exposure limits for the human eye because the human retina is surrounded by an infinite medium of water.

In the second series of experiments, to investigate the effect of tissue background temperature on damage thresholds, *ex-vivo* bovine retinal samples were exposed to laser radiation with increased sample background temperature from $\sim 20\text{ }^{\circ}\text{C}$ to $\sim 38\text{ }^{\circ}\text{C}$ for two different pulse durations. These two different sample background temperatures as well as pulse durations are chosen in order to; assess decrease in thermal damage threshold with increasing sample temperature, and to quantify this decrease in damage threshold as a function of time. Experimental results illustrate a reduction factor of 1.2 and 1.34 for 100 ms and 655 ms pulse durations respectively, whereas, the computer model calculations predicted a factor value of more than 1.5 for the same spot size diameter and pulse durations. Based on time-temperature theory, we deduced that, effect of the tissue background temperature on ED50 is more pronounced in 655 ms pulse duration case when compare to 100 ms pulse.

In the last series of experiments, effect of the dye CalceinAM, used for cell viability testing, on damage threshold, was evaluated. For this series of experiments, samples have been stained with the dye CalceinAM before and after exposure to laser radiation. A total of 1584 exposures have been executed on 44 bovine retinal samples. Threshold results obtained for all pulse durations revealed that, damage threshold for the dye CalceinAM, when applied afterward, are always less than the results obtained where the dye was used before exposure. Comparison of threshold results for the two series show a reduction in threshold, on the average, by factor of 1.13. These results have two

advantages; first, it verified that cell death occurs due to rupture or damage of cell membrane, and second, using the dye afterwards reassured that dye does have an influence on damage threshold but it is regarded as rather small compared to effects from other sources.

III. APPENDIX-A
EXPERIMENTAL RESULTS

Pulse Duration [ms]	Spot Size Diameter [μm]	Retinal Radiant Expo. [J cm^{-2}]	Lower Fiducial Limit [J cm^{-2}]	Upper Fiducial Limit [J cm^{-2}]	Slope [ED84/ED16]	Number of Samples	Number of Exposures	Comp. Model Radiant Expo [J cm^{-2}]	Ratio [Expt./Model]
1	26	34.73	27.76	30.99	1.17	11	239	48.68	0.71
	80	10.82	9.37	10.61	1.09	6	96	9.49	1.14
	261	6.74	5.25	6.07	1.25	12	206	6.92	0.97
	1120	5.89	4.72	526	1.2	32	128	6.64	0.89
10	26	190.69	181.00	196.64	1.21	11	363	161.31	1.18
	80	31.06	29.39	31.69	1.15	5	245	27.98	1.11
	261	10.82	9.81	11.44	1.17	4	100	13.41	0.81
	1120	11.48	9.53	12.69	1.22	13	52	11.56	0.99
100	26	1142.15	1075.43	1205.76	1.25	10	250	952.33	1.19
	80	181.75	176.84	186.59	1.15	9	288	139.63	1.30
	261	39.79	38.48	41.12	1.18	9	324	36.71	1.08
	1120	22.57	21.53	23.57	1.10	9	81	18.80	1.20
1000	26	7522.47	7211.44	7808.41	1.16	8	228	7308.15	1.03
	80	1315.07	1250.69	1380.25	1.28	13	421	1020.60	1.29
	261	289.28	281.89	296.90	1.14	12	352	209.91	1.38
	1120	64.64	60.74	67.09	1.09	16	64	55.91	1.16
	2539	44.47	44.47	44.47	1.01	4	16	-	-

Table A.1: Probit threshold data for the range of pulse durations 1 ms - 1 s, and retinal spot diameters, where relevant, from 26 μm to 2.5 mm, of *ex-vivo* explant bovine model for the 1090 nm. Beam profile for all retinal spots was Gaussian (1/e diameter criteria). The ED50 given as retinal radiant exposure was determined from the ED50 given in terms of total energy (TIE) divided by the area calculated from the spot diameter.

Laser	Wavelength [nm]	Pulse Duration [ms]	Spot Size Diameter [μm]	ED50 at Cornea [mJ]	Reference
Nd: YAG	1060	100	40	6.7	Skeen, 1972
Nd: YAG	1060	100	50	9.6	Vassiliadis, 1969
Nd: YAG	1064	100	275	25.79	Ham, 1978
OPO	1110	100	102	11.06	Vincelette, 2009
Fibre	1090	100	26	9.78	This Study
		100	80	14.74	
		100	261	34.33	
		100	1120	358.65	

Table A.2: Comparison between *ex-vivo* explant bovine (this study) and *in-vivo* NHP threshold data in terms of TIE (Corneal space) for similar laser parameters.

Pulse Duration [ms]	Spot Size Diameter [μm]	Retinal Radiant Exposure [532 nm] [J/cm^2]	Retinal Radiant Exposure [1090 nm] [J/cm^2]	Factor [1090 nm/532 nm]
1	26	1.99	34.73	17.45
	80	0.73	11.93	16.34
	261	0.71	6.74	9.49
	1120	0.63	5.89	9.35
10	26	10.41	191.69	18.41
	80	3.15	31.06	9.86
	261	1.89	10.82	5.72
	1120	1.58	11.48	7.27
100	26	76.7	1142.15	14.89
	80	17.81	181.75	10.20
	261	6.61	37.79	5.72
	1120	4.29	22.57	5.26
1000	26	771.5	7522.47	9.75
	80	159.85	1315.07	8.23
	261	38.57	289.28	7.50
	1120	12.62	64.64	5.12

Table A.3: Comparison of the ED50 given as retinal radiant exposure, obtained from *ex-vivo* explant bovine model for the 532 nm and 1090 nm. Beam profile for all retinal spots for the 1090 nm was Gaussian (1/e diameter criteria), while, Top Hat (TH) for 532 nm except 26 μm .

Spot Size Diameter [μm]	Pulse Duration [ms]	Temperature [°C]	Retinal Radiant Exposure without Hank (WOH) [J/cm ²]	Retinal Radiant Exposure with 2.5 mm Hank (WH) [J/cm ²]	Slope (ED84/ED50) [WOH---WH]	Number of Samples	Number of Exposures	Factor [WH/WOH]
80	10	22	3.59	4.04	1.10---1.07	15	344	1.12
	100	23	21.53	23.68	1.11---1.14	14	492	1.10
	655	23	117.27	130.44	1.12---1.20	12	394	1.11
288	0.1	23	0.33	0.33	1.01---1.06	8	144	1.02
	1	23	0.72	0.73	1.02---1.03	8	288	1.02
	10	23	1.90	2.24	1.12---1.08	24	633	1.18
	100	23	6.54	8.42	1.09---1.07	23	576	1.29
	655	23	26.16	36.59	1.08---1.02	20	360	1.40

Table A.4: *Ex-vivo* explant bovine thresholds for without hank (WOH) solution above the samples and for with hank (WH) solution. Beam profile for both spots was Top Hat (TH). The ED50 given as retinal radiant exposure (J/cm²) was determined from the ED50 given in terms of total energy (TIE) divided by the area calculated from the spot diameter.

Spot Size Diameter [μm]	Pulse Duration [ms]	Temperature [°C]	Retina Radiant Exposure [J/cm ²]	Slope [ED84/ED50]	Number of Samples	Number of Exposures	Factor
288	100	23	8.42	1.07	14	324	1.20
		35	7.01	1.01	5	245	
	655	23	36.59	1.02	10	180	1.34
		34.43	27.22	1.09	7	343	

Table A.5: *In-vitro* bovine retinal thermal damage thresholds for 288 μm top hat beam profile, varying number of pulse durations, and for two different sample temperatures. The ED50 given as retinal radiant exposure [J/cm²] was determined from the ED50 given in terms of total energy (TIE) divided by the area calculated from the spot diameter.

Spot Size Diameter [μm]	Pulse Duration [ms]	Temperature [°C]	Retinal Radiant Exposure Using Dye After Exposure [J/cm ²]	Retinal Radiant Exposure Using Dye Before Exposure [J/cm ²]	Slope [ED84/ED50]	Number of Samples	Number of Exposures	Factor
288	0.1	23	0.273	0.312	1.01--1.01	4	144	1.14
	100	24	6.093	7.152	1.06--1.07	15	540	1.17
	655	23	29.820	32.039	1.13--1.11	21	756	1.07
	2000	23	69.388	78.304	1.03--1.01	4	144	1.13

Table A.6: *In-vitro* bovine retinal thermal damage thresholds using dye CalceinAM before and after exposure for 300 μm top hat beam profile, and varying number of pulse durations. The ED50 given as retinal radiant exposure [J/cm²] was determined from the ED50 given in terms of total energy (TIE) divided by the area calculated from the spot diameter.

Bibliography

- [1] G. Smith, D. A. Atchinson. *The eye and Visual Optical Instruments*. Cambridge University Press, Cambridge, 1997.
- [2] Y. Ikuno, K. Kawaguchi, T. Nouchi, and Y. Yasuno. Choroidal Thickness in Healthy Japanese Subjects. *Investigative Ophthalmology & Visual Science*, 51(4): 2173-2176, 2010.
- [3] R. Henderson, and K. Schulmeister. *Laser safety*. Institute of Physics Publishing, Bristol, 2004.
- [4] F. H. Zaidi, J. T. Hull, S. N. Peirson, K. Wulff, D. Aeschbach, J. J. Gooley, G. C. Brainard, K. G-Evans, J. F. Rizo III, C. A. Czeisler, R. G. Foster, M. J. Moseley, and S. W. Lockley. Short-Wavelength Light Sensitivity of Circadian, Pupillary, and Visual Awareness in Humans Lacking an Outer Retina. *Current Biology*, 17:2122-2128, 2007.
- [5] O. Strauss. The Retinal Pigment Epithelium in Visual Function. *Physiological Review*, 85: 845-881, 2005.
- [6] D. M. Berson. Phototransduction in ganglion-cell photoreceptors. *Pflugers Archiv : European journal of physiology*, 454(5): 849–855, 2007.
- [7] S. K. LaBar, P. Dale, E. M. Brannon, C. Roberto, and S. A. Huettel. Principles of Cognitive Neuroscience. Sunderland, Mass, Sinauer Associates Inc, pp. 253, 2007.
- [8] G. Thumann, S. Hoffmann, and D. R. Hinton. Cell biology of the retinal pigment epithelium. In S. J. Ryan, editor, *Retina*, volume 1, Mosby, St. Louis, 4th edition, 2006.
- [9] E. A. Boettner, and J. R. Wolter. Transmission of the ocular media. *Investigative Ophthalmology*, 1(6): 776-783, 1962
- [10] R. D. Glickman, J. M. Gallas, S. L. Jacques, B. A. Rockwell, and D. K. Sardar. Physical and Photochemical properties of ocular melanin. In *Proceeding of SPIE*, volume 4241, pages 112-126, 2001.
- [11] T. Sarna. New trends in photobiology: Properties and function of the ocular melanin -a photobiophysical view. *Journal of Photochemistry and Photobiology B: Biology*, 12(3): 215-258, 1992.
- [12] L. Feeney-Burn. The pigments of the retinal pigment epithelium. *Current topics in Eye research*, 2: 119-178, 1980.

- [13] R. D. Glickman, S. L. Jacques, J. A. Schwartz, T. Rodriguez, K-W. Lam, and G. Buhr. Photodisruption increases the free radical reactivity of melanosomes isolated from retinal pigment epithelium. In *Proceeding of SPIE*, volume 2681, pages 461-467, 1996.
- [14] A. Vogel, V. Venugopalan. Mechanisms of pulsed laser ablation of biological tissues. *Chemical Reviews*, 103(2):577-644, 2003.
- [15] A. D. Yablou, N. S. Nishioka, B. B. Mikic, and V. Venugopalan. Measurement of tissue absorption coefficients by use of interferometric photothermal spectroscopy. *Applied Optics*, 38(7):1259-1272, 1999.
- [16] G. H. Pettit, and M. N. Ediger. Corneal-tissue absorption coefficients for 193- and 213-nm ultraviolet radiation. *Applied Optics*, 35(19):3386-3391, 1996.
- [17] M. L. Wolbarsht, A. W. Walsh, and G. George. Melanin, a unique absorber. *Applied Optics*, 20(13):2184-2186, 1981.
- [18] D. K. Sardar, and R. D. Glickman. Optical characterization of melanin. *Journal of Biomedical Optics*, 6(4):404-411, 2001.
- [19] G. M. Hale, and M. R. Querry. Optical constants of water in the 200-nm to 200- μ m wavelength region. *Applied Optics*, 12(3):555-563, 1973.
- [20] S. L. Jacques. Laser-tissue interaction: photochemical, photothermal, and photomechanical, *Surgical Clinics of North America*, 72(3):531-558, 1992.
- [21] R. Birngruber, C. A. Puliafito, A. Gawande, W-Z. Lin, R. W. Schoenlein, and J. G. Fujimoto. Femtosecond laser-tissue interactions: retinal injury studies. *IEEE Journal of Quantum Electronics*, 23(10):1836-1844, 1987.
- [22] C. P. Cain, C. A. Toth, G. D. Noojin, V. Carothers, D. J. Stolarski, and B. A. Rockwell. Thresholds for Visible Lesions in the Primate Eye Produced by Ultrashort Near-Infrared Laser Pulses. *Investigative Ophthalmology & Visual Science*, 40(10):2343-2349, 1999.
- [23] R. T. Mihran. Interaction of laser radiation with structures of the eye. *IEEE Transactions on Education*, 34(3):250-259, 1991.
- [24] D. Sliney, and M. L. Wolbarsht. *Safety with lasers and other optical sources*. New York, plenum, 1980.
- [25] J. Mellerio. Light effects on the retina: *Principles and Practice of Ophthalmology*. Eds D. M. Albert, and F. A. Jakobiec, W. B. Saunders, Philadelphia, 1994.

- [26] T. G. M. F. Gorgels, and D. V. Norren. Two spectral types of retinal light damage occur in albino as well as in pigmented rat: No essential role for melanin. *Experimental Eye Research*, 66:155-162, 1998.
- [27] L. M. Rapp, B. L. Tolman, and H. S. Dhindsa. Separate mechanisms for retinal damage by ultraviolet-A and Mid-visible light. *Investigative Ophthalmology & Visual Science*, 31(6):1186-1190, 1990.
- [28] E. R. Stadtman. Oxidation of proteins by mixed-function oxidation systems: implication in protein turnover, ageing, and neutrophil functions. *Trends in Biochemical Science*, 11: 11-12, 1986.
- [29] Jr. W. T. Ham, Jr. J. J. Ruffolo, H. A. Müller, A. M. Clark, and M. E. Moon. Histologic analysis of photochemical lesions produced in rhesus retina by short-wavelength light. *Investigative Ophthalmology & Visual Science*, 17(10):1029-1035, 1978.
- [30] A. E. Dontsov, R. D. Glickman, and M. A. Ostrovsky. Retinal Pigment Epithelium Pigment Granules Stimulate the Photo-Oxidation of Unsaturated Fatty Acids. *Free Radical Biology & Medicine*, 26(11/12):1436-1446, 1999.
- [31] U. Wihlmark, A. Wrigstad, K. Roberg, S. E. G. Nilsson, and U. T. Brunk. Lipofuscin Accumulation in Cultured retinal Pigment Epithelium Cells Caused Enhanced Sensitivity to Blue Light Irradiation. *Free Radical Biology & Medicine*, 22(7):1229-1234, 1997.
- [32] M. H. Niemz. *Laser-Tissue Interactions: Fundamentals and Applications*. 3rd enlarged edition, Springer Berlin Heidelberg New York, 2007.
- [33] A. W. Girotti. Photosensitized oxidation of membrane lipids: reaction pathways, cytotoxic effects, and cytoprotective mechanisms. *Journal of Photochemistry and Photobiology. B, Biology*, 63:103-113, 2001.
- [34] TAP Study Group. Photodynamic Therapy of Subfoveal Choroidal Neovascularization in Age-related Macular Degeneration With Vertepofin. TAP Report 1. *Archives of Ophthalmology*, 117:1329-1345, 1999.
- [35] S. L. Jacques, N. Ramanujam, G. Vishnoi, R. Choe, and B. Chance. Modeling photon transport in transabdominal fetal oximetry. *Journal of Biomedical Optics*, 5:277-282, 2000.
- [36] F. H. Johnson, J. Eyring, and M. J. Pollisar. *The Kinetic Basis of Molecular Biology*. New York, John Wiley & Sons, 1954.

- [37] S. Zamenhof, G. Griboff, and N. Marullo. Studies on the resistance of deoxyribonucleic acids to physical and chemical factors. *Biochimica et Biophysica Acta*, 13:459-470, 1954.
- [38] J. Marshall. Lasers in Ophthalmology: The Basic Principles. *Eye (Lond)*, 2 Suppl:S98-112, 1988.
- [39] A. L. McKenzie. Physics of thermal processes in laser-tissue interaction. *Physics in Medicine and Biology*, 35(9):1175-1209, 1990.
- [40] A. J. Welch, and G. D. Polhamus. Measurement and Prediction of Thermal Injury in the Retina of the Rhesus Monkey. *IEEE Transactions on Biomedical Engineering*, 31(10):633-644, 1984.
- [41] J. Marshall. Light Damage and the Practice of Ophthalmology. In *Intraocular Lens Implantation*, Eds: E. Rosen, E. Arnott, and W. Haining, Moseby-Yearbook, London, 1983.
- [42] P. S. Coogan, W. F. Hughes, and J. A. Mollsen. Histologic and Spectrophotometric Comparison of the Human and Rhesus Monkey Retina and Pigmented Ocular Fundus. Report, USAF School of Aerospace Medicine Aerospace Medical Division, Brooks Air Force Base Texas, 1974.
- [43] J. Marshall. Eye Hazards Associated with Lasers. *The Annual of Occupational Hygiene*, 21(1):69-77, 1978.
- [44] A. N. Takata, L. P. Kuan, L. Goldfinch, N. Thomopoulos, J. K. Hinds, and A. Weigandt. Thermal Model of Laser-Induced Eye Damage. Report IITRI-J-TR-74-6324, USAF School of Aerospace Medicine, Brooks Air Force Base, Texas, 1974.
- [45] C. A. Puliafito, R. F. Steinert, T. F. Deutsch, F. Hillenkamp, E. J. Dehm, and C. M. Adler. Excimer laser ablation of the cornea and lens. Experimental studies. *Ophthalmology*, 92(6):741-748, 1985.
- [46] R. Srinivasan. Ablation of Polymers and Biological Tissue by Ultraviolet Lasers. *Science*, 34:559-565, 1986.
- [47] P. E. Dyer, and J. Sidhu. Excimer laser ablation and thermal coupling efficiency to polymer films. *Journal of Applied Physics*, 57(4):1420-1422, 1985.

- [48] Q. Ren, V. Venugopalan, K. Schomacker, T. F. Deutsch, T. J. Flotte, C. A. Puliafito, and R. Birngruber. Mid-Infrared laser ablation of the cornea: A comparative study. *Lasers in Surgery and Medicine*, 12(3):274-281, 1992.
- [49] C- DeMichelis. Laser Induced Gas Breakdown: A Bibliographic Review. *IEEE Journal of Quantum Electronics*, 5(4):188-202, 1969.
- [50] F. Docchio, C. A. Sacchi, and J. Marshall. Experimental investigation of optical breakdown thresholds in ocular media under single pulse irradiation with different pulse durations. *Lasers Ophthalmology*, 1:83-93, 1986.
- [51] A. Vogel, J. Noack, G. Hüttmann, and G. Paltauf. Femtosecond-laser-produced low-density plasmas in transparent biological media: A tool for the creation of chemical, thermal, and thermomechanical effects below the optical breakdown threshold. *Proceedings of SPIE*, 4633:23-37, 2002.
- [52] A. Vogel, and S. Busch. Time-resolved-measurements of shock wave emission and cavitation bubble generation in intraocular laser surgery with picosecond and nanosecond laser pulses. In J. R. Blake et al. (Hrsg.): *Bubble Dynamics and Interface Phenomena*, Kluwer, Dordrecht, 105-117, 1994.
- [53] A. Vogel, P. Schweiger, A. Frieser, M. N. Asiyó, and R. Birngruber. Intraocular Nd:YAG Laser Surgery: Light-Tissue Interaction, Damage Range, and Reduction of Collateral Effects. *IEEE Journal of Quantum Electronics*, 26(12):2240-2260, 1990.
- [54] M. H. Niemz. Investigation and spectral analysis of the plasma-induced ablation mechanism of dental hydroxyapatite. *Applied Physics B: Lasers and Optics*, 58:273- 281, 1994.
- [55] W. Lauterborn, and H. Bolle. Experimental investigations of cavitation-bubble collapse in the neighbourhood of a solid boundary. *Journal of Fluid Mechanics*, 72:391-399, 1975.
- [56] J. Marshall, S. Trokel, S. Rothery, and H. D. Schubert. An ultrastructural study of corneal incisions induced by an Excimer laser at 193nm. *Ophthalmology* 92: 749-758, 1985.
- [57] J. Marshall, S. Trokel, S. Rothery, and R. R. Krueger. A comparative study of corneal incisions induced by diamond and steel knives and two ultraviolet radiations from an excimer laser. *British Journal of Ophthalmology*, 70:482-501, 1986.

- [58] N. Bloembergen. Laser-Induced Electric Breakdown in Solids. . *IEEE Journal of Quantum Electronics*, 10:375-386, 1974.
- [59] T. J. White, M. A. Mainster, P. W. Wilson, and H. H. Tips. Choroidretinal Temperature Increases from Solar Observation. *Bulletin of Mathematical Biophysics*. 33:1-17, 1971.
- [60] C. A. Puliafito, K. Wong, R. F. Steinert. Quantitative and ultrastructural studies of excimer laser ablation of the cornea at 193 nm and 248 nm. *Lasers in Surgery and Medicine*, 7: 155–9, 1987.
- [61] J. Noack, and A. Vogel. Laser-Induced Plasma Formation in Water at Nanosecond to Femtosecond Time Scale: Calculation of Thresholds, Absorption Coefficients, and Energy Density. *IEEE Journal of Quantum Electronics*, 35(8):1156-1167, 1999.
- [62] International Commission on Non-Ionizing Radiation Protection (ICNIRP). Revision of guidelines on limits of exposure to laser radiation of wavelength between 400 nm and 1400 nm. *Health Physics*, 79:431-440, 2000.
- [63] International Electrotechnical Commission (IEC). Safety of laser products-part 1: Equipment classification, requirements and user's guide, ed. 1.2. Technical report IEC-60825-1, IEC, Geneva, March 2007.
- [64] American National Standards Institute (ANSI). American national standards for the safe use of lasers. Technical report Z136.1, Laser Institute of America Orlando, 2007.
- [65] K. C. Smith. Multiple Pathways of DNA repair in bacteria and their roles in mutagenesis. *Photochemistry and photobiology*, 28(2):120-129, 1987.
- [66] D. H. Sliney, J. Mellerio, V. P. Gabel, and K. Schulmeister. What is the Meaning of Threshold in Laser Injury Experiments? Implications for Human Exposure Limits. *Health Physics*, 82(3):335-347, 2002.
- [67] E. Limpert, W. A. Stahel, and M. Abbt. Log-Normal Distributions across the Sciences: Keys and Clues. *Bioscience*, 51(5):341-352, 2001.
- [68] B. J. Lund. The ProbitFit Program to Analyze Data from Laser Damage Threshold Studies. Final Report F41624-02-D-7003, USAMRD-WRAIR, Brooks-City Base, Texas, TX78235, 2006.
- [69] K. Schulmeister, J. Husinsky, B. Seiser, F. Edthofer, H. Tuschl, and D. J. Lund. Explant retinal laser induced threshold studies in the millisecond regime. *Proceedings of SPIE*, 6084(1):E1-E19, 2006.

- [70] CalceinAM Cell Viability Assay, Catalog Number 4892-010-K. R&D System Inc. 614 McKinley Place NE Minneapolis, MN 55413, USA, 2008.
- [71] B. A. Rockwell, D. Hammer, P. Kennedy, R. Amnotte, B. Eilert, J. Druessel, D. Payne, S. Phillips, D. Stolarski, G. Noojin, R. Thomas, and C. Cain. Retinal Spot Size with Wavelength. *Proceedings of SPIE*, 2975:148-154, 1997.
- [72] D. J. Lund, P. Edsall, B. E. Stuck, K. Schulmeister. Variation of laser-induced retinal injury thresholds with retinal irradiated area: 0.1-s duration, 514-nm exposures. *Journal of Biomedical Optics*, 12(2):024023-1, 2007.
- [73] A. Vassiliadis, R. C. Rosan, and H. C. Zweng. Research on Ocular Laser Thresholds. Final Report F41609-68-C-0041, USAFS-AMAMD, Brooks Air Force Base, Texas, 1969.
- [74] C. H. Skeen, W. R. Bruce, J. H. Tips, M. G. Smith, and G. G. Garza. Ocular Effects of Near-Infrared Laser Radiation for Safety Criteria. Final Report F41609-71-C-0016, Brooks Air Force Base, Texas, 1972.
- [75] W. T. Ham, Jr., J. J. Ruffolo, Jr., H. A. Müller, and A. M. Clark, Sensitivity of the retina to radiation damage as a function of wavelength. *Photochemistry and photobiology*, 29:735-743, 1979.
- [76] R. A. Vincelette, B. A. Rockwell, J. W. Oliver, S. S. Kumru, R. J. Thomas, K. J. Schuster, G. D. Noojin, A. D. Shingledecker, D. J. Stolarski, and A. J. Welch. Trends in retinal damage thresholds for 100-ms near-infrared laser radiation exposures: A study at 1,110, 1, 130, 1,150, and 1319-nm. *Lasers in Surgery and Medicines*, 41:382-390, 2009.
- [77] K. Schulmeister, J. Husinsky, B. Seiser, F. Edthofer, B. Fekete, L. Farmer, and D. J. Lund. *Ex vivo* and computer model study on retinal thermal laser-induced damage in the visible wavelength range. *Journal of Biomedical Optics*, 13(5):1-13, 2008.
- [78] K. Schulmeister, J. Husinsky, B. Seiser, F. Edthofer, H. Tuschl, and D. J. Lund. Explant retinal laser induced threshold studies in the millisecond time regime. *Proceeding of SPIE*, volume 6084, pages 1E-119, 2006.
- [79] D. H. Sliney, J. Mellerio, and K. Schulmeister. Implications of using ED-50 and probit analysis in comparing retinal injury threshold data. 2001.

- [80] V-P. Gabel, R. Birngruber, and F. Hillenkamp. Visible and near-infrared light absorption in pigment epithelium and choroid. *International Congress Series No. 450*: 458-462, XXIII Concillium Ophthalmologicum, Kyoto, 1978.
- [81] J. Husinsky. *Experimental Ex-vivo studies of laser-induced thermal damage of the bovine retina for single pulse, multiple pulse, and scanned exposures to improve laser safety standards*. PhD thesis, Technischen Universität Wien, 2008.
- [82] B. Seiser, F. Edthofer, K. Schulmeister. A computer model of retinal thermal damage induced by laser radiation-part 2. Final Report, Seibersdorf Research, Austria, ARC--G--0005, 2005.
- [83] M. Jean, and K. Schulmeister. Laser-induced thermal damage of the Rhesus monkey retina: Computer model Description. Report, Seibersdorf Labor GmbH, Austria, 2010.
- [84] S. L. Jacques. Ratio of entropy to enthalpy in the thermal transition in biological tissues. *Journal of Biomedical Optics*, 11:4, 2006

Lebenslauf

RAHAT ULLAH (M.Sc)

- Date of Birth 1st January, 1976
- Nationality Pakistani

Academic Education

Master of Science in Nuclear Engineering

Sep. 2002

- **Institution.** Pakistan Institute of Engineering and Applied Sciences (PIEAS) Islamabad, Pakistan.
- **Majors.** Radiation Interaction and Detection, Radiological Engineering, Environmental Engineering, LASER Fundamental, Numerical Computing, Numerical Method of Engineering, Thermal Engineering Fundamentals, Thermonuclear Engineering, Nuclear Heat Transport, Applied Mathematics.
- **Project.** Solution of 3-D Navier Stockes Equations using visual C++

Master of Science in Physics

Sep, 1999

- **Institution.** Physics Department, University of Peshawar, NWFP, Pakistan.
- **Majors.** Modern Physics (Atomic Physics), Nuclear Physics, Special Nuclear Physics, Mathematical Methods of Physics, Solid State Physics, Electromagnetic Theory, Classical Mechanics, Statistical Mechanics, Quantum Mechanics, Condense Electronics.
- **Project.** Half value thickness and mass attenuation coefficient of Carbon.

Research Accomplishments:

1) Experience:

- Remains a full time teacher of Physics in Pakistan academic public high school from sep.2000 to april-2000.

- Remains a full time Lecturer of Physics in a degree college, also conducting laboratory of Physics to undergraduate students from may-2000 to oct-2000.
- Working as Senior Scientist in Health Physics & Radiation Protection Division in an R&D organization from 2002 till to date.

2) Other Written work:

- M.Sc Nuclear Engineering dissertation: To determine the velocity profile of the fluid flowing through a rectangular conduit for fully developed flow by Solving 3-D Navier-Stokes Equations using visual C++, which actually described the fully developed fluid.

Supervisor: Dr. Asad Majeed.

- M.Sc Physics dissertation: Half value thickness and mass attenuation coefficient of pure Cooper (99%) using Cobalt-60 source in GM tube.

Supervisor: Dr. Aurang Zeb khan.

3) Seminar/Talk Presented:

- “Radiation interaction and Detection” in Dept. of Physics, University of Peshawar (March, 1998).
- “Radiation and their types”, PIEAS, University Islamabad (Aug. 2002).
- “Biological Effects of radiations”, PIEAS, University Islamabad (Aug. 2002).
- “Personal Dose Management in Nuclear Power Plants” PIEAS, University Islamabad (Aug. 2002).
- “Operational Health Physics activity in Nuclear Power Plants” PIEAS, University Islamabad (Aug. 2002).